Laser Wakefield Acceleration Using Few-millijoule Laser Pulses at Kilohertz Repetition-Rate

by

Zhaohan He

A dissertation submitted in partial fulfillment
of the requirements for the degree of
Doctor of Philosophy
(Nuclear Engineering and Radiological Sciences)
in The University of Michigan
2014

Doctoral Committee:

Associate Professor Alexander G. R. Thomas, Chair
Professor Roy Clarke
Professor Almantas Galvanauskas
Professor Karl M. Krushelnick
Research Scientist John A. Nees

ACKNOWLEDGEMENTS

This dissertation would not have been possible without the support and encouragement from many people.

First and foremost, I would like to express my gratitude to Professor Alec Thomas, for the incredible amount of time and effort he spent providing me guidance and mentorship. I owe my graduate education to the wonderful team of the high field science group at CUOS, University of Michigan. Professor Karl Krushelnick for his advice and ideas. John Nees for his resourceful ideas and teaching me everything I know in the lab. Dr. Bixue Hou for all the help he gave me and his interest with my work. Dr. Anatoly Maksimchuk from the Hercules team, always willing to help and answer my questions. I would also like to thank our collaborators at LOA, Palaiseau, France: Dr. Jérôme Faure, for his insight and assistance in the electron diffraction experiments.

Thanks to my fellow (ex-)students who have provided both academic and spiritual support through my journey in graduate school. In no particular order: Dr. James Easter, Dr. Aghapi Mordovanakis, Dr. Chris McGuffey, Dr. Will Schumaker, Dr. Franklin Dollar, Dr. Calvin Zulick, Dr. Peng Zhang, Benoit Beaurepaire, Vivien Lebailly and many others I have not listed here.

This research was supported financially by the National Science Foundation, the Defense Advanced Research Projects Agency and the MCubed project at the University of Michigan. I would like to acknowledge the OSIRIS consortium of UCLA and IST Portugal for the use of OSIRIS framework. Simulations were performed on the

Flux Cluster at Center for Advanced Computing at the University of Michigan, Ann Arbor.

For my family.

TABLE OF CONTENTS

LIST OF FIGURES

Figure

LIST OF TABLES

Table

LIST OF APPENDICES

Appendix

LIST OF ABBREVIATIONS

ADK Ammosov-Delone-Krainov
BSI Barrier Suppression Ionization
CCD Charge Coupled Device
CPA Chirped Pulse Amplification
DM Deformable Mirror
EMCCD Electron-Multiplying Charged Coupled Device
FOM Figure of Merit
FOP Fiber-Optic Plate
FROG Frequency Resolved Optical Gating
FWHM Full Width at Half Maximum
GA Genetic Algorithm
IP Image Plate
LPA Laser Plasma Acceleration or Accelerator
LWFA Laser Wakefield Acceleration or Accelerator
Nd:YAG Neodymium doped Yttrium Aluminum Garnet
Nd:YLF Neodymium-doped Yttrium Lithium Fluoride
OAP Off-Axis Paraboloid
PIC Particle-in-Cell
PSL Photo-Stimulated Luminescence
RF Radio Frequency
SHG Second Harmonic Generation
SNR Signal-to-Noise Ratio
Ti:S Titanium doped Sapphire
UED Ultrafast Electron Diffraction
(X)FEL (X-ray) Free Electron Laser

ABSTRACT

Laser Wakefield Acceleration Using Few-millijoule Laser Pulses at Kilohertz Repetition-Rate

by

Zhaohan He

Chair: Alexander G. R. Thomas

Compared to conventional sources, electrons produced by a laser plasma based accelerator have some unique properties owing to the much higher acceleration gradient that can be sustained in plasma and the inherent synchronization with the driving laser pulse, making them a potentially useful source for developing tools for ultrafast time-resolved studies. This past decade has seen significant advances in the field of laser driven plasma accelerators, which can now generate electron beams with few femtosecond durations and up to GeV energies [S. M. Hooker, Nature Photon. **7**, 775 (2013)]. One of the main issues with plasma accelerators has been their shot-to-shot reproducibility and stability. In addition, experiments to date have been carried out at low-repetition rate. For many potential applications, increasing the repetition rate from a few hertz to kilohertz or higher will be required.

This thesis describes both experimental and numerical work aiming at the development of a wakefield electron source and applications at kilohertz repetition-rate using few-millijoule pulses. We first present a simple yet robust optical pulse com-

pression technique utilizing an ionization nonlinearity. A self-compressed 16 fs pulse was measured from an original 36 fs pulse containing a few millijoules of energy, which can be beneficial for driving laser wakefield acceleration. Electron acceleration using uncompressed multi-millijoule laser pulses (8 mJ, 32 fs) was studied both in experiments and with particle-in-cell (PIC) simulations. The wakefield acceleration experiments described in this thesis are the first of their kind at 0.5 kHz repetition rate and the first to use a relatively low peak-power (0.3 TW) laser system. Generation of sub-relativistic ($\sim$100 keV) electron beams from laser wakefield acceleration was demonstrated using this high-repetition rate system. An adaptive optimization method was implemented to improve the performance of laser wakefield acceleration through coherent manipulation of the wavefront of the driving laser pulse, enabled by the stability and high-repetition rate. The structure and dynamics of the plasma wave can be subsequently controlled, leading to more than one order of magnitude improvement on the generated electron beam properties such as total beam charge and divergence. Finally, the feasibility of using wakefield electrons for ultrafast studies was investigated through proof-of-principle electron diffraction experiments and a demonstration of probing the ultrafast dynamics of a non-equilibrium plasma.

CHAPTER I

Introduction

1.1 Motivation

Capturing ultrafast dynamics at atomic scale resolution has become a significant endeavor in the scientific community for understanding many important processes in biology, chemistry, material science and solid-state physics. From basic concepts of microscopy, we know that to observe structures that have a small length scale, a probe must be used having a characteristic wavelength of the same order or smaller. In elementary particle physics research, this becomes one of the underlying motivations for constructing ever larger particle accelerators in order to access the extremely short length scales (sub-atomic) of the building blocks of matter. For probing molecular systems and crystalline matter, x-rays, a form of electromagnetic radiation with wavelengths that can be shorter than molecules or atoms, are generally needed. Charged particles from high energy accelerators are used to generate such radiation, for example, from synchrotron sources to X-ray free-electron-lasers (XFEL). These machines have become powerful tools in today's scientific exploration. A limiting factor in modern accelerator technology is the maximum accelerating gradient that can be achieved in a radio-frequency (RF) cavity without breakdown. Consequently, such accelerator based advanced light sources generally require very large infrastructure. As an example, the European XFEL currently under construction, which will deliver

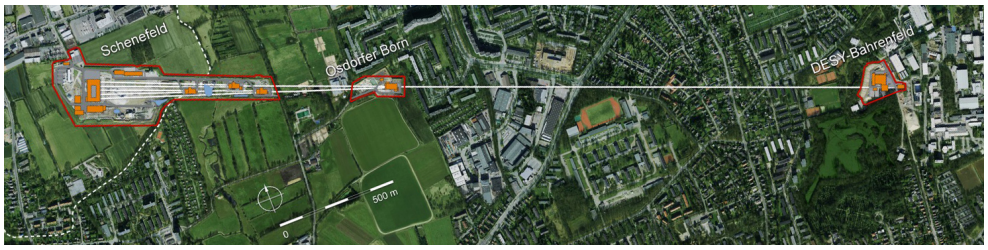

Figure 1.1 Aerial view of the European XFEL with the 3.4-km-long tunnel. Photography courtesy of `www.xfel.eu`

sub-100 fs bright x-ray pulses, as shown in Fig. 1.1, will require an overall cost of 1.15 billion euros. On the other hand, using the wave nature of electrons, for example in ultrafast electron diffraction (UED), is a cost-effective alternative to x-rays and has some unique advantages, such as the larger cross section for elastic interaction with matter and a higher intrinsic spatial resolution due to the shorter wavelengths of electrons. In conventional UED, a dc voltage of tens of kilovolts is typically used to accelerate electrons emitted from a photocathode irradiated by femtosecond UV pulses. One of the greatest challenges limiting the temporal resolution is the space charge effect of nonrelativistic electrons, which happens both near the photocathode source and during acceleration. Electrons accelerated from RF guns have recently been considered [1] because the space charge force will be greatly suppressed at relativistic energies. However, one of the current limitations involved with RF technology is the temporal jitter in pump-probe experiments. Thus far, no UED experiments with a resolution less than 100 fs has been demonstrated.

The recent development of short-pulse laser technology has opened new areas of light matter interaction using high-intensity pulses. The electric fields associated with such laser pulses are intense enough for almost instantaneous plasma formation, where the motion of electrons can be relativistic in the laser field. A number of phenomena in relativistic optics and plasmas may occur subsequently including wakefield generation, relativistic self-focusing, nonlinear self-phase modulation and high harmonic generation, to name but a few. Understanding these phenomena is crucial to the

development of new technologies utilizing relativistic laser plasma interactions, such as laser-driven accelerators and advanced radiation sources. One of the major advantages of laser-plasma-based acceleration is that the charge separation in plasmas can support very high acceleration gradients many orders of magnitude greater than those in conventional accelerator technology and it has the potential for making the future accelerators "compact". On the other hand, high-intensity lasers have extended the study of optical responses in material from bound electrons (perturbative regime) to plasma (i.e., free electrons), a highly nonlinear optical medium. Consequently, new plasma-based optical elements are being developed for light amplification and manipulation of its temporal and spatial properties.

1.2 Laser wakefield acceleration

Laser wakefield acceleration (LWFA) is a successful method for accelerating electrons to relativistic energies over a very short distance. In LWFA, an electron bunch "surfs" on the electron plasma wave generated by an intense laser, and gains energy. It was first suggested by Tajima and Dawson [2] more than three decades ago. The accelerating electric field strength that the plasma wave can support can be many orders of magnitude higher than that of a conventional accelerator, which makes plasma based accelerators an exciting prospect as an advanced accelerator concept. Earlier experiments using longer laser pulses (picosecond duration) accelerated electrons via a self-modulation instability, where the laser pulse length was much longer than the relativistic plasma wavelength λ_p, i. e., $c\tau \gg \lambda_p \approx 2\pi c/\omega_p$ [3–7].

It was not until high-power short-pulse lasers (sub-100 fs) became available, that high quality electron beams with quasi-monoenergetic spectra ($\Delta E/E < 5\%$ [8–10]), small transverse emittance ($< 1\,\pi\,\mathrm{mm}\cdot\mathrm{mrad}$ [11]), up to GeV energies [12–15] were produced in experiments in the so-called the "blowout" or "bubble" regime [16]. Efficient generation of large amplitude wakefields and acceleration of electrons in the

blowout regime requires a laser pulse that is both intense and short, with the energy of the laser pulse in a volume on the order of λ_p^3. In typical experiments, the intense laser pulse is loosely (with focal spot diameter of 10 μm and larger) focused into a gas jet, gas cell or capillary waveguide. The densities of such gaseous targets typically provide electron plasma densities around $10^{18} - 10^{19}\,\mathrm{cm}^{-3}$, indicating that short-pulse ($\sim$30 fs) laser systems with pulse energies on the order of a Joule or more are necessary. However, although highly competitive in terms of accelerating gradient, beams from laser wakefield accelerator experiments are currently inferior to conventional accelerators in terms of other important characteristics, such as energy spread and stability. In addition, due to constraints in high-power laser technology, experimental demonstrations have predominantly been performed in single shot operation, far below the kHz-MHz repetition rates of conventional accelerators.

Thanks to advances in laser technology producing high energy pulses at even shorter duration (sub-10 fs), LWFA experiments using an OPCPA type few-cycle laser system were recently demonstrated [17] to produce tens-of-MeV electron beams as was predicted in the original theory paper on the "bubble" regime [16]. Scaling laws and numerical studies [18, 19] indicate that using a laser pulse shorter than 10 fs, the pulse energy required to drive wakefield acceleration of electrons in a nonlinear relativistic plasma wave can be lowered to sub-100 mJ levels. Recent numerical studies [20] of electron acceleration using few-millijoule, few-cycle laser pulses shows production of relativistic electrons in the 5-10 MeV range. As high-average power laser technology continues to be developed, using lower pulse energies will undoubtedly be an important part of the efforts to bring LWFA to kHz repetition rates using existing or near-term technologies.

Most experimental work to date has been performed using pulse energies greater than 100 mJ, which limits the operation to a low repetition rate (0.03–10 Hz), often in a single-shot fashion because of existing laser technology. In this thesis, we explore

laser wakefield acceleration driven by femtosecond laser pulses with only a few millijoules. High-power ultrafast laser systems at this pulse energy level can operate at a repetition rate of a few kilohertz or higher. Compared to single-shot experiments, this high data rate capability provides better statistics and a superior signal-to-noise ratio and enables the use of new diagnostics and experimental techniques. Ultimately many proposed applications of laser accelerator sources require operation at very high repetition rates and good stability. These aspects will also be addressed in the research presented in this thesis.

1.3 Dissertation outline

This dissertation describes experimental work performed using the Relativistic λ^3 laser system at the Center for Ultrafast Optical Science (CUOS), University of Michigan. The outline of the thesis is as follows:

- Chapter II introduces fundamental physics and concepts that are pertinent to this thesis, including topics such as high-intensity laser technology, laser ionization physics, plasma oscillations and waves, nonlinear effects in relativistic laser plasma interaction and electron diffraction basics.

- Chapter III describes the laser system, experimental configuration, diagnostics and methods used in this thesis.

- Chapter IV presents a novel pulse compression scheme utilizing ionization nonlinearity and dynamic spatial pulse shaping. Experimental results are discussed, followed by supporting simulation investigation using 3D particle-in-cell codes.

- Chapter V describes the work on wakefield electron acceleration using millijoule laser pulses at 0.5 kHz repetition rate, including experimental implementation,

diagnostics and characterization of electron properties. The acceleration mechanism was also investigated using numerical methods.

- Chapter VI covers a series of experiments investigating the use of wavefront manipulation to control the laser plasma dynamics, in particular the optimization of the electron acceleration and pulse compression experiments in the previous chapters. An adaptive genetic algorithm was modified and employed for the optimization processes.

- Chapter VII focuses on the feasibility of using laser accelerated electrons as an ultrafast probe in dynamic studies of crystalline structures. Results from proof-of-principle experiments of static electron diffraction are discussed. A time-resolved experiment was performed to study a non-equilibrium optical-field-ionized plasma by electron deflectometry. Temporal characterization of the electron bunches was implemented using this technique.

- The final chapter draws conclusions and gives an outlook for future potential development and improvement of a laser-plasma based electron source.

CHAPTER II

Basic Concepts

2.1 High-intensity lasers

The decade following the invention of the laser in 1960 saw a rapid increase (see Fig. 2.1) in laser intensity as a consequence of two key technological developments, namely Q-switching and mode-locking, which led to the production of pulsed lasers enabling significant amounts of energy be concentrated into very short pulses. Over the past 40 years, great advances have been made such that the laser pulse duration has been reduced from the nanosecond regime (Q-switching) to as short as a few femtoseconds using the technique of Kerr-lens mode-locking with Ti:Sapphire crystals. By the early 1980s, the peak power and focused intensity reached a plateau limited by the optical damage from nonlinear effects in the amplifier. A successful technique, known as chirped-pulse-amplification (CPA), for amplifying ultrashort laser pulses invented in 1985 [21], triggered new growth in peak power and focused intensity.

The meaning of the term "high-intensity laser" has evolved with advances in laser technology, and depends on the particular state of matter with which the light interacts. Whereas "high intensity" could refer to an electron quiver energy around 1 eV, where the laser electric field is comparable to the Coulomb binding potential of the atom; in the context of this thesis, it is used to refer to laser fields that directly accelerate electrons to the order of the electron rest-mass energy $m_e c^2 \sim$

0.5 MeV. As ever more intense laser fields became available, increasing by more than ten orders of magnitude over the past 20 years, a wide variety of underlying physical regimes became accessible, from nonlinear optics in molecules and bound electrons to relativistic plasmas. Examples of some physical processes are shown in Fig. 2.1 for their intensity dependence.

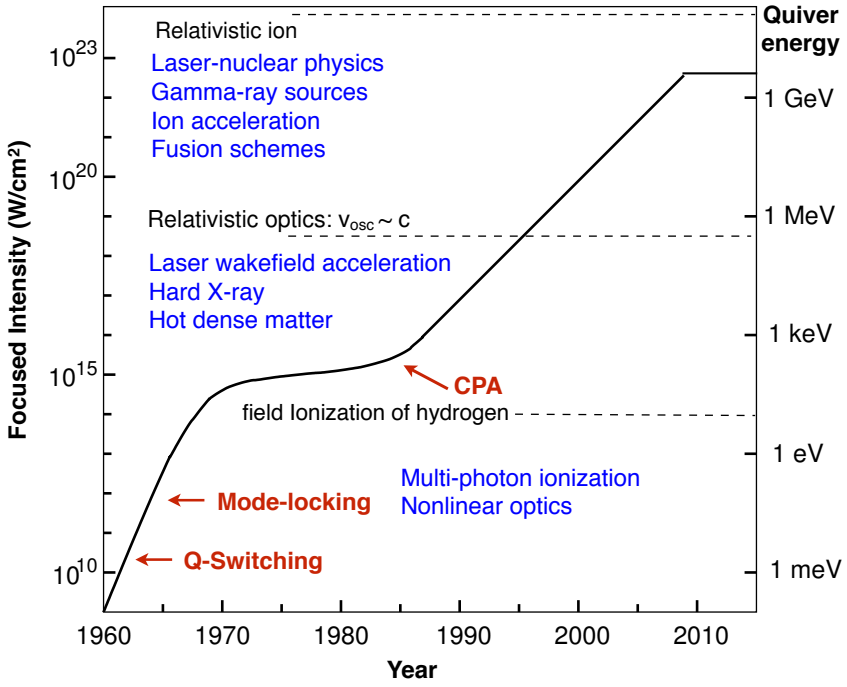

Figure 2.1 Laser intensity vs. years (adapted from Ref. [22]).

The CPA concept, which is illustrated in Fig. 2.2, is implemented in almost all high power laser amplifier systems, including the laser system used in this thesis. A short laser pulse produced by the oscillator is first temporally stretched (chirped) by a dispersive system (stretcher) such as an imaged pair of gratings before undergoing amplification. The temporal stretching reduces the peak intensity greatly so that the chirped pulse can be amplified without causing damage in the amplifiers. Another pair of diffraction gratings (compressor) is used to re-compress the amplified pulse to produce a short pulse with very high peak power. Using this technique, a focused

intensity as high as $2 \times 10^{22}\,\mathrm{W/cm^2}$ [23] has been demonstrated.

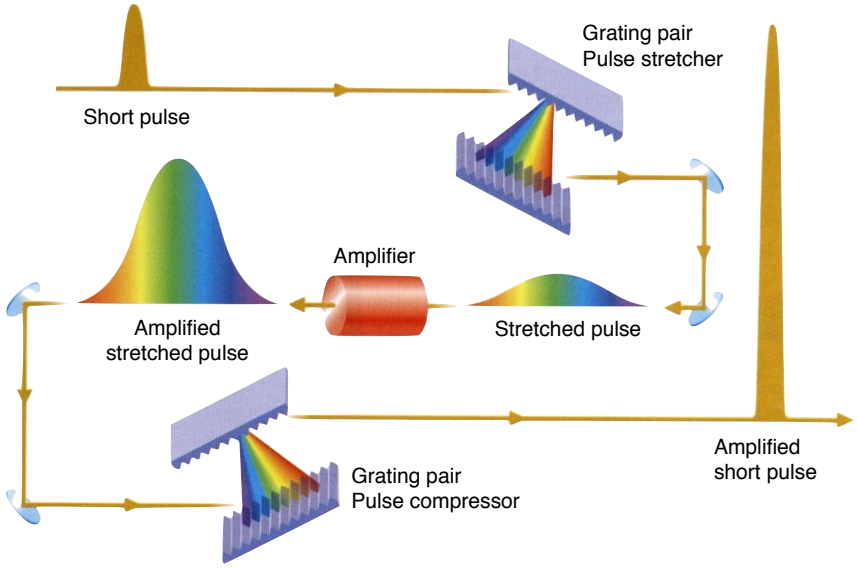

Figure 2.2 Schematic diagram of chirped pulse amplification laser system. A short pulse is first chirped using a stretcher to disperse the different frequency components that make up the short pulse. The temporally stretched pulse undergoes amplification. Finally the amplified pulse is sent to a matched compressor, where all frequency components are recombined, yielding the original short duration. The high energy short pulse is then delivered for experiments.

Titanium-doped sapphire (Ti:S) is a lasing medium typically employed in CPA-based amplifier laser systems as the oscillator and the amplifier gain media because of its wide gain bandwidth, high thermal conductivity and excellent optical properties. Cryogenic cooling of the Ti:S crystal enables amplified pulse energies up to 20 mJ at kHz repetition rates [24].

Given the spectrum of the pulse, the lower limit of the pulse duration is governed by the Fourier transform limit $\Delta\omega\Delta t \geq 1$. For standard Ti:S based CPA systems efficiently lasing around a central wavelength of 800 nm, the minimum pulse duration is typically greater than 20 fs and is limited by the amplifier gain bandwidth. Shorter pulse durations (sub-10 fs) can be obtained at high-energy levels using post-compression methods or extending conventional CPA techniques by using optical parametric amplifiers (OP-CPA) [25, 26]. Other schemes such as Raman amplifica-

tion in plasmas [27, 28], incorporating fiber lasers [29–32] or a combination of various techniques [33] have also been identified for potential future laser technologies to reach unprecedented extreme intensities.

2.2 Laser ionization mechanisms

Ionization is the process whereby an atom or a molecule becomes negatively or positively charged by gaining or losing electrons. Here we limit our discussion to the laser ionization process - one of the most important light-matter interactions. The famous photoelectric effect explained by Einstein [34] is the simplest picture of single-photon ionization, where, if the photon energy exceeds the ionization potential of an atom (similar to the work function of metal for photoelectric effect), atoms can be directly ionized (or emit photoelectrons). For light with wavelengths in the infrared to visible part of the spectrum, the photon energy is much lower than typical ionization potentials, but a nonlinear ionization process can occur where two or more photons are absorbed simultaneously, known as multiphoton ionization (MPI). This process was predicted by Göppert-Mayer [35] in the early 1930s but only observed experimentally after the invention of the laser provided light radiation that was sufficiently intense. If the laser electric field strength is large enough, ionization can be viewed according to a tunneling model (tunnel ionization). The intense electric field distorts the atomic or molecular potential barrier in such a way as to allow an electron to tunnel through the barrier. The schematics of the ionization processes are shown in Fig. 2.3 for multi-photon ionization and tunnel ionization.

The cycle averaged quiver energy of a free electron in the presence of a linearly polarized laser field is given by,

$$U_p = \frac{e^2 E^2}{4 m_e \omega_0^2} \tag{2.1}$$

where e is the electron charge, E is the electric field amplitude of the driving laser,

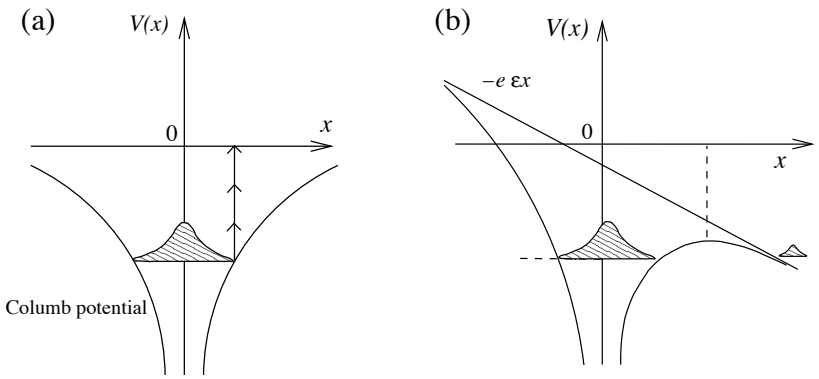

Figure 2.3 (a) Multiphoton ionization process: simultaneously absorb n photons with energy $\hbar\omega$. (b) Tunneling or barrier suppression ionization.

ω_0 is the laser angular frequency and m_e is the electron mass. U_p is referred to as the ponderomotive potential associated with the laser field. Note this energy depends inversely on the square of the laser frequency.

The theory of ionization from electromagnetic waves originates from the pioneering work by Keldysh [36]. It is shown that tunnel ionization in an alternating electric field and the multiphoton ionization can be parameterized by the Keldysh parameter,

$$\gamma_K = \frac{\text{tunnelling time}}{1/2 \text{ laser cycle}} = \frac{\omega_L}{\omega_t} = \sqrt{\frac{I_p}{2U_p}} \tag{2.2}$$

where ω_L is the laser frequency and $2\pi/\omega_t$ is the time of electron tunneling through a potential barrier. It can be written as the ratio between the ionization I_p and the ponderomotive potential U_p. Multiphoton ionization prevails at $\gamma_K \gg 1$, whereas for values of $\gamma_K \ll 1$, tunnel ionization is the dominant mechanism, which is the regime of laser intensity used in this thesis.

Using the tunneling model, one can estimate the ionization rate W in the presence of an alternating electric field. In experiments, the measurable quantity is the ionization probability p. In the case of the laser field, this depends on the properties of the laser focal conditions as well as its temporal profile. Considering a 1D Gaussian

laser pulse for simplicity, p can be related to W - particularly the time-dependence of p can be found via $W[E(t)]$, where $E(t)$ is the envelope of the laser field, using the slowly varying envelope assumption (SVEA).

Let $N(t)$ be the number of non-ionized atoms, the rate of ionization can be expressed as,

$$-\frac{dN(t)}{dt} = W(t)N(t) \tag{2.3}$$

Then the ionization probability at time t is,

$$p(t) = 1 - \frac{N(t)}{N(-\infty)} = 1 - \exp\left(-\int_{-\infty}^{t} W(t')dt'\right) \tag{2.4}$$

For a short pulse laser that has the electric profile $E(t)$, because the recombination time is much longer than the pulse duration, we can rewrite the upper limit of the integral to give the fraction of ionized electrons after the laser pulse,

$$p = 1 - \exp\left(-\int_{-\infty}^{+\infty} W[E(t)]dt\right) \tag{2.5}$$

A formula for the ionization rate W for complex atoms and atomic ions developed by Ammosov, Delone, and Krainov [37, 38] (ADK model), can be written, in a simplified form (s-state, linearly polarized field), using the original notation in Ref. [39],

$$W_{\mathrm{ADK}} = \sqrt{\frac{2n^{*3}F}{\pi Z^3}}\frac{FD^2}{8\pi Z}\exp\left(-\frac{2Z^3}{3n^{*3}F}\right) \tag{2.6}$$

where $n^* \equiv Z/\sqrt{2E_i}$ is the effective principal quantum number, $D \equiv (4eZ^3/Fn^{*4})^{n^*}$, Z is the charge of the atomic core, E_i the atomic ionization potential and F is the laser field strength in atomic units (see Appendix A).

Now substituting Eq. (2.6) into Eq. (2.5) with $E(t) = E_0 \exp[-2\ln(2)\frac{t^2}{\tau_p^2}]$ and using a full-width-at-half-maximum (FWHM) pulse duration $\tau_p = 30\,\mathrm{fs}$, we can calculate

the ionization probability for each state of argon atom as a function of the peak intensity, as shown in Fig. 2.4. The ionization probability is a rapidly increasing function of the laser intensity, in an almost stepwise fashion. A threshold intensity can be obtained from the barrier suppression ionization (BSI) model [40] by simply equating the maximum barrier potential to the ionization potential I_p,

$$\begin{aligned} I_{\mathrm{BSI}} &= \frac{cI_p^4}{128\pi e^6 Z^2} \\ &= 4.00 \times 10^9 \frac{I_p^4[\mathrm{eV}]}{Z^2} \end{aligned} \tag{2.7}$$

where the intensity is in the unit of W/cm^2.

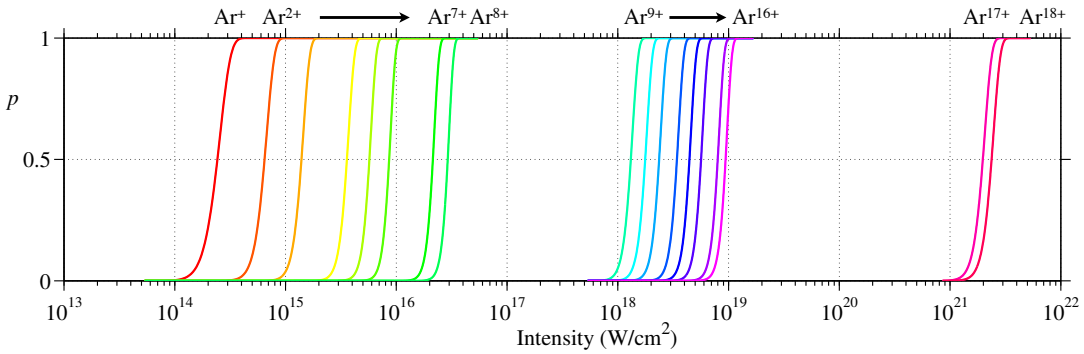

Figure 2.4 Ionization probability for different charge states of argon atoms as a function of laser intensity for a 30 fs pulse.

In Fig. 2.5, we compare the BSI threshold intensity with results from the ADK model for four types of gas atoms (H, He, N and Ar). The appearance intensity calculated using the BSI model can be used as a good approximate for the threshold intensity at which the ionization probability is 1. The small discrepancy may come from the fact the ADK model includes the tunneling effect while BSI does not. Ionization occurs at the threshold intensity for the BSI model, which does not depend on the pulse duration.

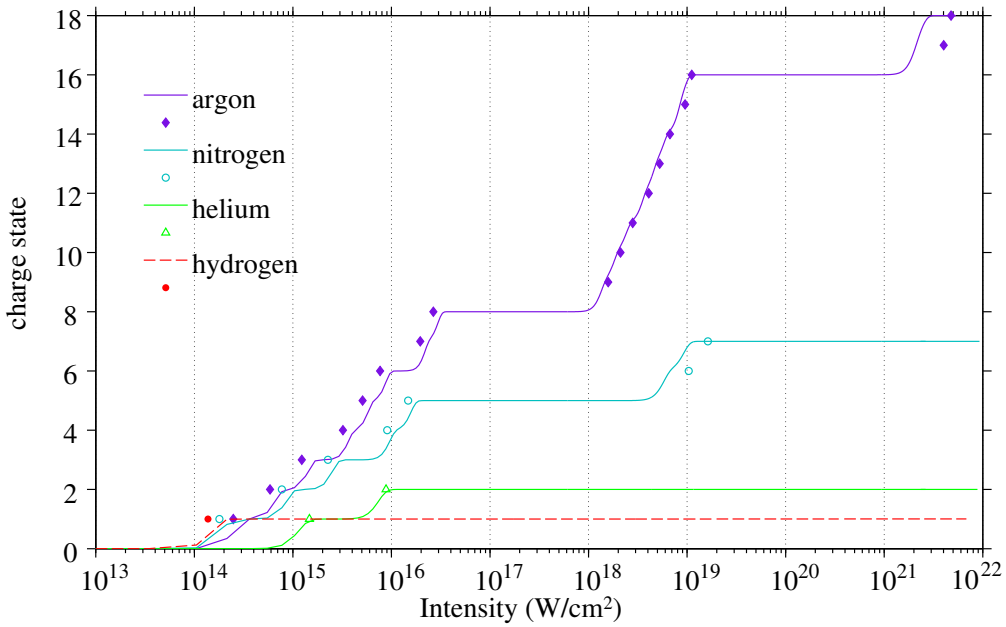

Figure 2.5 Intensity dependence for optical field ionization of argon, nitrogen, helium and hydrogen calculated using the BSI and ADK models. The values of appearance intensity (threshold intensity from the BSI model) are shown as data points for each charge state. The curves show the calculated ionized state using the ADK model plotted against the peak intensity of a 30 fs pulse.

2.3 Single electron dynamics in a laser field

Once the electron is set free from the atomic nucleus, the classical dynamics of its motion in an external electromagnetic field are given by the Lorentz equation,

$$\frac{d\mathbf{p}}{dt} = -e(\mathbf{E} + \mathbf{v} \times \mathbf{B}) \tag{2.8}$$

where $\mathbf{p} = \gamma m_e \mathbf{v}$ is the electron momentum, $\mathbf{v}$ is the electron velocity and $\gamma = (1 - v^2/c^2)^{-1/2}$ is the relativistic factor. The magnetic component of the Lorentz force (right-hand-side of Eq. (2.8)) is negligible in the linear regime. In a laser field, the electron undergoes quiver motion driven by the oscillating electric field of the laser with the angular frequency ω. Thus we can obtain the quiver velocity of the

electron oscillatory motion using the leading order equation $d\mathbf{p}_q/dt = -e\mathbf{E}$,

$$v_{\rm osc} = \frac{eE}{m_e\omega} \tag{2.9}$$

In the discussion of intense laser fields, an important parameter is the normalized vector potential a_0,

$$a_0 \equiv \frac{eA}{m_e c} = \frac{eE}{m_e\omega c} \tag{2.10}$$

For relativistic results, we should replace m_e with γm_e in Eq. (2.9). Now we have $a_0 = \gamma v_{\rm osc}/c$. The laser field strength becomes relativistic when $a_0 \geq 1$, or the quiver energy is equal to or greater than the electron rest mass energy. In practical units, a_0 is related to the intensity I and the wavelength λ of the light through,

$$a_0 = \left[\frac{I\lambda^2}{1.37\times 10^{18}\,{\rm W/cm^2}\cdot\mu{\rm m}^2}\right]^{1/2} \tag{2.11}$$

Now let us consider a second-order perturbation, using $\mathbf{p} = \mathbf{p}_q + \delta\mathbf{p}$ and the first-order motion expressed in the vector potential $\mathbf{p}_q = m_e c\mathbf{a}$. The second-order momentum is [41],

$$\begin{aligned}\frac{d\delta\mathbf{p}}{dt} &= -\left(\frac{\mathbf{p}_q}{m_e}\cdot\nabla\right)\delta\mathbf{p} - \mathbf{p}_q\times(c\nabla\times\mathbf{a}) \\ &= -m_e c^2\nabla(a^2/2)\end{aligned} \tag{2.12}$$

The time average of this equation is known as the ponderomotive force (in the linear limit),

$$\mathbf{F}_p = -m_e c^2\nabla\langle a^2/2\rangle \propto -\nabla I \tag{2.13}$$

Here $\langle\ \rangle$ denotes the average over the period of the laser. The relativistic generaliza-

tion of the ponderomotive force is derived in Ref. [42],

$$\mathbf{F}_p = -\frac{m_e c^2}{\bar{\gamma}} \nabla \langle a^2/2 \rangle \tag{2.14}$$

where $\bar{\gamma} = (1 + \langle p^2 \rangle / m_e^2 c^2 + \langle a^2 \rangle)^{1/2}$ is the time averaged relativistic factor. The ponderomotive force is thus proportional to the gradient of laser intensity and expels particles in the direction of lower intensity.

2.4 Laser driven plasma waves and electron acceleration

In this section, the theoretical basis for laser wakefield acceleration is presented. The physics of laser driven plasma accelerator was recently reviewed by Esarey *et al.* in Ref. [41]. Here we will cover some important aspects pertinent to the work in this thesis.

2.4.1 Linear and nonlinear plasma waves

A plasma oscillation known as plasma wakefield can be excited through the ponderomotive force of an intense laser pulse propagating in a plasma, with a characteristic frequency,

$$\omega_p = \frac{e^2 n_e}{\epsilon_0 m_e} \tag{2.15}$$

where n_e is the equilibrium electron density.

In the linear limit where the density perturbation is small, $\delta n/n_0 = (n - n_0)/n_0 \ll 1$, using the cold fluid equation and the expression of ponderomotive force, Eq. (2.12), the solution of the linear wakefield can be given,

$$\delta n/n_0 = (c^2/\omega_p) \int_0^t dt' \sin[\omega_p (t - t')] \nabla^2 a^2(\mathbf{r}, t')/2 \tag{2.16}$$

From this result, it can be shown the plasma wave will be generated most efficiently

for an optimum pulse duration that is on the order of the plasma wavelength, $\lambda_p = 2\pi c/\omega_p$. Transversely, the wake extends over a spatial scale on the order of the laser spot size. Using the Poisson equation $\nabla \cdot \mathbf{E} = -e\delta n/\epsilon_0$, the maximum longitudinal electric field from this sinusoidal wave gives the cold, nonrelativistic wave breaking amplitude,

$$E_{max} = mc\omega_p/e \tag{2.17}$$

which scales with the plasma density as $E_{max}[\mathrm{V/m}] = 0.96\sqrt{\mathrm{n_e}[\mathrm{cm}^{-3}]}$.

As the laser intensity is increased, a considerable fraction of the background density can be displaced, and the linear perturbation treatment $\delta n/n_0 \ll 1$ is no longer valid. The plasma wave and its evolution becomes highly nonlinear. In 1D, the maximum electric field associated with a nonlinear plasma wave can be shown using the nonlinear relativistic cold fluid equations to be [43],

$$E_{wb} = \sqrt{2}(\gamma_p - 1)^{1/2} E_{max} \tag{2.18}$$

where $\gamma_p = (1 - v_{ph}/c)^{-1/2}$ is the relativistic Lorentz factor associated with the phase velocity of the plasma wave.

For nonlinear plasma waves in 3D, numerical analysis and simulations are usually required. In a highly nonlinear regime where $a \gg 1$, electrons can be fully expelled by the ponderomotive force of the laser pulse [44], leaving an ion sheath "bubble" from complete electron cavitation. The electric fields in the cavitation region can be simplified to linear ramp functions in all directions, providing both longitudinal acceleration and radial focusing for ideal electron acceleration [16].

2.4.2 Wave breaking

As previously mentioned, the maximum electric field in a longitudinal plasma oscillation is limited by wave breaking. A one-dimensional derivation will give us

some useful insight. Consider the 1D continuity equation,

$$\frac{\partial n_e(z,t)}{\partial t} + \frac{\partial}{\partial z}[n_e(z,t)v_z(z,t)] = 0 \tag{2.19}$$

In the wave frame of a 1D nonlinear plasma wave at the phase velocity v_{ph}, using a transformation of coordinates, $\xi = z - v_{ph}t$ and $\tau = t$, we can rewrite the partial derivatives in Eq. (2.19) with $\partial/\partial t = \partial/\partial\tau - v_{ph}\partial/\partial\xi$ and $\partial/\partial z = \partial/\partial\xi$. Now Eq. (2.19) becomes

$$\frac{\partial}{\partial\xi}[n_e(v_{ph} - v_z)] = \frac{\partial n_e}{\partial\tau} \tag{2.20}$$

The right-hand side of Eq. (2.20) can be dropped assuming the plasma quantities do not change very much during the transit time of the plasma electrons through the laser pulse (the quasistatic approximation) such that the fluid quantities mainly depend on the frame variable ξ. Then the left-hand side of this equation can be integrated using the initial condition ($n_e = n_0,\ v_z = 0$),

$$n_e(v_{ph} - v_z) = n_0 v_{ph} \tag{2.21}$$

This can be rearranged so,

$$\frac{n_e}{n_0} = \frac{1}{1 - v_z/v_{ph}} \tag{2.22}$$

where n_0 is the unperturbed background density. This means that as the electron fluid velocity v_z becomes equal to the phase velocity of the wave v_{ph}, the local plasma density will go to infinity, corresponding to wave breaking. This effect can result in the reduction of the wave amplitude or a complete loss of the coherent wave structure. It is an important mechanism by which the background plasma electrons can be self-injected and accelerated in the plasma waves. Thermal effects can reduce the threshold for wave breaking when there is a finite velocity spread in the oscillating electrons [45]. In addition to 1D analysis, multi-dimensional effect can also lead to

transverse wave-breaking [46], whereby electrons are injected from the sides of the wave due to the phase front curvature in 2D or 3D.

2.4.3 Electron trapping and acceleration

Once an electron is injected into the plasma wave, it can be accelerated and gain energy in the appropriate phase. When the electron travels past half a period of the plasma wave and enters the region of a decelerating field, it is known as dephasing. The electron dynamics in the wake can be elucidated by examining a test particle interacting with a 1D nonlinear plasma wave [47]. Using the quasistatic approximation (a transform of variables using $\xi = z - v_{ph}t$), it can be shown that,

$$\frac{d}{d\xi}(\tilde{\gamma} - \tilde{p}\beta_{ph} - \tilde{\phi}) = 0 \tag{2.23}$$

where $\beta_{ph} = v_{ph}/c$ is the phase velocity of the wave, $\tilde{\phi} = e\phi/mc^2$ is the normalized electrostatic potential of the wake, and $\tilde{\gamma} = \gamma/mc^2$ and $\tilde{p} = p/mc$ are the normalized energy and momentum respectively. This expression means that the Hamiltonian is conserved for a set of trajectories in the phase space $(\tilde{p}, \xi)$ and it is determined by the initial conditions of the particle. Electrons that have sufficient momentum can be trapped in the wave, appearing as closed orbits in the phase-space. The maximum energy gain for a trapped electron estimated using the threshold orbit that lies at minimum electrostatic potential, can be given as [47],

$$\gamma_{max} \simeq (1 + \beta_{ph})\gamma_{ph}^2 \Delta\phi \tag{2.24}$$

where $\Delta\phi = \phi_{max} - \phi_{min}$ is the maximum potential difference of the plasma wave.

2.5 Laser propagation in ionizing plasma

The propagation of the laser in a medium is governed by the refractive index η. As discussed in the previous section, plasma density can be modified through the ponderomotive force of the laser pulse, which will in turn affect the laser pulse propagation.

The dispersion relation for a plane wave in a cold, unmagnetized, collisionless plasma is given by,

$$\omega_0^2 = \omega_p^2 + k_0^2 c^2 \tag{2.25}$$

where ω_0 is the laser frequency and ω_p is the plasma frequency. The critical plasma density $n_c = m_e \epsilon_0 \omega_0^2 / e^2$ is found when $\omega_0 = \omega_p$. With the expressions for phase velocity $v_{ph} = \omega/k = c/\eta$, we can obtain the plasma refractive index,

$$\eta = \sqrt{1 - \frac{\omega_p^2}{\omega_0^2}} \tag{2.26}$$

When the index of refraction varies with the intensity of the laser, nonlinear optical effects come into play. As we shall see, a plasma can be a highly nonlinear optical medium, whereby the index of refraction can be changed through the electron density, laser intensity, or frequency. Including variations of the plasma density and relativistic mass correction, a number of these nonlinear effects can be summarized by considering the expanded plasma refractive index [48],

$$\eta = 1 - \frac{\omega_p^2}{2\omega_0^2}\left(1 + \frac{\delta n}{n} - \frac{\langle a^2 \rangle}{2} - 2\frac{\delta \omega_0}{\omega_0}\right) \tag{2.27}$$

where δn is the density perturbation.

In this expression, the term with a^2 represents the relativistic effective mass associated with electron quiver in the laser field, and is responsible for relativistic self-focusing [44, 49] for an appropriate transverse laser profile. The term with the den-

sity perturbation can contribute to a variety of transverse effects depending on the density variation, such as self-channeling [50], plasma wave guiding [51] or plasma defocusing [52]. The last term is responsible for the group velocity dispersion due to broadband light.

In addition to the transverse effects, a longitudinal gradient in the refractive index gives rise to a variation in the phase velocity, leading to a frequency shift. This effect is known as self-phase modulation. In ionizing plasmas, one self-induced effect is ionization induced blue shifting [53]. The frequency shift from a varying index is given by [54],

$$\Delta\omega = -\frac{\omega_0}{c}\int \frac{\partial\eta}{\partial t}(z)dz \tag{2.28}$$

where z is the longitudinal distance. An ionizing laser front creating free electrons producing a rapidly decreasing refractive index, results in $\Delta\omega > 0$.

In the case of a plasma wave, the maximum frequency shift has the form $\Delta\omega/\omega_0 \propto -d\delta n/d\xi$ [55] in the wave frame coordinate $\xi = z - v_{ph}t$, hence the electron density gradient $d\delta n/d\xi$ will give rise to local frequency upshift or downshift depending on the sign, leading to pulse compression [56] and photon acceleration [57, 58].

2.6 Electron diffraction basics

Electron diffraction is a technique that can be used to study the structure of crystals, using the wave nature of an electron. For an electron with a momentum of p, the electron wavelength is given by the de Broglie relation, $\lambda_e = h/p = h/\gamma\beta m_e c$, where h is the Planck constant. The wavelength is about 0.04 Å for electrons at 100 keV. Kinematic electron diffraction analysis [59, Ch. 2] follows the theory of Bragg's law as found in X-ray diffraction, which gives the relation between the scattering

angle θ and the crystal inter-planar spacing d,

$$2d\sin\theta = n\lambda,\ n = 1, 2, 3... \tag{2.29}$$

where λ is the wavelength of the incident electron. The inter-plane distance d depends on the crystal structure. For example, a cubic crystal system (e.g., aluminum and gold metals) with the lattice constant a, the spacing between Bragg planes with Miller indices (hkl) is given by,

$$d_{hkl} = \frac{a}{\sqrt{h^2 + k^2 + l^2}} \tag{2.30}$$

The pattern of diffraction represents the reciprocal Fourier domain related to the structure of the crystalline lattice in real space. The amplitude of the diffracted beams can be viewed as the Fourier component of the electrostatic potential of the atoms, which is given by, for elastic scattering with N atoms,

$$A(\mathbf{s}) = \sum_{j=1}^{N} f_j^{(e)}(s)\exp(-i2\pi\mathbf{s}\cdot\mathbf{r}_j) \tag{2.31}$$

where $f_j^{(e)}$ is the atomic scattering factor for the jth atom and $\mathbf{s}$ is the scattering vector having a magnitude $s = 2\sin\theta/\lambda$. The measured quantity in diffraction experiments is the intensity $I(\mathbf{s}) = |A(\mathbf{s})|^2$. In a single crystalline sample, where the atoms are arranged in an orderly lattice, the scattered electron waves constructively interfere such that the diffraction pattern peaks at specific angles determined by the Bragg condition, as diffraction spots. On the other hand, a polycrystalline material, composed of a large number of single crystal grains at random orientations, will generate many overlapping diffraction spots to form a diffraction pattern of concentric rings. Inelastic scattering and multiple scattering may cause broadening of the Bragg peak and a diffuse background. Their contribution is usually insignificant for very thin samples and high-energy electron diffraction.

In time-resolved electron diffraction, the change in the position and width of the diffraction peak as well as the diffracted intensity can reflect structural dynamics of the sample. For example, a reduction in the diffracted amplitude may be caused by thermal disordering (Debye-Waller effect).

CHAPTER III

Methods

This chapter describes the laser system, experimental configuration and diagnostics as well as the computational modeling methods used in this thesis.

3.1 The λ^3 laser system

All experiments discussed in this dissertation were performed using the Relativistic Lambda Cubed (λ^3) laser system at the Center for Ultrafast Optical Science of the University of Michigan. The λ^3 laser produces 30 fs pulses of 800 nm light at a repetition rate of 500 Hz. The laser system has an ASE (Amplified-Spontaneous-Emission) intensity contrast of $\sim 10^8$ around 1 ns before the main pulse. A diagram of the laser system is shown in Fig. 3.1. The system is seeded by a FemtoLasers Ti:sapphire oscillator, which generates 12 fs pulses and has a companion carrier envelope phase (CEP) locking system. An RF addressable acousto-optic programmable dispersive filter (AOPDF) called a "Dazzler" controls the spectral amplitude and phase of these pulses. Selected pulses from the Dazzler train are stretched to 220 ps in a low-aberration stretcher and amplified to 7 mJ in a cryogenically cooled large-mode regenerative amplifier (Regen). The energy dumped from the Regen cavity is "cleaned" in a Pockels cell and used to seed a 3-pass amplifier that delivers up to 28 mJ pulses to the compressor. The total efficiency of the compressor is 71% after four

reflections and the output 20 mJ pulses are trimmed to 18 mJ at the perimeter of a 47 mm-diameter deformable mirror (DM). Throughout the system, pump light is provided by a variety of internally doubled Nd-doped YAG, YLF and vanadate lasers, as shown in Fig. 3.1. The output beam with its controllable wavefront is then delivered to one of five experimental areas for the production of x-rays, electron beams, ion beams, THz radiation, high-order harmonics, or warm-dense matter.

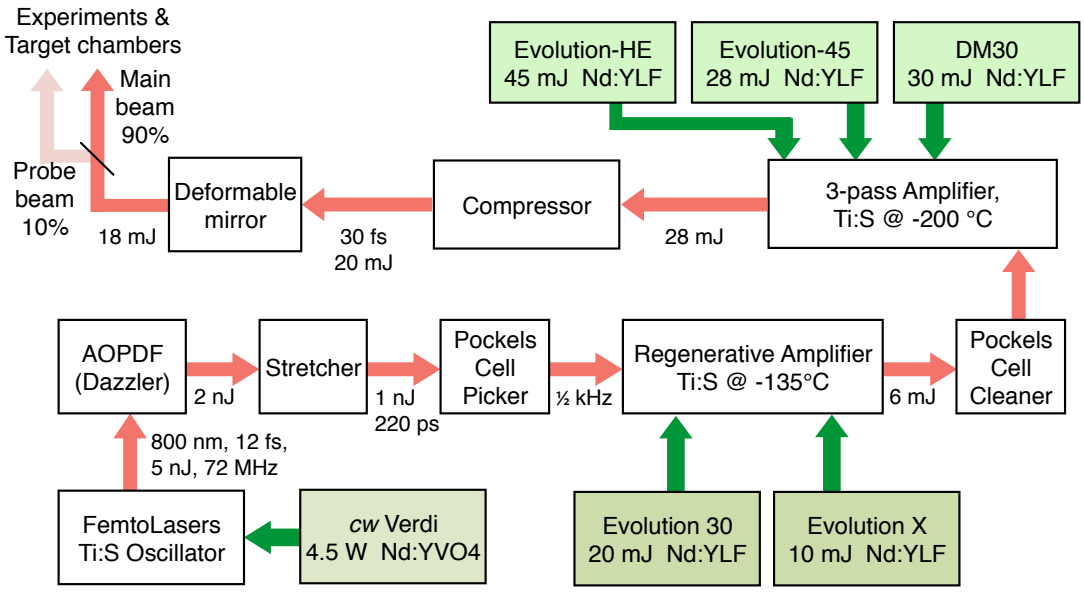

Figure 3.1 Schematic of the λ^3 laser system.

As part of the laser system, the deformable mirror (AOA Xinetics, Northrop Grumman) has a silver coated face sheet with 37 piezoelectric actuators arranged on a square grid spaced 7 mm apart. The actuators are PMN (lead magnesium niobate) ceramic capable of delivering 4 μm of mechanical stroke at 100 V. The mirror surface shape is controlled by setting 37 independent voltage values for the actuators with a computer LabView program.

3.2 Setup of the experiments

Experiments were conducted in a cylindrically shaped vacuum chamber. A circular optical breadboard having a 56 cm diameter (22 inches) is mounted inside the vacuum chamber. The output laser pulse reflected off the deformable mirror is transported to the experimental chamber by 2 silver coated mirrors and through an optical window port made of low dispersion material (magnesium fluoride, MgF_2). An $f/2$ off-axis parabolic mirror with protective gold coating is used to focus the light to a spot size of the order of a few micrometers. The focal spot can be optimized by iteratively setting the DM so that the signal of second-harmonic generation from a BBO crystal is maximized. Details on the spot optimization and characterization will be discussed in chapter VI.

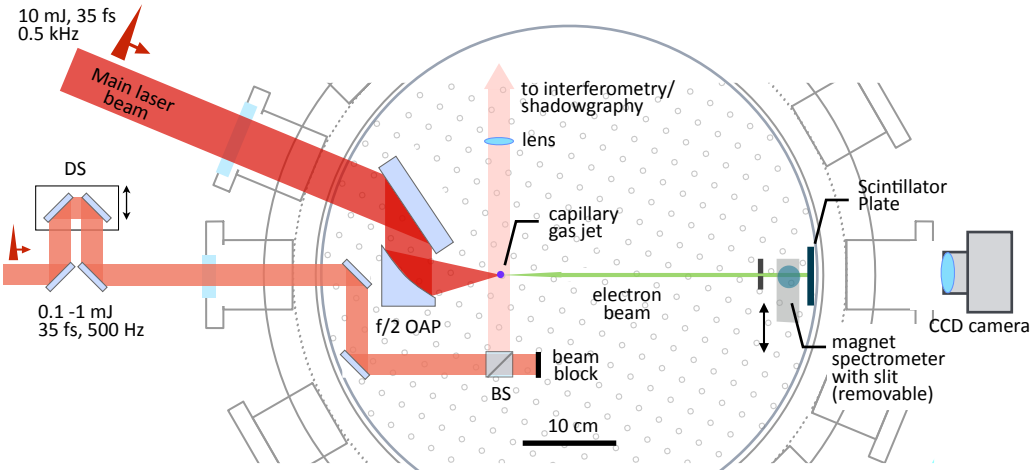

Figure 3.2 Layout of the experimental chamber (top view). Shown for major components of an electron acceleration experiment including the focusing optics, gas jet target and the electron detection system. Inside of the vacuum chamber is drawn to scale. OAP: off-axis parabolic mirror; BS: beamsplitter cube; DS: delay stage.

Fig. 3.2 shows a schematic sketch of the experimental chamber. A probe beam split from the main laser beam using a $2\,\mu$m thick nitrocellulose pellicle (National Photocolor) contains variable energies from a few percent up to 10% of the main beam by tuning the angle of reflection. An optical delay stage is installed in the

probe beam path to control its relative timing to the main pulse. The synchronized probe pulse is telescoped to a beam diameter of roughly 20 mm and further split into two copies using a polarization beam splitter cube (Thorlabs PBS252). A half-wave plate is placed in the probe beam to control the energy splitting ratio between the two copies. One of them is delivered transversely to the interaction region for plasma shadowgraphy or interferometry; the other is reserved for pump-probe time-resolved experiments (blocked in Fig. 3.2). Taking into account other energy losses during beam transport using multiple silver and gold mirrors, up to 8 mJ pulse energy was delivered on the target (after the focusing paraboloid) for the experiments described in this thesis. This gives a peak intensity as high as 3×10^{18} W/cm^2 using the $f/2$ focusing.

3.3 Gas target

For laser plasma experiments in the under-dense regime (electron densities up to a few $10^{19}\,\mathrm{cm}^{-3}$ for 800 nm laser light), the targets usually consist of a capillary discharge plasma or a gas jet/cell. Tailoring appropriate density profiles for these gaseous targets has become an active research topic in itself for laser plasma applications and poses some engineering challenges. For single-shot experiments on larger-scale laser systems, pulsed gas targets driven by supersonic solenoid nozzles are typically used [60].

Due to the nature of the experiments using fast focusing optics at a high repetition rate in this thesis, a simple nozzle was designed using a segment of fused silica capillary tubing, which has an inner diameter (ID) of 100 μm. An approximately 1 cm length of this tubing is mounted on a standard compression fitting to a 30-cm-long flexible stainless steel tubing (1/16″ inner diameter) and connected to the gas delivery system. During experiments, gas continuously flowing out of the tubing serves as the target. The gas flow experiences free expansion into vacuum and different densities

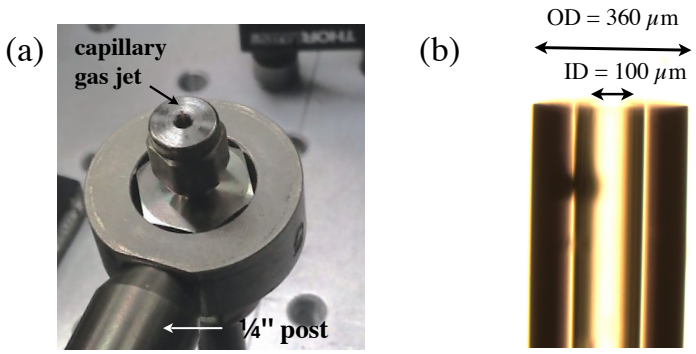

Figure 3.3 (a) Picture of the capillary gas jet assembly. (b) A microscope image of the capillary tubing.

are achieved by varying the backing pressure. A turbomolecular pumping (Varian V550) system is placed on the top of the gas jet to provide efficient evacuation of gas inside the chamber. The configuration of the gas delivery system has a flow rate that allows operation of the experiments at an acceptable vacuum level (typically below 1 millitorr) as the chamber pressure reaches equilibrium. The gas jet is mounted on a motorized XYZ translation stage that is used to manipulate the target positioning to an accuracy of 2 μm.

3.4 Plasma density characterization

The vertical plane at the main pulse propagation axis is imaged using the transverse probe beam with a single lens imaging system (focal length $f = 15\,\text{cm}$, N.A=6). The transverse imaging beam is sent to a Michelson interferometer for measuring the plasma density. The interferogram data provide information on both the plasma spatial distribution and its temporal evolution, by varying the optical delay. Alternatively if one arm of the Michelson interferometer is blocked, a plasma shadowgram is obtained.

In the Michelson setup of the plasma interferometry, one arm of the probe beam is flipped or offset such that the interaction region interferes with a reference region

with no plasma. The phase difference induced by the plasma can be recorded in the fringe shift. The phase shift accumulated for light traveling along a path l in a plasma can be written as

$$\delta\phi = \frac{2\pi}{\lambda}\int (\eta - 1)\, dl \tag{3.1}$$

where λ is the probe beam wavelength, $\eta = \sqrt{1 - n_e/n_c}$ is the refractive index of the plasma. Hence, by retrieving the phase difference $\delta\phi$ from the interference fringe, one can calculate the plasma density.

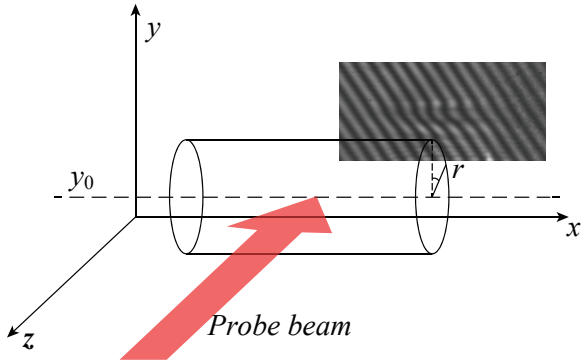

Figure 3.4 Abel inversion geometry for the transverse plasma interferometry. The ionizing laser pulse is propagating along the $x-$axis.

An example of the interferogram and the geometry of the transverse probing is shown in Fig. 3.4. We implemented the Fourier-transform method [61] to extract the two-dimensional phase difference information $\delta\phi(x, y)$ from the measured interferogram, which is a projection of the phase shift along the path of the probe beam. Since the shape of a laser produced plasma channel is typically axisymmetric, one can determine the plasma density in three dimensions through an Abel inversion:

$$\delta\phi(x, r) = -\frac{1}{\pi}\int_{y_0+r}^{\infty} \frac{d}{dy}\left[\delta\phi(x, y)\right] \frac{1}{\sqrt{(y - y_0)^2 - r^2}}\, dy \tag{3.2}$$

Using the expression for the plasma refractive index and assuming $n_e \ll n_c$ (under-

dense plasma), we can rewrite Eq. (3.1)

$$\delta\phi(x,r) = \frac{2\pi}{\lambda}\left(\sqrt{1-\frac{n_e(x,r)}{n_c}}-1\right)dl \approx -\frac{\pi}{\lambda}\frac{n_e(x,r)}{n_c}dl \tag{3.3}$$

This gives us a simplified relationship between $n_e(x,r)$ and $\delta\phi(x,r)$.

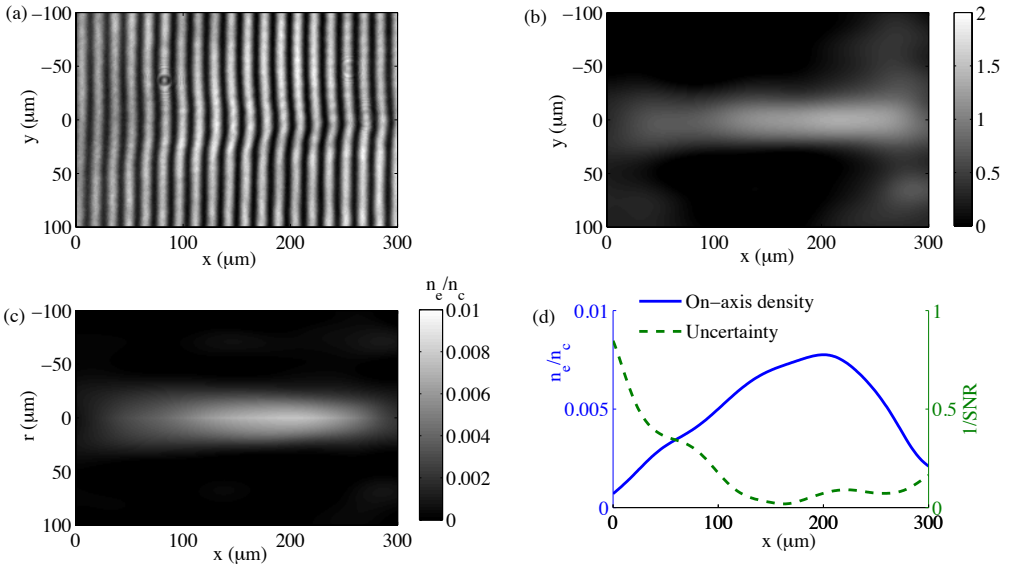

Figure 3.5 (a) Measured interferogram with fringe shift; (b) Extracted phase shift map $\delta\phi(x,y)$; (c) Reconstructed electron density map $n_e(x,r)$; (d) Electron on-axis density $n_e(x,r=0)$ (solid blue line) and the ratio of the phase retrieval noise to the on-axis maximum phase shift for $\delta\phi(x,y)$ (dashed green line).

The fringe analysis and subsequent Abel inversion are carried out in MATLAB. The Abel inversion is implemented using two different methods. The first one relies on the analytical form of an Abel inversion of a Gaussian function by fitting the measured phase shift to a Gaussian profile. The fitting method is noise-resistant, and gives a rough estimate for the maximum density without including details on the shape of distribution (Gaussian is assumed). For the second method, we compute the Abel inversion numerically, following a modified version of the method in Ref. [62] to include a second-order correction for data with small non-axisymmetry. As seen from Eq. (3.2), numerically evaluating an Abel inversion involves differentiation, which can

be sensitive to noise. Some smoothing is necessary before the experimental data can be used for the Abel inversion. Additionally, data have been processed and analyzed using the IDEA 1.7 software, a freeware developed by Hipp *et al.* [63]. Unless otherwise stated, the plasma densities quoted in this thesis refer to the maximum on-axis peak electron densities from either extrapolation or direct reconstruction using measured interferogram data. The results of the reconstructed densities using different methods may vary by up to ±20% at signal-to-noise ratios greater than 5. Other systematic errors include phase-shift induced by the gas molecules in the beam path.

Fig. 3.5 shows a typical measured interferogram and the retrieved plasma density in our experiments. Note that because the plasma scale is smaller as compared to gas targets typically used in laser wakefield experiments with 10-100 TW class lasers, the resultant phase shift is more difficult to measure at lower plasma densities because of the low signal-to-noise ratio. We have estimated the plasma densities through extrapolation rather than direct measurement for some of our experimental conditions. The retrieved electron density can be approximated by a Gaussian profile along the propagation axis with a FWHM of 100-300 μm.

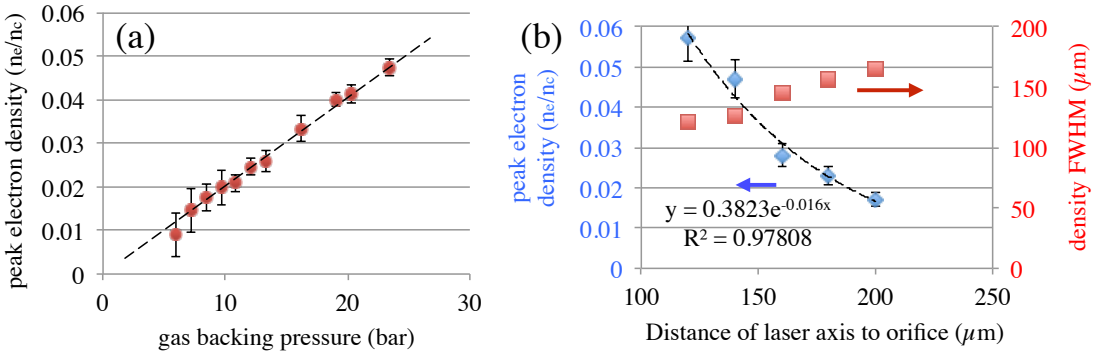

Figure 3.6 (a) Peak plasma electron density as a function of backing pressure (gas used: helium). (b) Peak electron density and FWHM as a function of the distance from laser focus to the orifice.

The plasma density profile can be varied by changing the gas backing pressure and the relative height of the laser axis to the orifice of the capillary nozzle. In Fig. 3.6(a),

we plot the peak electron density as a function of the gas backing pressure for a fixed focus position. Fig. 3.6(b) shows the density dependence as a function of the distance to the orifice from the focus, for both the maximum density and the profile width.

3.5 Optical characterization

3.5.1 Laser focal spot

The laser focal spot (far-field profile) can be measured by a microscope objective lens after the laser energy has been sufficiently attenuated to avoid damaging the optics. Absolute calibration on the magnification is performed by translating the objective lens by a known distance and recording corresponding images. The focusing parabolic mirror can be properly aligned by scanning through focus and correcting astigmatism. Additional wavefront correction can be employed using the deformable mirror to further optimize the focal spot, as discussed in Chapter. VI. An example of the laser spot is shown in Fig. 3.7 for a best manually aligned focus without the deformable mirror engaged.

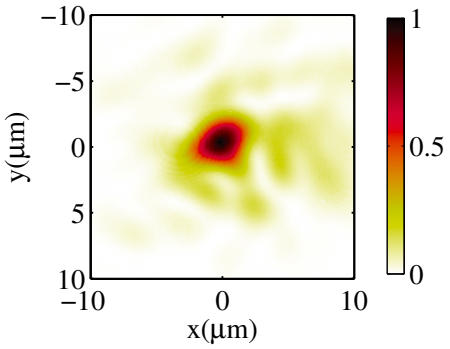

Figure 3.7 CCD image of a laser spot focused by the $f/2$ parabolic mirror. The deformable mirror is at 0 V for all actuators.

3.5.2 Transmitted light

Measurement of the transmitted light, including far-field imaging, transmitted optical spectrum and complete temporal characterization using frequency resolved optical gating (FROG), is performed, in particular for the pulse compression experiments described in Chapter IV. Due to the space limitations of the experimental chamber, optical measurements were not performed simultaneously with the electron experiment setup. The input beam configuration with the gas jet is identical to the electron experiment (see Fig. 3.2). The setup for optical diagnostics is illustrated in Fig. 3.8. The transmitted laser beam is re-collimated by a second off-axis parabolic mirror and transported out of the chamber through a 0.5 mm thick fused silica glass window (to keep dispersion as low as possible). Three different diagnostics can be selected by using the two flipping mirrors in the output beam path (1) near-field imager; (2) an integrating sphere with a miniature spectrometer (OceanOptics USB4000); (3) the FROG measurement (SwampOptics model 8-9-thin-USB).

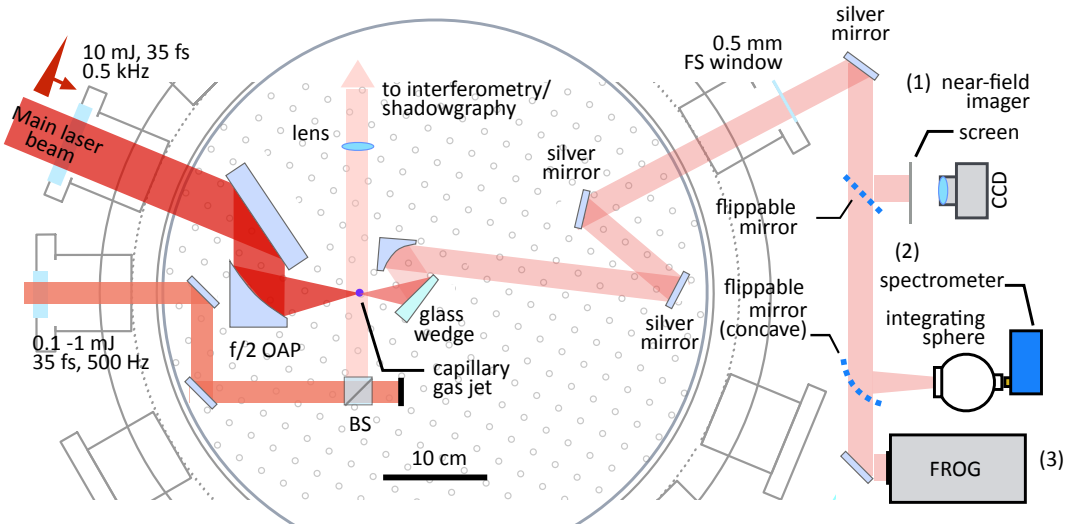

Figure 3.8 Layout of the experimental setup for optical characterization. OAP: off-axis parabolic mirror; BS: beamsplitter cube; FS: fused silica. (1) near-field imaging; (2) spectral measurement; (3) FROG measurement.

Frequency Resolved Optical Gating

Frequency resolved optical gating (FROG) [64] is a robust technique for *complete* characterization of the time-dependent intensity and phase of a femtosecond pulse. The basic principle of ultrashort optical pulse (duration on the order of 10 fs) characterization is to use the pulse itself as a probe and produce some kind of autocorrelation such that information of the pulse can be retrieved. Unlike an intensity autocorrelator, where proper retrieval of the pulse duration requires *a priori* assumption of the pulse shape, FROG does not need additional information on the pulse to be measured. It is a widely employed method based on spectrally resolving a noncollinear intensity autocorrelation in a nonlinear-optical medium. A generic beam geometry for a second-harmonic-generation (SHG) based FROG is shown in Fig. 3.9. In SHG-FROG, the corresponding spectrogram signal (also called a FROG trace) is given by

$$I_{\mathrm{SHG-FROG}}(\omega,\tau) = \left| \int_{-\infty}^{\infty} E(t)E(t-\tau)\exp(-i\omega t)dt \right|^2 \tag{3.4}$$

Then the time-dependent electric field can be reconstructed from the measured FROG trace using an iterative algorithm similar to a two-dimensional phase-retrieval problem. The SHG-FROG has an ambiguity in the direction of time as its trace is always symmetric with respect to the time axis as seen in Eq. (3.4). However, it can be removed, for example by introducing a pre- or post-pulse. The pulse measurement in this thesis is performed using a commercial single-shot SHG-FROG device (SwampOptics).

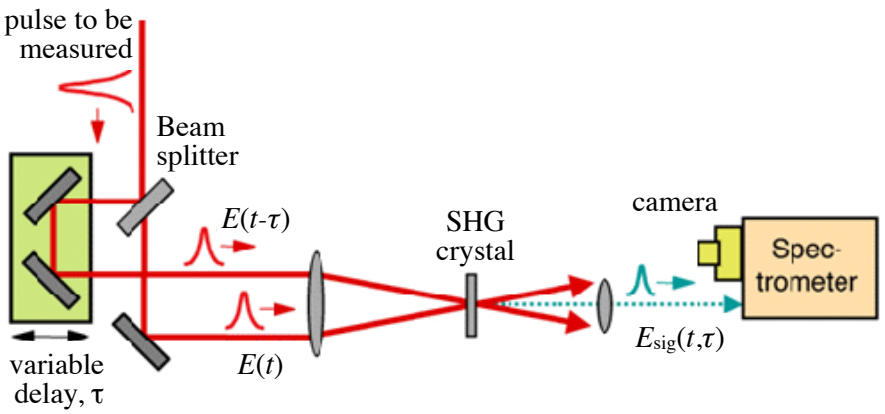

Figure 3.9 Basic principle of operation of SHG-FROG. Figure courtesy of `http://www.swampoptics.com/tutorials_FROG.htm`.

3.6 Diagnostics of electron beams

3.6.1 Detection of electrons

Electron beam emission profiles are measured on a scintillating screen that is imaged on a CCD camera by a telephoto lens. For most of the experiments, high-resolution electron images are obtained using a scintillating plate (FOS, Hamamatsu J6677), which consists of a protective film and a CsI(Tl) scintillator plate deposited on top of a fiber optic plate (FOP). The emission spectrum of the scintillator peaks at a wavelength of 550 nm. We also use Kodak LANEX screens as the electron scintillator. The active scintillating material in LANEX is a layer of Gd_2O_2S that emits photons at a wavelength around 545 nm. LANEX is covered with a protective aluminum foil for laser shielding during the experiments. The imaging system is properly light shielded to block any light from the laser and other sources. A BG39 glass filter is placed before the CCD camera to block fundamental laser light.

Alternatively, an image plate (IP, Fujifilm BAS-SR 2025) can be used to record the electron profile. Image plates are a type of phosphor film that uses photo-stimulated luminescence (PSL) to store the pattern of the deposited energy, which can be read

out by illuminating a laser in an IP reader. Despite of the advantages of IP for its high sensitivity and dynamic range, it must be removed for readout and therefore cannot provide real-time results. IPs are less useful for high-repetition-rate experiments described in this thesis and only used as a method for cross calibration of the electron charge or the energy distribution.

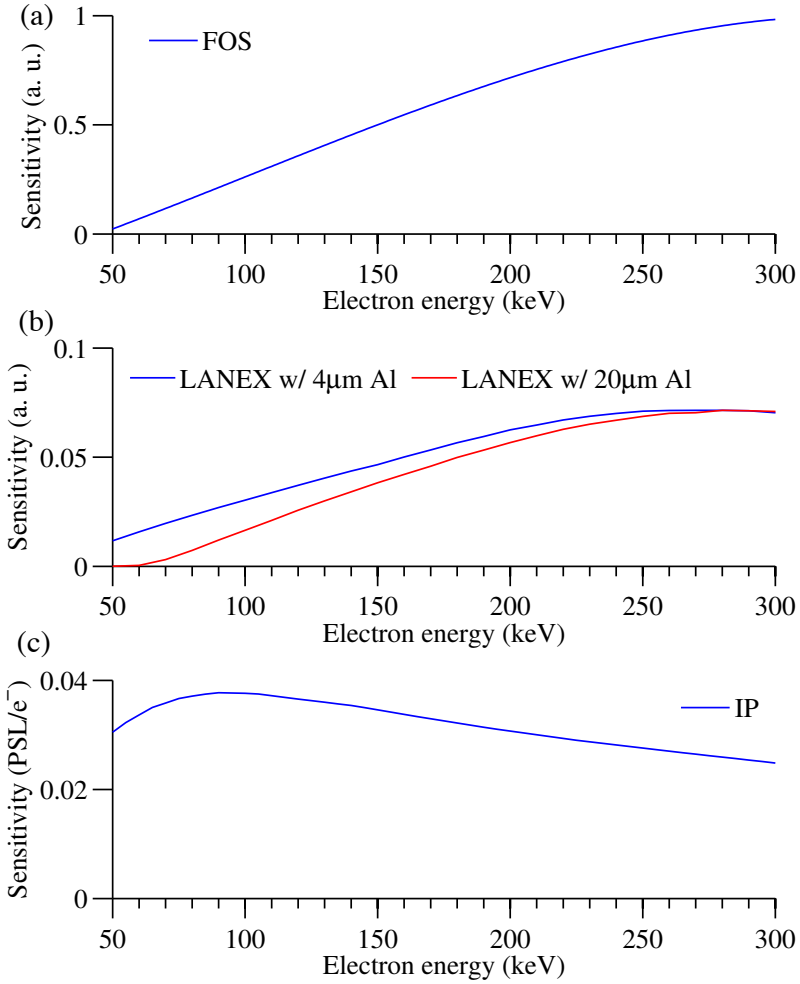

Figure 3.10 Sensitivity response of various detectors for electrons in 50-300 keV. (a) FOS plate; (b) LANEX screen covered by a 4 μm or 20 μm thick aluminum foil; (c) image plate.

The response of the FOS to electrons was calibrated using an electron microscope in the range 50-300 keV (performed by J. Faure at LOA, Palaiseau, France). The detector has a very small response below 50 keV so that in practice, electrons below

50 keV were not detected. We used this calibrated response to obtain the absolute number of electrons per shot as well as in the deconvolution of the electron distribution data. The sensitivity of LANEX screen was modeled with Monte Carlo simulations using the code EGSnrc [65]. This is important because the response of scintillators is far from flat when the electron energy is comparable to the energy deposited in these materials [66, 67]. For image plates, photo-stimulated luminescence (PSL) values are directly obtained during the read-out process and an absolute electron number can be obtained using the sensitivity calibration performed by Tanaka *et al.* [66]. The fading effect of IP signal is included for calibration, which is also described in Ref. [66]. For imaging using FOS plate or a LANEX screen, absolute charge calibration requires additional information including the photon collection efficiency (NA of optics, filter response etc.) and CCD response (quantum efficiency, gain etc.). The measured or computed sensitivity curves for all three types of electron detectors used are plotted in Fig. 3.10.

3.6.2 Electron spectrometer

The electron spectrometer is the apparatus used to measure the energy distribution of the electron beam. For high-energy electrons traveling at some fraction of the speed of light, a dipole magnet is often used as the spectrometer. Electron trajectories in a magnetic field can be computed using the Lorentz equation, Eq. (2.8). The magnetic field map is measured by a gaussmeter (LakeShore Model 425). Energy calibration of the spectrometer can be obtained numerically using a 2D particle tracking code written in MATLAB or the 3D particle-tracing module from the commercial software COMSOL Multiphysics (version 4.3b) [68]. Depending on the range of electron energies to be measured, the magnetic strength should be carefully chosen to give a reasonable resolution. An additional entrance aperture or slit is typically used to improve the resolution.

For experiments in Chapter V, two configurations are employed for the electron spectrometer. In one configuration, the spectrometer is composed of a pair of 20-mm-diameter disc magnets yoked together (providing a 25 mT magnetic field in the middle of the gap). To improve the spectral resolution, a 0.5 mm aluminum slit was mounted vertically at the entrance of the magnetic field. In an alternative configuration, the magnetic spectrometer [69] is used in conjunction with an image plate, which has an entrance collimator with 3 mm diameter and 5 mm length.

3.7 Computational modeling

3.7.1 Introduction

Due to the complexity of the nonlinear and kinetic processes that can occur during the interaction of a high-intensity laser or particle beam with plasma, computational modeling can be very important, especially in situations such as the 3D nonlinear regime where analytical solutions do not exist. Computer simulations can help understand the fundamental physical processes and interpret experimental results.

The particle-in-cell (PIC) method [70] is a widely used technique to model complex laser plasma interactions. This method tracks the motion of a collection of charged particles (so-called macro-particle) in self-consistent electromagnetic fields on a particle-mesh grid. The PIC scheme has the basic steps as follows:

1. Particle pusher: integrate the equations of motion to calculate each macro particle's position and momentum.

2. Use distribution of weighted particles on the grids to obtain currents and charge densities.

3. Field solver: solve Maxwell's equations using the currents and charge densities. Both external fields such as that of a laser pulse and the self-fields of the charged particles are included.

4. Calculate weighted fields on the grid. Go to step 1 so that each particle is advanced to a new position and momentum via self-consistently calculated electromagnetic fields.

These codes are ideally suited for complex systems with a large number of degrees of freedom and offer a fully kinetic description of multi-dimensional plasmas. The grid size should be chosen to resolve the plasma Debye length to minimize numerical heating, which can give rise to spurious effects resulting from a non-physical instability. For LWFA simulations, higher spatial resolution is usually used to resolve the laser wavelength.

3.7.2 OSIRIS 2.0 framework

For this thesis work, PIC simulations were performed using the OSIRIS 2.0 framework [71] at the Center for Advanced Computing at the University of Michigan. OSIRIS is a fully parallelized, explicit, relativistic and object-oriented PIC code that can be used in one-, two-, or three-dimensional space with all three dimensions of momentum space. Simulations can be carried out in a co-moving window, which moves at the speed of light. This feature allows efficient simulations of the evolution of the laser pulse and plasma around it in the laboratory frame for substantial propagation distances.

In the simulations relevant to this thesis, only the dynamics of electrons are included and ions are treated as an immobile background. This is valid for the laser intensity and timescales considered here and the much heavier ions can be considered stationary on the timescale of interest. Particles can be initially loaded in the simulations at the beginning, similar to a case of a pre-ionized plasma. In OSIRIS, a module of ionization physics can be optionally included to inject particles (electrons) from a tunnel ionizable fixed gas background based on the choice of ionization model (ADK, BSI, etc.). This feature is useful for modeling ionization effects.

CHAPTER IV

Self-Compression of Laser Pulses in Ionizing Plasmas

4.1 Introduction

Understanding the propagation of intense femtosecond laser pulses in gases and underdense plasmas is of crucial interest in areas such as laser driven particle acceleration [41] and attosecond pulses from high harmonic generation [72]. The nonlinear interaction of laser pulses in a transparent medium also finds useful applications in generating ultrashort pulses at high energy level via temporal compression. Although conventional Ti:sapphire based amplifier systems can generate laser pulses at joule level energies, the pulse duration is, in most cases, limited to 25 fs or longer by the gain-narrowing effect in the amplifier medium and imperfect dispersion compensation. Kerr induced self-phase modulation (SPM) and/or ionization-induced nonlinearity have been utilized as sources of spectral broadening for post-compression in plasma filaments [73], gas-filled waveguides [74] or bulk media [75]. A relativistically intense pulse driving a plasma wave can also lead to self-compression [76–83]. It is an important and challenging problem to achieve homogenous temporal pulse compression with a focusable spatial profile and high energy throughput efficiency. In addition, demonstration of a high degree of stability is of great importance. Having

a few-cycle optical pulse at the tens of millijoule energy levels is beneficial for high-repetition rate laser wakefield acceleration as shown in both numerical [16, 20] and experimental work [17].

In several recent studies [84–87], ionization induced spectral broadening for post-compression has become an attractive idea because of its potential to scale to higher energy pulses and overcome the energy limitations typically found in SPM and filamentation methods. However, since ionization also results in a transverse refractive index variation, an external guiding structure, such as a large diameter capillary waveguide, is required for moderate interaction lengths (typically on the order of 10 cm). Additional dispersion compensation using optical elements such as chirped mirrors [88] may still be necessary at the output of the waveguides [84, 85]. Alternatively, the dispersion can be self-compensated via spatio-temporal reshaping inside the capillaries [86, 89], which results in self-compression of the laser pulse.

In this chapter, we discuss experimental results and consistent particle-in-cell simulations demonstrating self-compression of a 10-mJ laser pulse in plasma using a relatively tight focusing scheme without any external guiding structures, operating at high intensities in the moderate relativistic plasma regime with $a_0 \sim 1$. A combination of ionization, refraction, focusing and diffraction in three-dimensional (3D) space leads to stable and reproducible compression from 36 fs to 16 fs. The best compression is not at focus but where the intensity corresponds to the steepest refractive change due to ionization. The spectral broadening can be mainly attributed to optical-field-ionization (OFI). The high transmission means that the pulse peak power is nearly doubled. Two of the key requirements to achieve this are the use of a very short ($\sim$100 μm) moderate density ($n_e \sim 10^{19}$ cm^{-3}) free-flowing gas jet and a fast focusing optic with a relatively large numerical aperture ($f/2$), which enables significant compression to occur without a guiding structure. This method does not suffer from limitations due to the coupling efficiency or material damage present in

a guided geometry, and consequently it can be easily implemented at high-repetition rates.

4.2 Experiment

4.2.1 Experiment setup

The experiments performed on the λ^3 laser system used pulse energies up to 10 mJ. The near transform-limited pulse duration was measured using the FROG to be 35 ± 3 fs (FWHM) - the variance comes from conditions of the Dazzler configuration and alignment of the amplifier and compressor on different experimental days. The linearly polarized laser beam was focused by an $f/2$ off-axis parabolic mirror onto expanding gas flow produced by a 100 μm diameter nozzle. The gas density was varied by setting the backing pressure. A turbo-molecular vacuum pump was placed above the continuously flowing gas nozzle to maintain an equilibrium state during experiments. Plasma densities were determined by interferometry using a transverse probe beam. On-axis electron density profiles exhibited a Gaussian distribution with a 150-300 μm FWHM, depending on the distance to the nozzle orifice.

The measurements were performed using the setup shown in Fig. 3.8. Light transmitted through the focus was collimated by a second parabolic mirror and transported out of the vacuum chamber through a 500-μm-thick fused silica Brewster window. The energy of the output pulse was measured by an optical power meter (Coherent PM30). Alternately, the collimated light was reflected by a wedged plate onto a diffuser screen for near-field mode imaging or an $f/1$ parabolic mirror to characterize its focusability. An iris diaphragm was inserted to limit the beam profile for alignment of temporal characterization in a commercial single-shot second-harmonic-generation frequency-resolved optical gating (SHG-FROG) device [64]. Optical spectra were independently recorded using a miniature spectrometer (Ocean Optics USB4000), with

the absolute spectral response across all wavelengths being calibrated in-situ for our imaging setup using a white light source.

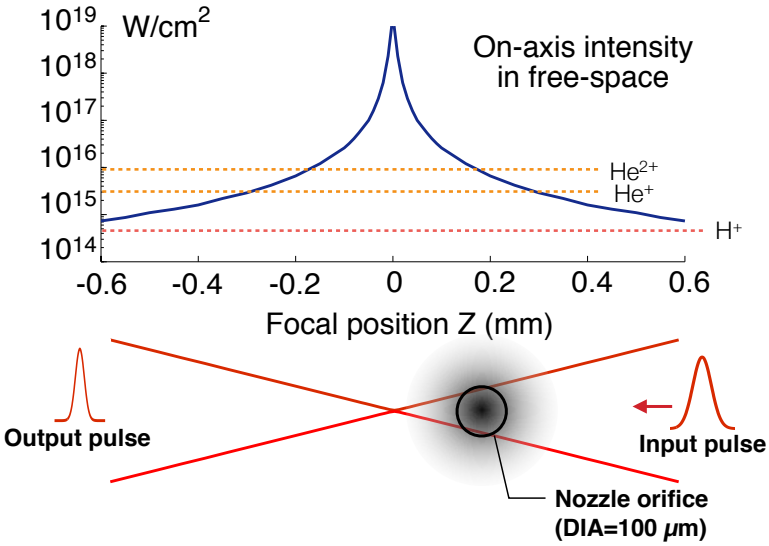

Figure 4.1 Top view schematic of the experimental configuration. Focal position Z specifies the relative distance from the center of the gas jet to the geometrical focus. A negative Z means the gas jet is behind the focus.

The configuration of the laser-gas interaction is sketched in figure 4.1. The laser intensity along the propagation axis is calculated for free-space propagation, based on the f-number of the focusing optics used in the experiments. This represents the case with ideal diffraction-limited focusing and is used only to provide a reasonable estimate for the laser intensities in the mid-field region near the focus but not the peak intensity at focus because of imperfections and aberrations of the optical systems. Although the deformable mirror can be used to correct wavefront distortion to produce a close-to-diffraction-limited focal spot (see Section 6.3 of Chapter VI), the pulse compression does not require having an optimized spot *at the focal plane* since we employed the ionization nonlinearity *in the mid-field region*. It will be shown that the wavefront of the incoming light can affect the interaction. The details of this are discussed in Chapter VI.

4.2.2 Experiment results

Three different gas species were used, hydrogen, helium and argon. For all three gases used, we have observed self-compression of the laser pulse from the FROG measurement at the output.

A typical FROG trace with and without compression is shown in Fig. 4.2 obtained using argon gas. The original pulse was measured at the same location with the gas jet turned off. The pulse was self-compressed from $\tau = 36$ fs to a near-transform-limited one with $\tau = 16$ fs under optimal conditions. The FROG retrieval algorithm was implemented using the QuickFROG software (Swamp Optics). We show in Fig 4.2(d) by comparing the measured and retrieved spectra from FROG

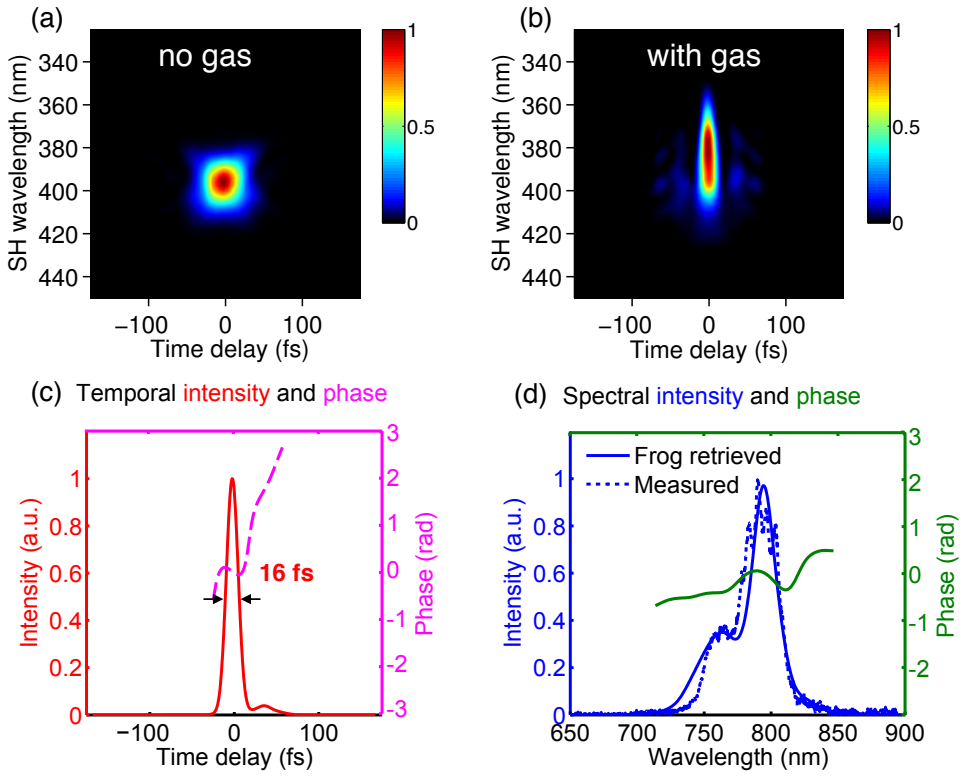

Figure 4.2 (a) The FROG trace measured at the output with no gas and (b) with gas after self-compression. (c) and (d) are the retrieved temporal and spectral intensity and phase for the self-compressed pulse. The retrieval error is 0.016 on a 128×128 grid. The measured spectrum (dotted curve) is plotted in (d) for comparison with the FROG retrieved spectrum.

that our measurements are self-consistent. Asymmetric spectral broadening with a large blue shifted component was measured for the compressed pulse.

It was found that the optimal compression depends on the focal position differently for different gas atoms. Figure 4.3 shows the measured optical spectrum and pulse duration (FWHM) as a function of the focal position. The minimum output pulse duration was found to be at a distance of 0.2–0.3 mm and 0.4–0.6 mm from the geometrical focus for He and H_2 gas respectively. Hydrogen is a gas of diatomic molecules, so it can be directly compared with helium as they provide roughly same electron density when fully ionized at the same backing pressure. Pulse compression was associated with spectral broadening, as is clearly depicted in Fig. 4.3(a) and (b) where a large blueshift of the central wavelength occurs at the optimal compression points. The spectral broadening is a consequence of new frequency components generated in the blue-shifted spectrum during optical field ionization. The influence of

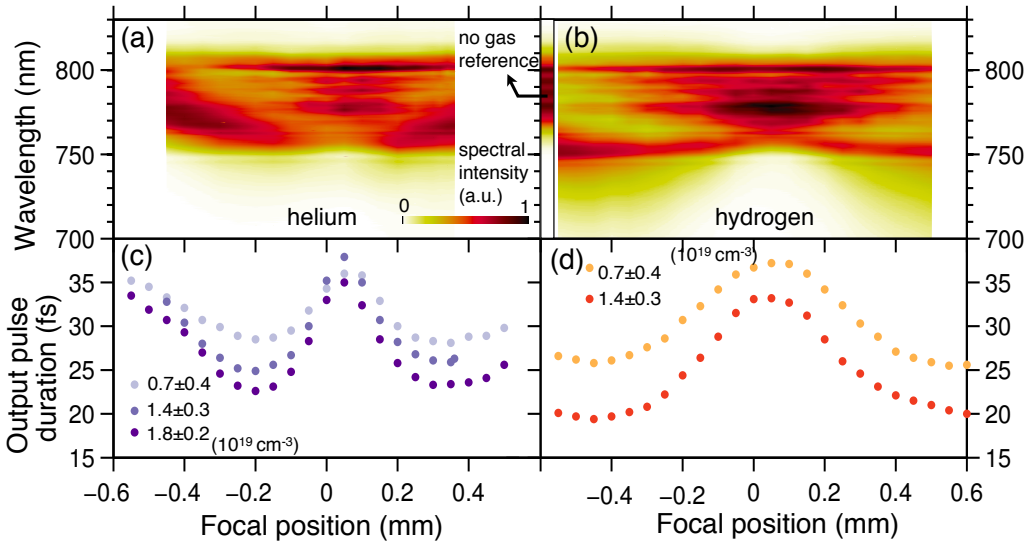

Figure 4.3 Composite images showing the measured optical spectra as a function of the focal position for (a) helium and (b) hydrogen at the same plasma density $(1.4 \pm 0.3) \times 10^{19}\,\mathrm{cm}^{-3}$. A reference spectrum obtained without gas is also shown. The output pulse duration (FWHM) as a function of the focal position for helium (c) and hydrogen (d) at various backing pressures (4.5, 6.6 and 9.0 bar for helium; 4.5 and 6.7 bar for hydrogen). The initial pulse duration was 38 fs for this data set.

the gas species can be explained by the different ionization potentials for helium and hydrogen atoms, as shown in Fig. 4.1.

The laser intensities of the barrier suppression ionization [40] [see Eq. (2.7)] threshold for hydrogen and helium (the first ionization charge state) are 1.4×10^{14} W/cm^2 and 1.5×10^{15} W/cm^2 respectively. Given one focusing position and gas type, the spectral bandwidth increases with the backing pressure (gas density), which gives more temporal compression. Similar trends were also observed using argon gas where the optimal compression was found approximately 0.2 mm from the focus.

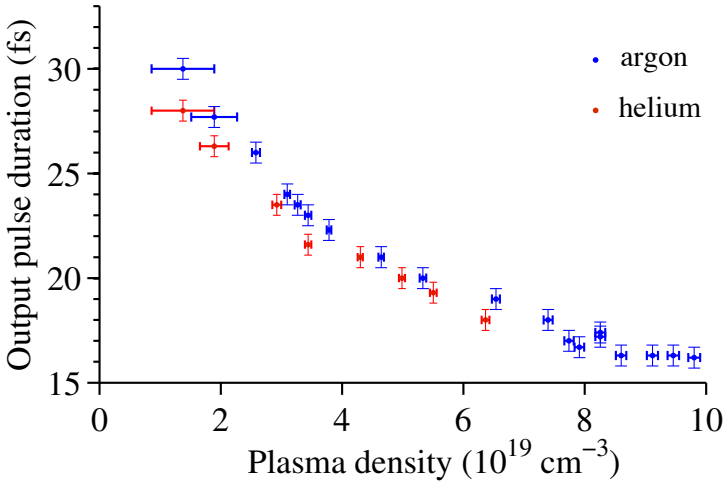

Figure 4.4 Pulse duration as a function of maximum on-axis plasma density.

Although more complex dynamics can be expected due to multiple ionization (successive ionization charge states up to 8 are achievable under our experiment conditions), under comparable plasma densities, the compression is not very sensitive to the gas species as shown in Fig. 4.4 over a range of similar plasma densities. Here, the focal position was fixed at the optimal compression point for argon at the highest densities. No stable measurement could be made with helium gas above a plasma density of 7×10^{19} cm^{-3}; a 4-fold increase in backing pressure was required for helium to provide the same plasma electron density as compared to argon, and consequently the gas flow gives a larger interaction volume. At this high gas flow rate, it was

also difficult to pump the interaction chamber as the turbo pump began to reach its operational limit.

Further increase in the density of argon was observed to cause strong modulations in the beam mode and pulse-to-pulse instability. The FROG measurement also became unreliable as the measured spectral width continued to broaden and reach the bandwidth limit of the nonlinear crystal in the FROG device, where the crystal phase matching efficiency becomes lower at shorter wavelength. The shortest stable pulse we measured was with a peak electron density around 0.9×10^{19} cm^{-3} ($\approx 0.05 n_c$) using argon. To characterize the stability of the compression, the output pulse duration as a function of time is shown in Fig. 4.5. Fluctuation in pulse duration smaller than 0.4 fs RMS was observed for the FWHM pulse duration at 16 fs.

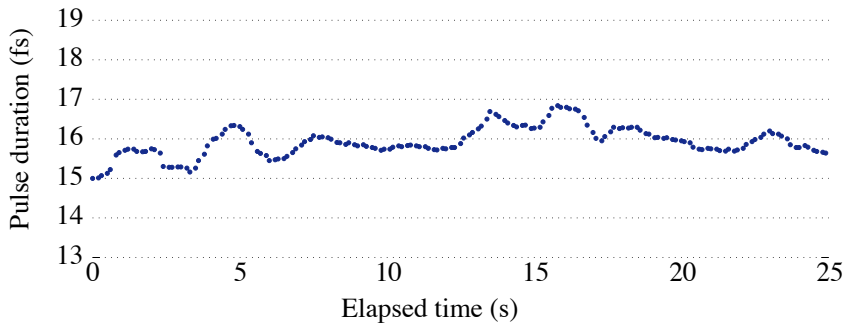

Figure 4.5 Pulse duration fluctuation after self-compression as a function of time.

The gas backing pressure was kept below 15 bar such that the near field mode of the transmitted light remained stable from shot-to-shot with good spatial quality (i.e., no strong modulation or filamentation). We also confirm that the temporal compression may be considered homogenous by measuring various locations across the beam. Fig. 4.6 shows three FROG traces measured at different parts of the output beam and the corresponding transmission spectra. The variance in the retrieved pulse durations was less than 2 fs at all transverse locations. FROG retrieval errors (RMS difference between the experimental and retrieved traces) were below 2% on a 128×128 grid for all measurements reported here.

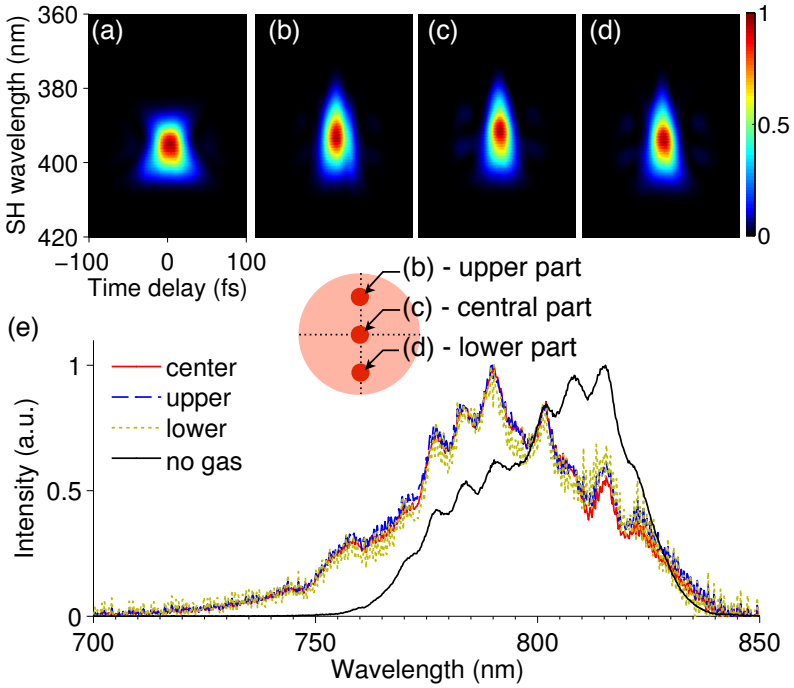

Figure 4.6 The FROG traces measured at the output with no gas (a) and with gas (argon) using (b) the upper, (c) central and (d) lower parts of the transmitted beam. (a)-(d) share the same axes. The aperture was opened to approximately a 3 mm diameter as illustrated in this figure. (e) The normalized transmission spectra measured without gas and with gas for three locations.

The absence of significant frequency downshifting (indicative of large amplitude plasma wave excitation) suggests that even higher energy efficiency might be achieved because the laser pulse is not losing energy in generating a large amplitude plasma wakefield and the subsequent trapping of energetic electrons as in the strong nonlinear relativistic regime [80, 81]. On the other hand, previous compression work employing a much lower laser intensity in filamentation processes suffered losses due to multi-photon ionization over long propagation distances, thus limiting the energy efficiency. By contrast, in the operating regime of our experiments, the peak laser intensity increases or decreases rapidly with the propagation distance and OFI occurs in the leading fraction of the pulse over a very short distance ($\sim$100 μm). Indeed we find a high total energy transmission (88% for the measurement in Fig. 4.2) measured using a power meter. The transmission was increased to 95% at half the backing

pressure, but with a lower level of compression. Moreover, our scheme is free of an external guiding structure, which eliminates any loss in compression efficiency due to imperfect coupling in previous methods.

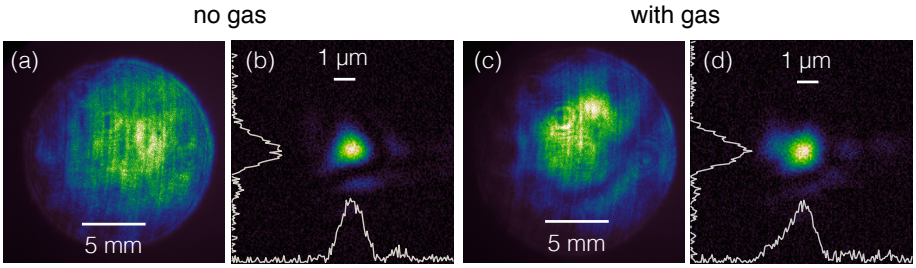

Figure 4.7 Near-field images of the output beam (a) with no gas (c) with argon at backing pressure of 12 bar. (b) and (d) are the corresponding far-field images of the re-focused beam.

The beam profile of a stable compressed pulse is shown in Fig. 4.7(a) and (c) to have a relatively smooth spatial mode. There is some modulation to the spatial profile introduced by the plasma, but in Fig. 4.7(b) and (d), we show that the focal spot shape does not change significantly from the vacuum case to that with flowing argon gas, demonstrating the excellent focusability of the transmitted beam. In both "no gas" and "with gas" cases, the optical imaging system was identical. This implies that the peak intensity can be effectively doubled after the compression. Because the process is stable, the use of adaptive optics after pulse compression can effectively correct aberrations to achieve highest possible intensities to a near diffraction-limited spot. This demonstration of the focusability of the light is clearly important for plasma based compression to be a useful practical technique.

4.3 Simulations & discussion

To interpret our experimental results, we have performed a series of 3D particle-in-cell (PIC) simulations using the OSIRIS 2.0 framework [71] including the ionization physics models. The PIC approach contains the full range of electromagnetic and

collisionless plasma physics, yet the nonlinear response of bound electrons in atoms and molecules such as the Kerr effect is not included in the codes. The ionization rate typically increases very rapidly with laser intensity. It should be pointed out that for the spatial scalelength of the gas profile in our experiments, the effect of self-phase modulation contributed by Kerr nonlinearity can be considered negligible when compared to the change of refractive index induced by ionization [90]. This validates the use of PIC codes to model our experiments. Simulations were carried out in a moving window of dimensions $64 \times 230 \times 230$ μm^3 on a Cartesian grid with step sizes $\Delta x_1 = \lambda/10$ (the propagation direction) and $\Delta x_2 = \Delta x_3 = \lambda/3$ (the transverse direction). The transverse dimension was chosen to be sufficient to contain the large diffraction angle of a tightly focused laser beam. Ionization physics can be optionally included using the ADK tunnel ionization model. For each ionization level, particles with a charge-to-mass ratio equivalent to that of an electron were used, with $2\times2\times2$ particles-per-cell. The neutral density profile has a truncated Gaussian profile with a FWHM width of 150 μm.

The reshaping dynamics of an ionizing laser pulse were first studied using numerical models based on nonlinear envelope propagation for a two-dimensional pulse [91]. It was shown in Ref. [91] that the light pulse can transform into a horseshoe or horn-type structure during its ionization process. Similar ionization induced refraction was also measured experimentally by Chessa *et al.* in [92].

Fig. 4.8 illustrates the evolution of the laser pulse structure at different propagating distances taken from a 3D simulation for the scenario when a neutral helium gas density profile is peaked 200 μm before the geometric focus (at 500 μm). The maximum gas density is $0.02n_c$, corresponding to an electron density of $0.04n_c$ when fully ionized. To visualize the local change of the laser spectrum, the frequency shift distribution at the center slice for the laser polarization plane is plotted, with a cut-off threshold at 10% of the maximum intensity, below which the frequency shift is

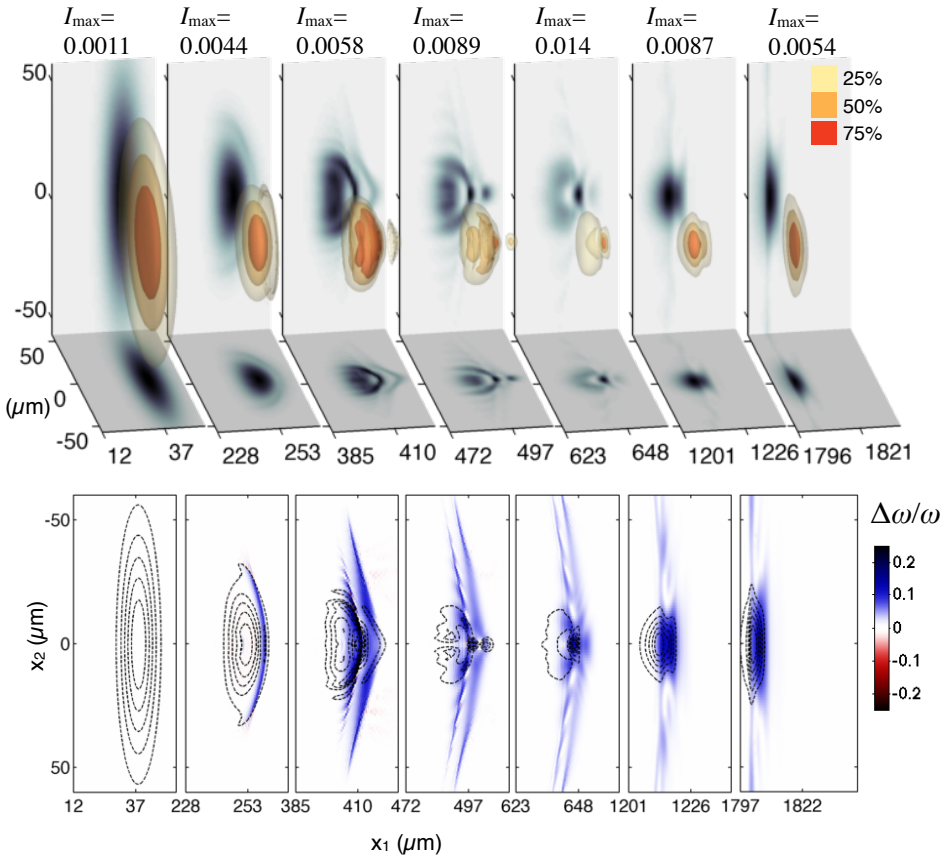

Figure 4.8 The gas peak is before laser focus (Z = 0.2 mm). Top panel: isosurface plots (25%, 50% and 75% of the maximum intensity) showing the pulse dynamics at different propagating distances. Side panels display intensity profiles at cross-sectional planes through the center of the box. Bottom panel: spatial distribution of the local frequency shift $\Delta\omega/\omega_0$ of the laser pulse for the center slice. The blue color represents frequency upshift (blueshift) and red for frequency downshift (redshift). The dashed lines are 2D contour plots for intensity profile.

not shown. As can be seen from the local frequency shift, much of the leading part of the pulse gradually becomes blue-shifted as a result of OFI during propagation through the helium gas around 300 μm. The laser pulse experiences dramatic nonlinear refraction due to a rapidly changing refractive index induced by the increasing electron density. In the meantime, as the focusing optic acts to converge the light pulse, a dynamic redistribution of the pulse energy takes place, which leads to not only an enhanced peak intensity but also a shorter temporal duration. Although

multiple structures are observed during this complex interaction, the electromagnetic field diffraction in vacuum transforms into a single mode containing most of the pulse energy. Experimentally, the pulse splitting is often associated with an increased backing pressure and/or use of a gas species with multiple ionization levels. Multiple ionization is also known to cause phase modulation of the laser pulse.

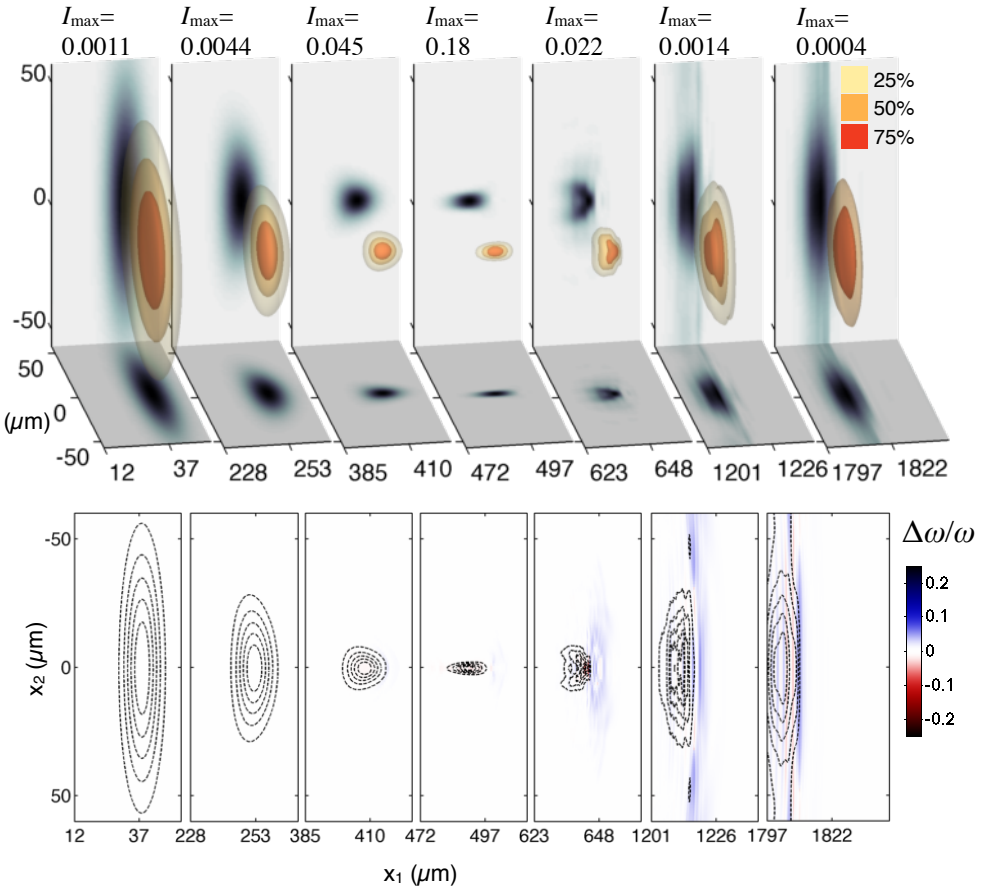

Figure 4.9 The peak of the gas density profile is at laser focus ($Z = 0$ mm). Top panel: isosurface plots showing the pulse dynamics at different propagating distances. Side panels display intensity profiles at cross-sectional planes through the center of the box. Bottom panel: spatial distribution of the local frequency shift $\Delta\omega/\omega_0$ of the laser pulse for the center slice. The blue color represents frequency upshift (blueshift) and red for frequency downshift (redshift). The dashed lines are 2D contour plots for the intensity profile.

For comparison, we plot in Fig. 4.9 the case in which the same density profile is peaked at the geometric focus. Since the laser intensity has become quite high when the pulse starts to interact with the gas, only a small part at the leading edge of the

pulse is involved in the ionization process. As a result, no significant blue-shifting takes place at the body of the pulse, which corroborates our experimental observation in Fig. 4.3 that minimum spectral broadening is found when the gas jet is centered near the geometrical focus. However, it should be noted that as the peak laser intensity approaches and exceeds relativistic intensities ($a_0 \sim 1$), excitation of plasma waves is possible, which can also give rise to pulse compression. A small amplitude plasma wave generated in our simulations for this particular case is manifested with a red-shifting portion of the pulse following the ionization blue-shifted pulse front (see Fig. 4.9 bottom panel: fifth figure from left). Nonlinear shaping from ionization is much weakened compared to Fig. 4.8. Although the laser has a larger peak intensity near the focal region because of the absence of pulse splitting and strong nonlinear shaping, it experiences less efficient longitudinal compression at the end of the simulation with a smaller peak intensity at equivalent propagation distances.

4.4 Conclusion and future work

In conclusion, we have demonstrated efficient self-compression of a multi-mJ laser pulse by ionization induced reshaping of laser pulses in a 100 μm scalelength continuously flowing gas target. This leads to very stable and reproducible compression down to 16 fs at 0.5 kHz repetition rate without a guiding structure. The high transmission means that the pulse peak power is doubled. The consequences are two-fold. Firstly, we have demonstrated a practical way to achieve significant pulse shortening. Secondly, the stability of the process indicates that plasma may be viable as a nonlinear optical medium to replace conventional optics in future high power laser systems.

In order to apply the self-compression effect to laser plasma experiments (for example, laser wakefield acceleration in the next chapter), the output laser beam must be re-collimated and then focused onto the plasma target. A deformable mirror may be necessary to control the wavefront of the re-collimated beam and correct for

distortions induced by the ionization compression process as well as by the additional optical components. It is likely to be a critical task to manage the dispersion and nonlinear effects when delivering a 15 fs high energy pulse. Another way to use the compressed pulse is to place the target directly at the beam focus. The compression dynamics occurs at the ionization gradient, which is in the mid-field region of a very intense laser pulse. As the laser pulse arrives at the focus, it already exits the plasma region. The effects of various f-numbers may be investigated in the future. Due to the difficulty to experimentally characterize the far-field at full power (note that the FROG measurement was performed in the near-field), we do not have any measurement of the temporal profile of the laser pulse at focus when it is self-compressed. Nevertheless the proposed method can be straightforwardly implemented to study pulse shaping effects on the interaction with the second gas target.

CHAPTER V

Laser Wakefield Acceleration of Electrons From Multi-milijoule Laser Pulses

5.1 Introduction

Most laser wakefield acceleration experiments have been limited to operation at a low repetition rate (much less than 10 Hz) due to the joule-level systems used, generating high-energy electrons in the 0.1–1 GeV range. A pulse energy less than 100 mJ was previously used to produce LWFA electrons in the range of several 10's of MeV [17], but a sub-10 fs pulse duration is required in order to access the nonlinear blowout regime. Acceleration using similar few-cycle optical pulses but with much less pulse energy (multi-millijoule level) has also been investigated through PIC simulations and sub-10 MeV electrons could be produced according to scaling laws and numerical studies [16, 20].

In this chapter, we investigate laser plasma wakefield acceleration using the λ^3 laser system with pulse energy at multi-millijoule levels and a pulse duration of 30 fs. Such amplified systems are widely accessible using standard CPA techniques and can operate at kHz repetition rates.

Both the amplitude and accelerating electric field of the plasma wave are proportional to the intensity of the driving laser pulse. To achieve wakefield excitation

using a laser system with peak power (0.3 TW) at least an order of magnitude smaller than that typically employed for LWFA, the laser pulse must be focused tightly to reach the required intensity ($a_0 \sim 1$) for large amplitude plasma wave generation. Short focal length geometries are generally not ideal for LWFA using high-power and high-pulse energy laser systems [93]. In our case, using tightly focused 30 fs laser pulses, the electrons can be accelerated in a sub-relativistic wave. Conditions for electron trapping in the plasma wave are also restrictive due to the lower achievable intensity. One method for trapping electrons is to use a density downramp injection mechanism [94], which was demonstrated experimentally using 10 TW lasers [95–97]. In this scheme, the inhomogenous plasma leads to a time varying plasma wave phase velocity, which enables trapping once the velocity of oscillating electrons exceeds the wave phase velocity.

As a result of acceleration in the slow plasma wave, electrons are measured to have energies in the range of 100 keV. Although having lower electron energies (sub-relativistic), this is the first experimental work demonstrating laser wakefield acceleration at high repetition rate and low pulse energy. In addition, electron bunches in this energy range are suitable for potential applications such as ultrafast electron diffraction. Finally, improved statistical studies and new diagnostic techniques are made possible by using a high repetition rate.

5.2 Experimental setup and procedures

The typical experimental setup is shown in Fig. 3.2. Since gas was constantly introduced into the chamber during the electron acceleration experiments with a limited pumping capacity, measured electrons appeared diffuse due to scattering when there was too much gas in the chamber. Experiments were carried out at a measured vacuum pressure of $p \leq 10^{-3}\,\mathrm{mbar}$. This level of vacuum may limit applications where surface contamination on samples must be prevented or high-voltage is required

such as use of a Thomson parabola ion spectrometer or a microchannel plate (MCP) detector and therefore a differential pumping system may be necessary.

After alignment of the parabolic mirror and the wavefront set using the deformable mirror (see Chapter VI for details), the gas jet was positioned roughly 200 μm below the laser axis centered at the focus. The focal position of the laser was determined by imaging a weak plasma spark generated in atmosphere air at attenuated power level. A silicon PIN diode was placed about 5 cm after the gas jet to detect the electron signal. The detector has a 7 mm^2 area and uses a 20 μm thick aluminum foil to block the laser light. The diode operates in biased mode and an oscilloscope monitors the signal of every pulse. To find the best experimental conditions, the position of the gas jet was scanned in 3D space to maximize the diode signal. The gas jet was moved at a step size of 10 μm. By visually observing the plasma emission light, the gas jet was first centered horizontally with laser axis to a 30 μm accuracy. Subsequent adjustments were mainly made to the longitudinal and vertical positions. The backing pressure was also scanned. The PIN diode was then removed to enable the electron beams to be measured on a scintillating screen.

Electrons were observed using a number of gases including helium, argon and hydrogen at plasma densities on the order of 10^{19} cm^{-3}. No electrons were detected when the pulse energy was reduced below 6 mJ.

5.3 Experimental results

5.3.1 Electron beam profile

Typical electron beam profiles at 32 cm downstream are shown in Fig. 5.1(a)-(c). The spatial distribution of the electron beam shows a "ring" structure around the laser central axis with a divergence angle about 50 mrad. By applying different deformable mirror configurations, thus changing the wavefront of laser beam, the electron beam

profile can be altered and the beam charge can be optimized. An improvement of more than a factor of 10 for the maximum signal count can be achieved by feeding the electron produced signal measured on the silicon PIN diode to the deformable mirror's genetic algorithm for optimization. We will discuss this further in chapter VI on using the electron image for the genetic algorithm with the deformable mirror adaptive optics.

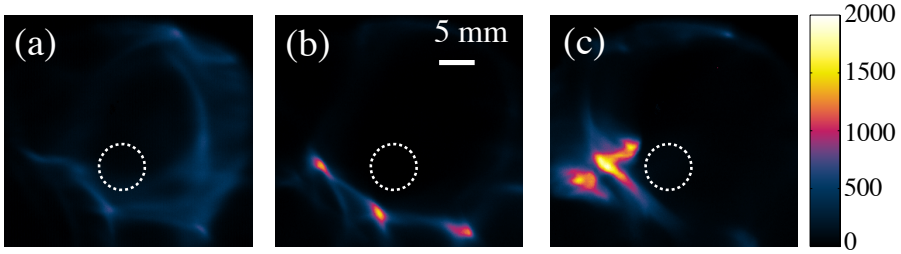

Figure 5.1 Typical measured electron beam profiles at 32 cm. The dotted circle indicates the position of the laser beam axis. The size of the circle represents a divergence angle of 20 mrad. Note the divergence of the laser beam is much larger. These three images were taken under the same experimental conditions except the deformable mirror is (a) off (a "flat" mirror); (b) optimized for best SHG generation and (c) optimized for best electron signal. The acquisition time are 1000 ms, 1000 ms, and 200 ms respectively for (a), (b) and (c).

The structure and pointing of the electron beam remains stable once the DM is set and the vacuum chamber has reached equilibrium state. The oscilloscope trace from the silicon diode showed less than 10% shot-to-shot fluctuation. In the experiments, data were obtained in "real time" for optimization of the beam parameters.

5.3.2 Energy distribution

The raw images of the dispersed electron signal are shown in Fig. 5.2(b) for FOS and Fig. 5.2(c) for IP. The two spectrum data are measured using different electron spectrometers and detectors under the same experimental conditions. After calibration using corresponding detector sensitivity, the deconvolved spectra agree with each other and exhibit a quasi-monoenergetic peak in the 100 keV energy range with

a width of $\Delta E_{\mathrm{FWHM}} \approx 20$ keV.

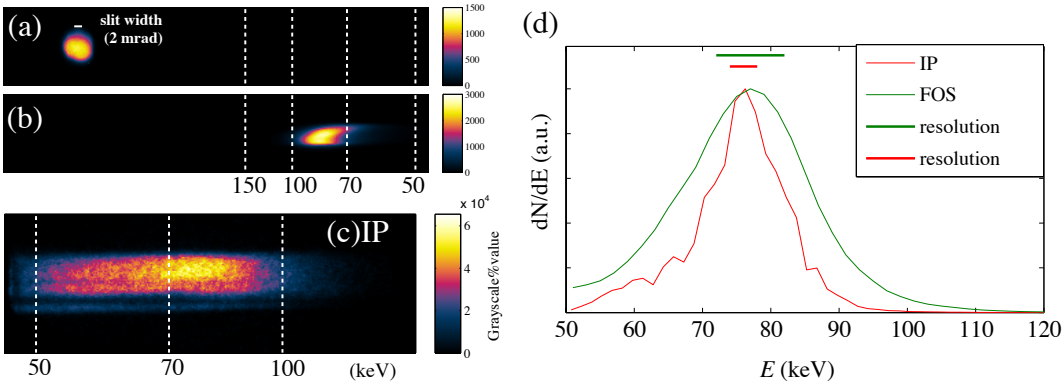

Figure 5.2 (a)(b): Typical spectral data obtained with FOS plate (from argon plasma) (a) without magnets (no slit; electron beam through the pinhole) (b) spectrally dispersed electron. (c) Raw spectrum data on image plate with the custom-built electron spectrometer under the same experimental conditions as in (b). (d) Calibrated electron spectra deconvolved from data in (b) and (c). Each horizontal bar represents the energy resolution due to the finite acceptance angle from the slit or the pinhole.

5.3.3 Density scan

At a fixed position, electrons were observed over a finite range of backing pressures corresponding to plasma densities of order 10^{19} cm^{-3}. The electron spectra are shown in Fig. 5.3(a) for an argon plasma at different backing pressures. A clear trend is observed such that the electron energy decreases as the plasma density increases. The signal significantly drops when the density is too low or too high. Note the difference in the exposure time for taking these spectral data.

Analysis results for the integrated electron signal and the energy peak as a function of the plasma density are plotted in Fig 5.3(b). At lower densities, the plasma wave phase velocity is so high that the oscillating electrons are below the trapping threshold. At plasma densities where the plasma wavelength, λ_p, in the wake is comparable to the laser pulse length L, large amplitude plasma waves are resonantly excited, enabling more efficient acceleration of injected electrons. At higher densities, the laser pulse

is likely to be susceptible to strong self-modulation or filamentation instability.

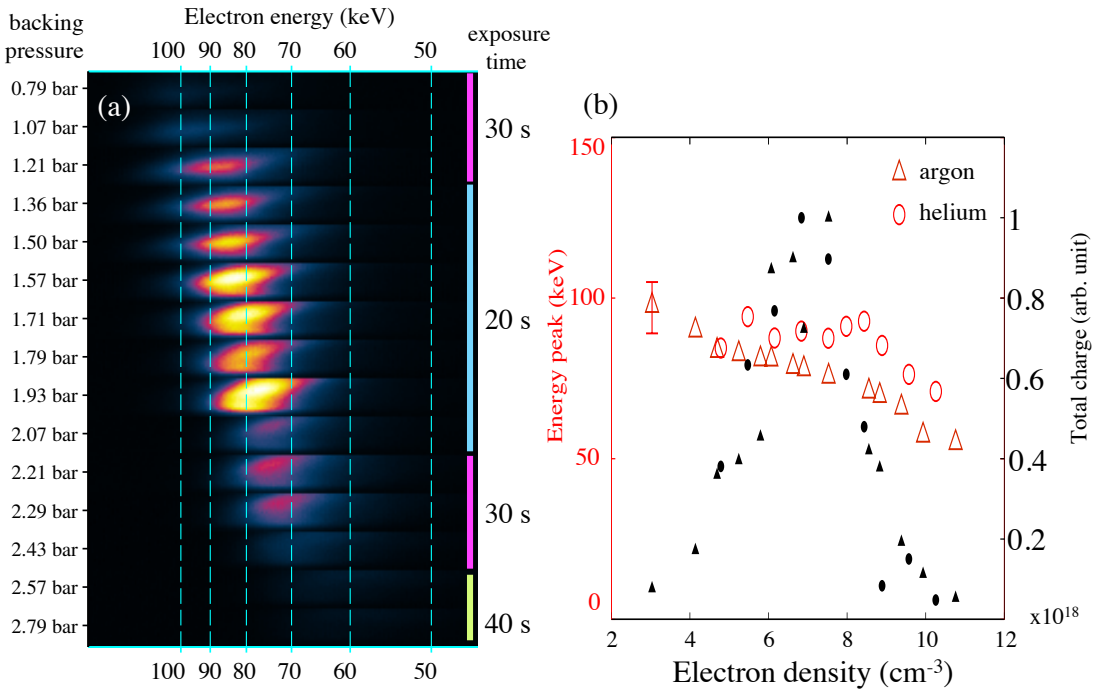

Figure 5.3 (a) Raw electron spectrum data shown as a function of backing pressure (electron density) using an argon plasma. (b) Electron charge and peak energy over a range of plasma densities. The peak energy is computed from the weighted average energy over a spectral width at 90% of the maximum. The error bar shows the energy resolution at 100 keV.

Quantitatively similar results obtained in the experiments using helium at comparable electron densities are also shown in Fig 5.3(b). This suggests that during our optimal experimental conditions, the ionization dynamics due to different gas species plays a less important role in the generation of the electron beams. We did not observe any detrimental effects such as plasma defocusing using higher Z gas target which have been observed previously in high-power laser wakefield experiments. This might be due to the fact that we have a very short Rayleigh length (on the order of 10 μm). Note this is different from the situation discussed in Chapter IV where the ionization of the gas occurs near the main body of the laser pulse, so it can drastically modify the spatiotemporal structure of the laser field and lead to self-compression.

5.3.4 Focal position scan

By scanning the gas jet position relative to the laser focus, we find that the electrons are preferentially accelerated when the laser is focused on the rear side of the gas plume. Figure 5.4 shows the integrated electron signal measured using a Lanex screen placed 6 cm downstream as function of the focus position. This is related to the acceleration mechanism based on density down ramp injection [94], which will be discussed in detail in the next section.

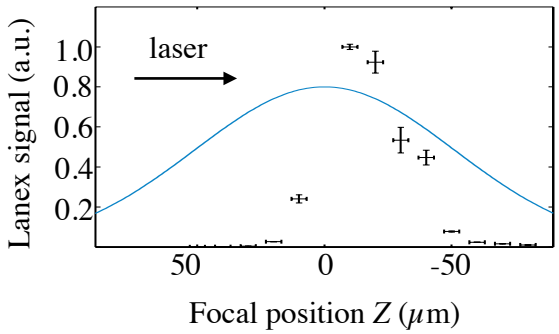

Figure 5.4 Integrated electron signal measured by Lanex scintillator screen (at 6 cm downstream) as a function of the focal position. A negative Z is defined for the laser focused on the rear side of the nozzle. The blue line is the shape of a Gaussian density profile with a FWHM of 120 μm.

5.4 Simulation & acceleration mechanism

To study the acceleration mechanisms, we performed both 2D and 3D PIC simulations using the OSIRIS 2.0 framework [71]. The 2D simulations ran in a stationary window of 713 μm $\times$ 38 μm, with a grid size of 18000 $\times$ 600 cells. A Gaussian profile of neutral helium gas was used with the peak centered at 200 μm [see the lineout in Fig. 5.5(b)]. The peak atomic density was $0.005n_c$. The peak width (FWHM) was 120 μm, as determined from the interferometric measurement. Electrons were produced using the ADK ionization model [37], with 4 particles-per-cell in each dimension (i.e., 16 total). The laser parameters were chosen to match our experiment and consisted

of a Gaussian spatial profile with a waist of $w_0 = 2\,\mu$m, and a 5th order polynomial temporal profile similar to a Gaussian with a pulse duration of $t_p = 32\,$fs. The laser pulse leading edge was initialized at $25\,\mu$m and focused at $210\,\mu$m. The simulation ran for 3 ps.

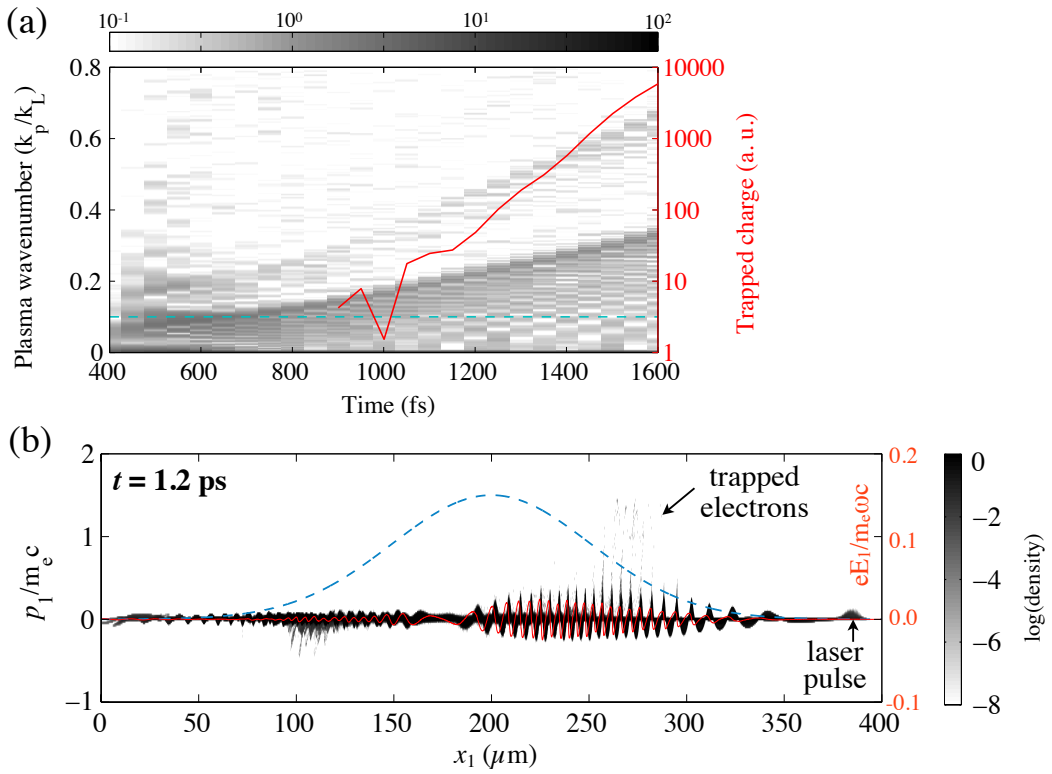

Figure 5.5 (a) The evolution of the plasma wavenumber spectrum from the 3D PIC simulation. Solid curve (red) is the total charge of the trapped electrons defined as those with $p_e/m_e c > 0.2$. (b) The electron momentum phase-space (x_1, p_1) at $t = 1.2\,$ps. The blue dashed curve is a lineout of the Gaussian density profile. The red solid curve is the normalized on-axis longitudinal electric field, E_1.

The short laser pulse generates large amplitude plasma waves by its ponderomotive force as it propagates through the center of the gas, but not to wave-breaking amplitude. Some time after the laser pulse leaves the plasma, wave-breaking of the plasma waves is observed and electrons are trapped and accelerated. The reason for this trapping is that the plasma waves formed on the downramp of the gaussian pro-

file have a time varying phase velocity, v_{ph}. In a 1D inhomogeneous plasma, the wave number k_p of a plasma wave varies in time according to $\partial k_p/\partial t = -\partial\omega_p/\partial x$ [98]. For an appropriately directed traveling wave on a decreasing density, k_p increases so that the phase velocity v_{ph} decreases as $v_{ph}/c = [1 + (\zeta/k_p)dk_p/dx]^{-1}$, where $-\zeta = ct - x$ is the distance behind the driver pulse. When the wave phase velocity falls below the maximum electron oscillation velocity in the wake, the charge sheets cross and trapping (wave-breaking) commences [94]. The phase velocity keeps decreasing as the distance behind the pulse becomes larger, so electron trapping in a gradual density inhomogeneity can occur several plasma periods behind the driver laser pulse [99].

The observed trapping mechanism from PIC simulations is illustrated in Fig. 5.5. The slowdown of the plasma wave phase velocity can be visualized by plotting the Fourier transform of the electron number density on the central axis as a function of time.

Qualitatively identical results are obtained in both 2D and 3D PIC simulations and Fig. 5.5(a) is plotted for the 3D simulation result. The peak electron density $n_e = 0.01n_c$ in this simulation translates to a relativistic plasma wave number $k_p = 0.1k_L$ for a linear plasma oscillation, where $k_L = 2\pi c/\lambda_L$ is the laser wave number in vacuum. In Fig. 5.5(b), we plot the electron phase space showing the injected electrons being accelerated from 2D PIC simulations. Note at this time the leading edge of the laser pulse has travelled to 392 μm. Electron trapping occurs about ten plasma waves behind the laser driver around 270 μm, where the phase velocity of the plasma waves in the simulation has slowed down to $0.35c$. This distinguishes the present work from previous experiments on higher power laser systems, where most electrons are trapped in the few plasma wave buckets just following the driver pulse (e.g. see Fig. 5A in [95]).

A quantitative comparison with the previous experiment using plasma density gradient injection by Geddes *et al.* [95] is given in table 5.1 for the other parameters.

The time evolution of the wakefield is the crucial reason for the electron trapping at low laser power.

Experiment parameter	Low power (this thesis)	High power (Geddes, *et al.*[95])
Laser pulse energy (mJ)	8	500
Laser pulse FWHM duration (fs)	32	47
Laser peak power (TW)	0.25	10
Laser repetition rate (Hz)	500	10
Focal spot FWHM (μm)	2.5	7.5
Electron kinetic energy (keV)	100	400
Absolute energy spread ΔE (keV)	20	140
Bunch charge	10 fC	0.3-1 nC
Averaged beam current	5 pA	3-10 nA
RMS shot-to-shot charge stability	$< 15\%$	40%
Plasma peak density (cm^{-3})	$0.5\text{-}2 \times 10^{19}$	$2.2 \pm 0.3 \times 10^{19}$
Plasma length FWHM (μm)	100–200	750±100

Table 5.1 A quantitative comparison between the present and previous work.

Using the cold, non-relativistic upper limit for the wave breaking in the one-dimensional approximation $E_{max} = m_e \omega_p v_{ph}/e$ [100] (cf. Eq. (2.17)), the calculated value is

$$eE_{max}/m_e\omega_L c \approx 0.022 \tag{5.1}$$

which is slightly larger than the simulated value 0.016 [see Fig. 5.5(b)]. The lower trapping threshold observed in our 2D PIC simulations might be due to the fact that the plasma has a finite temperature [101] or could also be due to multi-dimensional effects which can relax the trapping threshold [100]. Equivalent 1D PIC simulations we ran confirm that the 1D trapping condition agrees with the analytical expression very well.

A close-up view of the region where trapping occurs is shown in Fig. 5.6 from the 2D PIC simulation. At wave-breaking locations, the plasma wake phase front develops a backward curvature due to the radial dependence of the plasma wavelength for the wave evolution. Electrons are trapped along the curved wavefront as

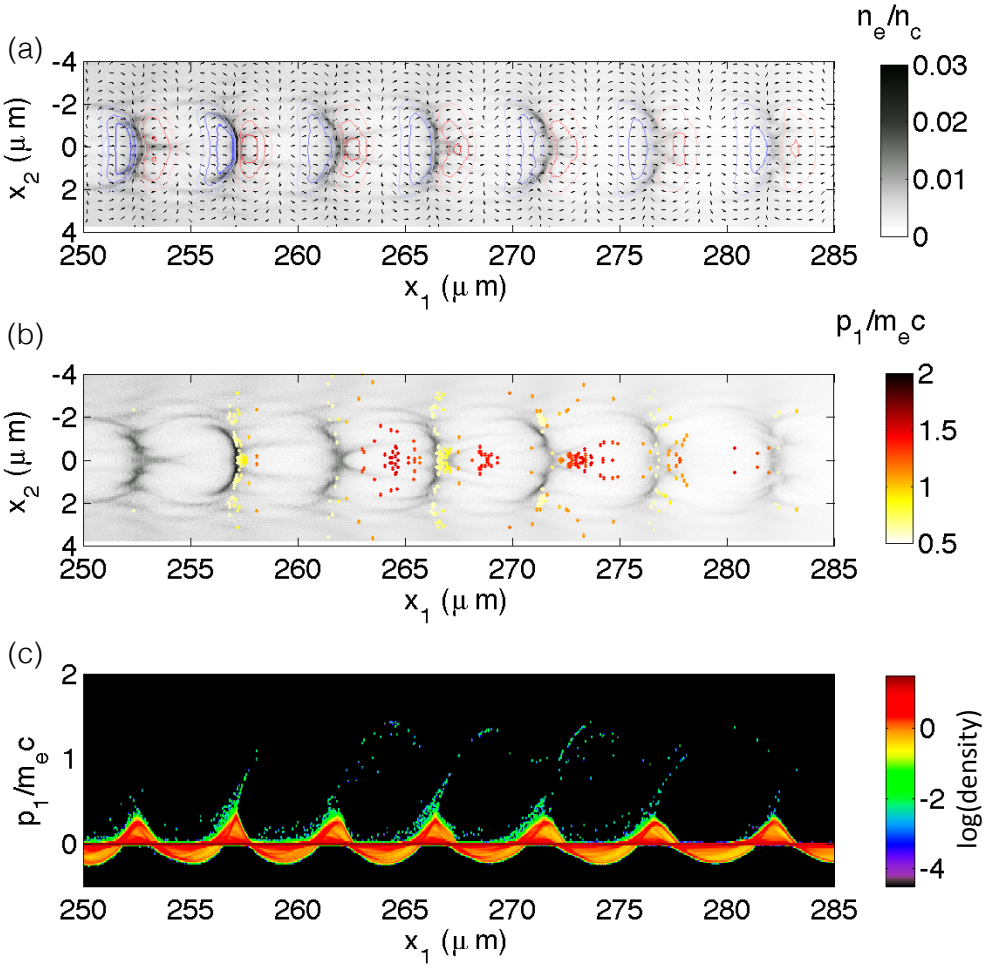

Figure 5.6 Results obtained from 2D PIC simulations at 1.2 ps at the trapping location (zoomed) of Fig 5.5(b) for: (a) Electron density and electric field in space x_1-x_2. Black arrows represent the electric field direction. The magnitude of longitudinal electric field E_1 is indicated by the isocontours, where the red (blue) colour corresponds to an accelerating (decelerating) field for electrons. (b) Spatial distribution of the accelerated electrons in x_1-x_2. Color represents the electron longitudinal momentum p_1. (c) Electron phase space (x_1, p_1).

shown in Fig. 5.6(b). This is different from what is normally observed in laser wake-field acceleration experiments where the electrons are trapped in the few wakes just following the driver laser pulse. In our scenario, the trapped electrons experience a defocusing electric field in the accelerating phase [see Fig. 5.6(a)] as these trapped electrons subsequently acquire a sub-relativistic net energy gain in the slow waves. The backward curvature of the plasma waves may therefore explain the "ring" shape

of the measured electron beam profile. A realistic focusing condition using the active deformable mirror is likely to break the radial symmetry and seed electron trapping such that the accelerated electrons are preferably distributed in a few stable beamlets as measured from the experiments [Fig. 5.1(b)].

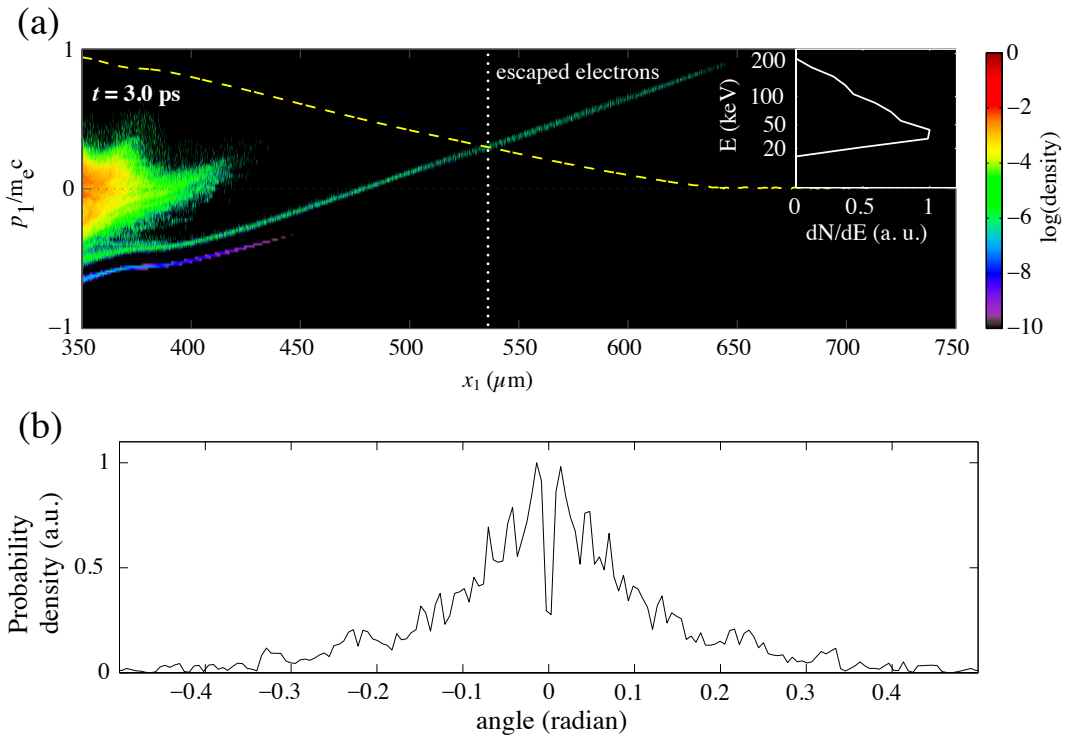

Figure 5.7 (a) The electron phase space (x_1, p_1) at $t = 3.0$ ps. The dashed curve is the plot of the additive inverse of the longitudinal electric potential expressed in $\mathrm{sgn}(\phi)\sqrt{(|\phi|/m_ec^2+1)^2-1}$. The energy distribution of the escaped electrons defined as those with $E + \phi > 0$ is shown in the inset. Note the color maps are in logarithmic scale. (b) Angular distribution of the escaped electrons in the simulation.

At later times, the longitudinal electric field established by the space charge separation pulls electrons with lower energies back to the plasma, but the portion of the trapped electrons having kinetic energies greater than the electric potential escape as shown in Fig. 5.7(a). It should be noted that the electrostatic field in 2D geometry may be overestimated compared to full 3D case because it is proportional to the inverse distance rather than the inverse distance squared. The angular distribution

of these electrons [Fig. 5.7(b)] exhibits a bimodal shape with a local minimum on axis, which resembles an observed "ring" structure with a divergence angle of ∼50 mrad [see Fig 5.1(a)]. As the accelerated electrons leave the simulation box, they ballistically expand such that its phase space distribution evolves into a linear form [Fig. 5.7(a)], indicating strong correlation between momentum and position. In principle, one can reverse this chirp to its uncorrelated original duration using techniques such as radio-frequency structures [102] or magnetic compression [103]. One possible path to further increase the electron energies is to add a second plasma segment as the accelerator stage, which is not a trivial task, as pointed out by Trines *et al.* [104]. An additional laser pulse may be required to drive a plasma wakefield in the second stage due to the rapid diffraction of the original laser pulse in a tightly focusing scheme. However, the increased complexity may bring the benefit of more flexibility on controlling the injector for the accelerator.

The maximum electron density at the maximum of the Gaussian profile was varied using n_e/n_c=0.005, 0.00725, 0.01 and 0.02 in the 2D simulations. The corresponding mean energies of the escaped electrons are 120, 100, 75 and 40 keV, which reproduces the observed experimental trend (Fig. 5.3). By scanning the focal position in the simulations, the maximum number of escaped electrons was generated when focusing between 40 μm and 60 μm behind the density peak on the rear side, qualitatively consistent with the experimental results.

5.5 Conclusion

In this chapter, we have used a high repetition rate 8 mJ, 30 fs laser to demonstrate plasma wakefield acceleration of electrons. Highly stable and reproducible electron beams with a quasi-monoenergetic spectrum in excess of 100 keV can be produced. The acceleration mechanism is investigated through numerical simulations, which suggest the electrons are trapped and accelerated to sub-relativistic energies in slow

plasma waves. With the capability of operation at 0.5 kHz and stability, "real-time" optimization and control of the electron beam properties is possible, for example using the deformable mirror adaptive optical system as discussed in the next chapter. In addition to demonstrating the scalability of wakefield acceleration to lower energies, such a source may be useful for ultrafast electron diffraction applications, provided that the longitudinal phase space can be time-reversed using ballistic compression.

CHAPTER VI

Adaptive Optics in Laser Plasma Experiments

6.1 Introduction

Adaptive Optics (AO) has been widely used in optical systems to correct wavefront distortions. Originally developed for astronomical telescopes [105] and satellite imaging, AO technology has found growing applications in a variety of fields such as microscopy [106], medical retinal imaging [107] and laser machining [108]. A type of phase manipulation instrument commonly used in adaptive optical systems is the deformable mirror (DM).

Deformable mirror adaptive optical systems have been successfully implemented in high intensity laser experiments to increase the peak laser intensity by improving the beam focusability, especially in systems using high numerical aperture optics. The shape of the deformable mirror can be determined in a closed loop where either a direct measurement of the wavefront is performed [109] or some nonlinear optical signal [110, 111] is used as feedback in an iterative algorithm. The objective of adaptive optics has largely been optimization of the laser focal shape to a near diffraction-limited spot, thus producing the highest possible intensity.

In this chapter, we will discuss the use of DM with adaptive feedback control throughout the laser plasma experiments described in this thesis, in particular, the optimization of the laser wakefield acceleration. The improvement to electron ac-

celeration as a result of wavefront optimization will play an indispensable part in developing applications using our electron source.

The organization of this chapter is as follows. In section 6.3, we compare three types of feedback control used for laser focus optimization, including one established technique [110]. Section 6.4 focuses on the direct optimization of electron acceleration and section 6.5 presents the result for pulse compression.

6.2 Adaptive optics with genetic algorithm

Traditional adaptive optics usually requires a measurement of the wavefront in order to determine the appropriate mirror shape to compensate the distortions. However, such a measurement can be difficult for a tightly focused beam. Also, it is not always known what is the best wavefront for a particular experimental process. A perfectly flat wave front is desirable for a diffraction-limited focusing but this is not necessarily the optimal condition for other physical processes. Therefore, we employ an evolutionary genetic algorithm (GA) is used to control the mirror shape of the DM. The computer optimization algorithm iteratively searches for the desired mirror shape by maximizing a feedback signal that correlates to the experimental goals. The idea of adaptive feedback control is simple yet very powerful in coherent control experiments where the light matter interaction is sensitive to the phase of the applied electric field in complex, real physical systems that are too sophisticated to model.

Genetic algorithm

The genetic algorithm is an adaptive learning method that is inspired by the process of biological evolution. It is a very useful optimization technique to solve global optimization problems in complex systems with a large number of variables. A typical GA requires a *genetic representation* of the solution parameter space and a *fitness function* to evaluate the solutions.

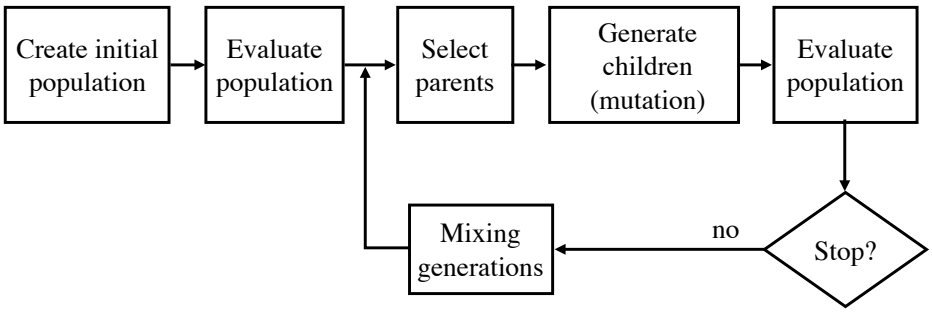

Figure 6.1 Flow chart of the genetic algorithm process.

Figure 6.1 shows the flow chart illustrating major steps in a genetic algorithm. It starts with a set of solutions (population) with randomly selected "genes". The fitness function is used to evaluate all individuals in the population. They are ranked from most to least fit individuals and the best ones are selected as the parents. The next step is to produce children using these parents by adding random mutations to the gene pool. The new solutions are evaluated and the best children are chosen as the new parents for the next generations. A portion of the parents from the previous generation are mixed and combined with the fittest children. This mixing will help retain some of the good genes if all the children generated are inferior than their parents and thus make the algorithm more efficient. The reproduction and evaluation cycle repeats itself until a termination criteria is satisfied.

A set of 37 values corresponding to the actuator voltage applied to the deformable mirror constitute the genetic representation of our system. The GA software is implemented using the LabView program. Based on the optimization goals, different fitness functions can be designed and constructed for evaluating the results in the following sections.

6.3 Optimization of laser focus

Focusing a laser beam using large numerical aperture geometry is very susceptible to aberrations introduced by alignment errors, thermal effects in the laser system and imperfections of the focusing optics. Correcting wavefront distortions for achieving diffraction limited focusing is crucial particularly in high intensity laser experiments where the highest peak intensity is desired. This section describes three different methods we have used for the fitness function in the genetic algorithm for optimization of the laser focus.

6.3.1 SHG in BBO

It was first demonstrated in Ref. [110] to use the second-harmonic signal generated from a beta barium borate (β-BBO) crystal to optimize the focal spot of the λ^3 system. The intensity of the second harmonic light is proportional to the square of the incoming radiation, $I(2\omega) \propto I^2(\omega)$. The intensity of the laser pulse is given roughly by $I \approx E/\tau w_0^2$, where E is the pulse energy, τ is the pulse duration and w_0 is the beam waist spot size. Therefore, a mirror shape that give a smaller spot size will generate stronger SHG signal. The experimental setup is shown in Fig. 6.2. A 60$\times$ microscope objective was used to image the focal spot on the BBO crystal. To avoid damage to the objective, the laser beam before the parabolic mirror was attenuated down to 0.1 μJ level by a half-wave plate polarizer combination and additional neutral density filters. Second-harmonic signal was measured using a photodiode covered by a set of colored Schott glass filters (BG39 and BG3) to block the fundamental laser wavelengths.

The SHG signal was amplified by a lock-in amplifier and sent to the genetic algorithm by a NI-DAQ device to be used as a figure of merit (FOM) for evaluating the fitness. Initial alignment of the parabolic mirror was done by monitoring the focal spot on a CCD camera with all the DM actuators set at 0 V. The GA was

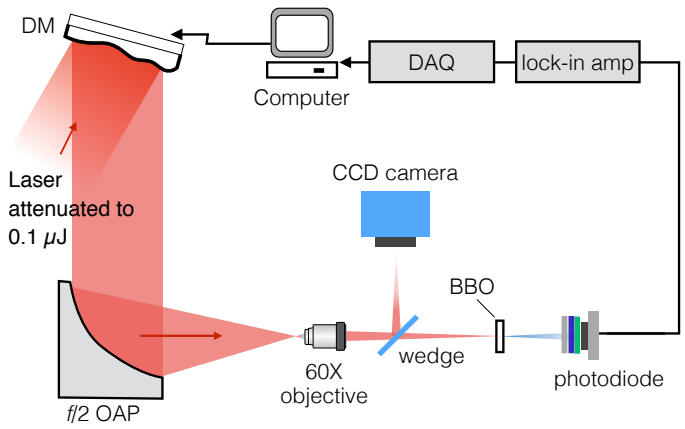

Figure 6.2 Experimental setup to optimize the laser focus using SHG from BBO. DM: deformable mirror; OAP: off-axis parabolic mirror; OL: objective lens.

developed in the LabView programing environment. After no more improvement could be made, we initialized the GA using a mirror figure with all actuators set at 30 V to allow bi-directional search because the range of the applied voltage in the experiments was 0 to 50 V. The program uses 10 best individuals for each generation to produce 100 children with a random mutation applied to the voltage values, which typically begins with a sufficiently large parameter space using a mutation level of 20% and is gradually reduced to as small as 1% as the algorithm reaches convergence.

6.3.2 Focal spot image

In this method, the image of the focal spot is directly used for the fitness function of the genetic algorithm. Since no BBO crystal is required, it is simpler to implement. The experimental setup is shown in Fig. 6.3.

LabView image tools allow us to grab image data from the CCD camera. The focal spot image must be processed and analyzed to give the figure of merit. A variety of schemes can be implemented to process the image to obtain the FOM. One fitness function for increasing the focal peak intensity is to assign a weighting factor that will contribute towards maximizing the peak count. The fitness function here is given

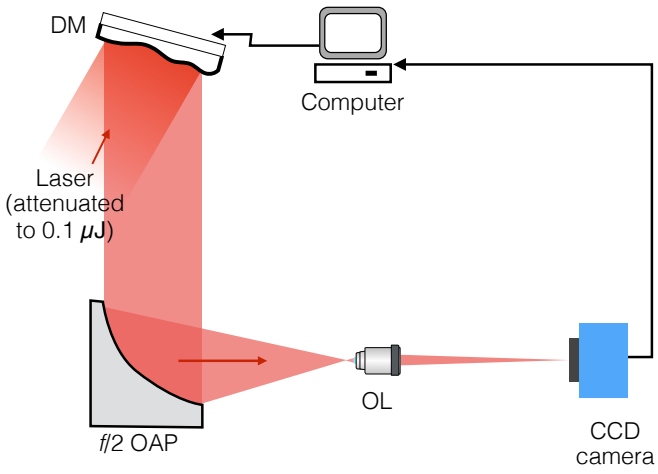

Figure 6.3 Experimental setup to optimize the laser focus using focal spot image. DM: deformable mirror; OAP: off-axis parabolic mirror; OL: objective lens.

by,

$$\mathrm{FOM} = \sum_{\substack{(i,j) \\ r_{ij} \neq r_0}} \frac{\mathrm{I_{ij}}}{|\mathrm{r_{ij}} - \mathrm{r_0}|^{\mathrm{n}}} \tag{6.1}$$

where I_{ij} is the pixel intensity for all pixel (i, j) from the whole image and r_0 is a point in the image used to specify the focal spot center. The power factor $n > 0$ gives higher weighting to those pixels closer to the target (inverse distance weighting).

6.3.3 SHG in helium

Both the previous two methods require the laser beam to be attenuated to a safe level to avoid damage to the objective lens. The neutral density filters used in the system may be a source of wavefront errors because actual experiments will be carried out using full energy of the laser pulse. The thermal effect of a high energy pulse may also modify the wavefront distortions.

An alternative optimization method without attenuation is to use second harmonic generation in a low pressure helium gas. The setup is shown in Fig. 6.4. A large-area (1 inch diameter) photodiode covered by a stack of filters is placed roughly 2 cm after

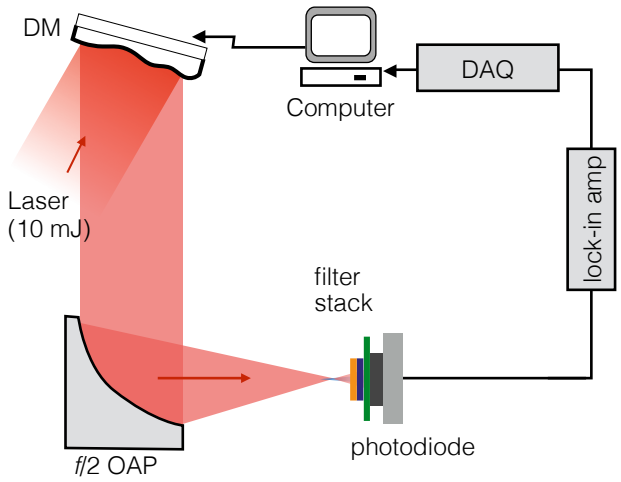

Figure 6.4 Experimental setup to optimize the laser focus using SHG in helium gas. DM: deformable mirror; OAP: off-axis parabolic mirror. The filter stack consists of a 800 nm high-reflector and two colored glass filters (BG3 and BG37).

the focus to collect all the diverging light rays. The photodiode detector is carefully shielded to prevent noise from stray light. The chamber is back filled with helium gas to an ambient pressure of 2 Torr.

The mechanism of SHG in neutral or partially ionized gas was first studied by Bethune in Ref. [112] and observed experimentally in [113]. The free-electron second-order susceptibility $\chi^{(2)}_{fe}(2\omega)$ can give rise to SHG polarization by the expression,

$$\mathbf{P}(2\omega) = \chi^{(2)}_{fe}(2\omega)\left[(\mathbf{E}\cdot\nabla)\mathbf{E} + \frac{i\omega}{c}\mathbf{E}\times\mathbf{B}\right] + \frac{e\mathbf{E}(\nabla\cdot\mathbf{E})}{8\pi m\omega^2} \tag{6.2}$$

where

$$\chi^{(2)}_{fe}(2\omega) = \frac{n_e e^3}{4m^2\omega^4} \tag{6.3}$$

We can rewrite Eq. (6.2) by using vector identities and Maxwell's equations for the first term, and quasi-neutral plasma condition $\nabla\cdot(\epsilon_p\mathbf{E}) = 0$ for the second term, where $\epsilon_p = 1 - \omega_p^2/\omega^2$ is the plasma dielectric constant,

$$\mathbf{P}(2\omega) = \chi^{(2)}_{fe}(2\omega)\left[\frac{1}{2}\nabla E^2 + \frac{2(\mathbf{E}\cdot\nabla\ln n_e)\mathbf{E}}{\epsilon_p}\right] \tag{6.4}$$

The first term of Eq. 6.4 has vanishing curl and thus does not radiate. For nonuniform plasma, the second term dominates the SHG due to the nonzero gradient of the electron density ∇n_e, which is produced by the ponderomotive force (Eq. (2.14)). When the chamber is back filled with helium the turbo pump is not used, therefore the contamination from higher Z gas atoms such as oxygen and nitrogen (air leak) can also be a contributing factor due to additional ionization near focus.

6.3.4 Results & Discussion

The optimization results are shown in Fig. 6.5(c)-(e) for the three described methods. For comparison, the focal spot profiles with the DM set for 0 V or 30 V on all actuators are also shown in Fig. 6.5(a) and (b). Ideally when all actuators shift from 0 V to 30 V, the mirror faceplate should translate without deformation. However due to interdependence and nonlinearity of the DM influence functions, we observed that applying 30 V on all actuators results in more wavefront distortion, as both the near- and far-field profiles of the laser beam showed more modulations. All three methods result in an improvement in peak focal intensity and less wings around the main spot. The final result from SHG in helium is slightly worse than the other two methods. This might be related to the details of the SHG mechanism as it not only depends on the focal intensity E^2 of the laser field but also the electron density profile of the plasma volume (Eq. (6.4)).

Figure 6.6 shows the improvement chart for the three methods. The algorithm reached convergence faster when using the image of the focal spot as the figure of merit, while the nonlinear optical methods have similar slope. A quantitative comparison is made in Table 6.1 for the three fitness functions used. The focal peak intensity is increased by more than a factor of 2 after the optimization, and about 66% of the laser energy is contained in the $1/e^2$ focal area. The measured spot size is about 2.5 μm FWHM.

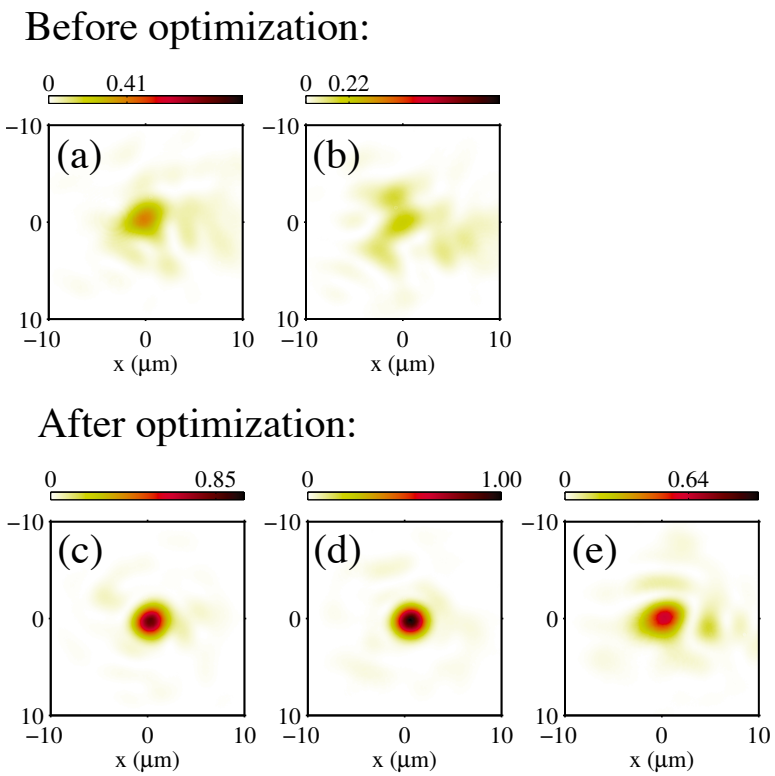

Figure 6.5 Far-field focal spot image with deformable mirror set for: all actuators at 0 V (a) and 30 V (b); optimization results using SHG from BBO (c), focal image (d) and SHG from helium (e). All the images are shown using the same color scale and the maximum intensity is marked on each colorbar normalized to that with the DM at 0 V.

	DM off (0 V)	SHG in BBO	focal image	SHG in helium
Peak intensity (arb. unit)	1	2.1	2.4	1.6
Δx_{FWHM} (μm)	3.0	2.5	2.4	2.8
Δy_{FWHM} (μm)	3.5	2.7	2.6	3.3
Energy contained in $1/e^2$	57.0%	65.6%	66.2%	60.0%
Energy contained in FWHM	26.8%	38.6%	39.1%	32.3%
Iterations required	-	∼40	∼10	∼40

Table 6.1 A quantitative comparison for spot optimization using different fitness functions.

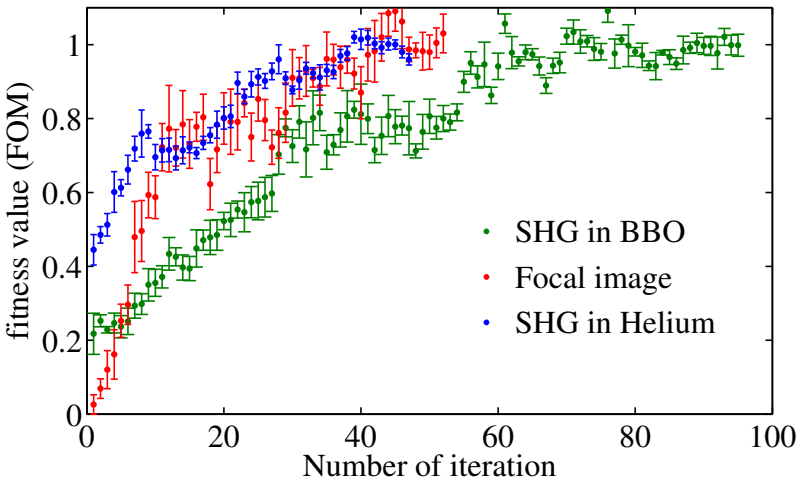

Figure 6.6 Improvement chart: the fitness value (figure of merit, FOM) as a function of iteration number. FOM is normalized to the maximum value for each method. Error bars represent the 10 best children from every generation (iteration).

6.4 Optimization of electron beams

In the previous section, we discussed experiments and methods to optimize the laser focal profile by using the deformable mirror to correct for wavefront distortions. However, for laser-plasma experiments where the plasma (ionized region) extends greater than the focal volume, not only the far-field will affect the experimental conditions, the mid-field can also be very important. Due to the complexity of the laser-plasma interaction, the precise optimal wavefront of the laser field may not simply correlate to having the highest peak intensity. Using the evolutionary search approach would be of significant advantage for such optimization tasks, where it is intractable to model the full experiment accurately. For example, adaptive pulse shaping has been successful to enhance and control the high-harmonic soft X-ray generation by either tailoring the phase in the temporal/frequency domain [114] or in the spatial domain (wavefront) [115], whereby the phase-matching condition of the driving laser pulse and the atomic system is optimized. Here, we employed this technique to control the dynamics of plasma and optimize the electron acceleration

described in Chapter V. We demonstrate that orders of magnitude improvement to electron beam properties can be made, through the use of genetic algorithm coupled to the DM adaptive optical system to coherently control the plasma wave formation.

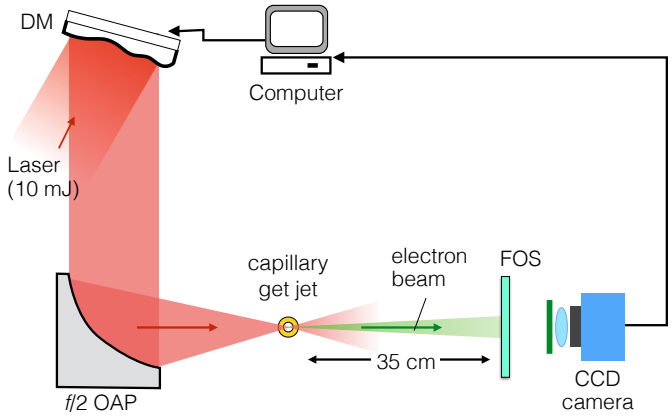

Figure 6.7 Experimental setup for direct optimization of the electron signal from the laser plasma accelerator. DM: deformable mirror; OAP: off-axis paraboloidal mirror, 50 mm diameter.

The experimental setup is shown schematically in Fig. 6.7. The electron image from the scintillator screen measured using the CCD camera is sent to the genetic algorithm for processing and use for the fitness function as feedback. This allows us to design the fitness criteria directly using the electron data. We will show that the improved electron result was not simply due to an improvement in focal quality, since a laser pulse with the "best" (highest intensity) focus in vacuum produced a greatly inferior electron beam compared with a laser pulse optimized using the electron beam properties themselves. The focal spot optimized for electron beam production had pronounced intensity "wings". Modifications to the phase front of the tightly focusing laser alter the light propagation, which experiences strong optical nonlinearities in the plasma, and therefore affect the plasma wave dynamics in a complex but deterministic manner.

Optimization of electron beam profiles

Eq. (6.1) was used to evaluate the fitness function from the electron scintillation data. The pixel of the optimization point r_0 can be *dynamically* adjusted during the genetic algorithm to concentrate all electron signal to the peak point of the charge distribution during each generation. The first generation of the genetic algorithm was initialized using a mirror shape with 30 V for all actuators.

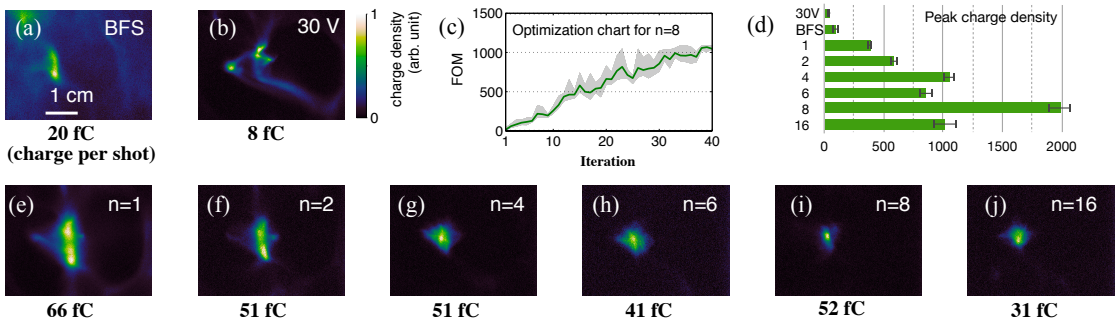

Figure 6.8 Electron beam profiles for a deformable mirror configuration of (a) the best focus spot (BFS) and (b) all actuators at 30 V; (c) shows the convergence of the genetic algorithm with n=8. The shaded gray area represents the range of the 10 best children in each iteration and the solid green curve is the average. (d) Comparison of the peak intensity; (e)-(j) Electron beam profiles after genetic algorithm optimization for different weighting parameters, n.

For comparison, electron beams produced by the "best" laser focus (by optimizing the intensity, e.g. having far-field profile in Fig. 6.5(c) and (d)) and the mirror shape at 30 V are shown in Figs. 6.8(a) and (b) respectively. The optimized electron beam profiles are shown in Figs. 6.8(e)-(j) for various weighting parameters, n. After the algorithm reached convergence, the best electron beam in terms of beam divergence and charge density was obtained using $n = 8$.

The peak charge density was increased by a factor of 20 compared to the initial electron beam profile before optimization [see Fig. 6.8(d)]. The optimized electron profile is highly stable and collimated, with FWHM of $\Delta x = 2.6 \pm 0.2$ mm and $\Delta y = 4.5 \pm 0.5$ mm. The shot-to-shot pointing (defined by the centroid position)

fluctuation of the electron beam is less than 1 mrad (root mean square, r.m.s.). The integrated charge was increased by more than two-fold from the electron beams generated by a laser focus of highest intensity. The high repetition rate and real-time diagnostics permit implementation of the algorithm within a practical time frame using a standard personal computer. Typical optimization takes only a few minutes (∼40 iterations) to reach convergence, as is shown in Fig. 6.8(c).

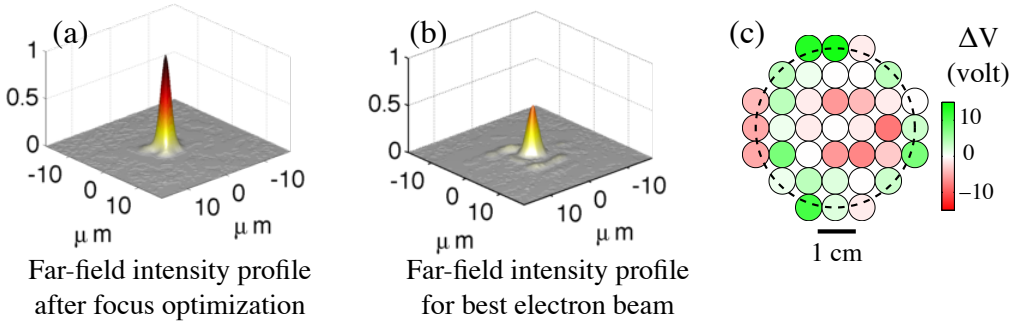

Figure 6.9 Comparison of laser focal spot with deformable mirror optimized for (a) second harmonic signal; (b) electron beam profile. (c) shows the difference in the voltage configurations for the deformable mirror actuators. The dashed line shows the mirror aperture.

In Fig. 6.9, we compare the focal spot (b) that produced the best electron beam with one that is optimized using SHG signal (a). The laser focal spot that produces best electron beam exhibits several low intensity side lobes around the central peak as depicted in Fig. 6.9(b). It has a very dramatic effect on the structure of the plasma waves produced and consequently the electron beam profile. Figure 6.9(c) shows the actuator arrangement displaying the difference in the applied voltage for the two deformable mirror configurations. To some extent, this can provide physical insight on the surface profile of an optimal wavefront for accelerating electron beams. Precise knowledge of the wavefront information requires a measurement using a wavefront sensor or a complete characterization of the DM actuator responses and its influence function, which was not done in the thesis work.

Control of energy distribution

We extended the genetic algorithm optimization to *control the electron energy distribution*. Through control of the light propagation, the plasma wave amplitude will be affected and therefore also the strength of the accelerating gradient. Hence, we can expect to be able to modify the energy spectrum.

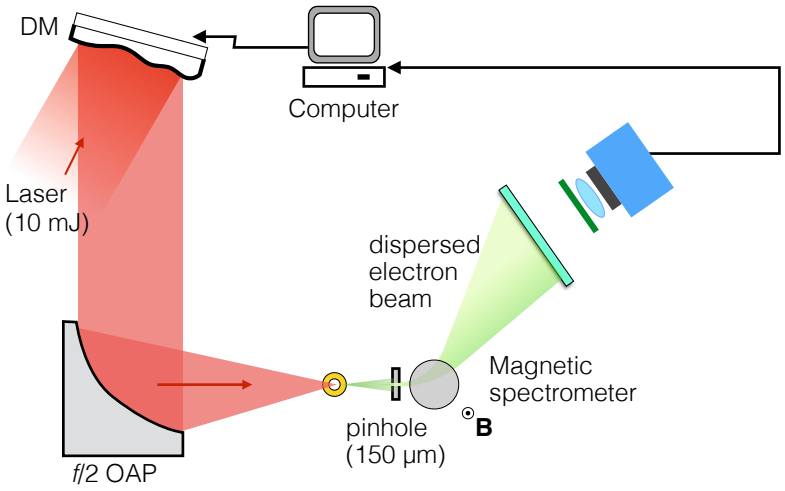

Figure 6.10 Schematic setup for control of electron energy distributiion

The schematic setup is shown in Fig. 6.10. A high resolution electron spectrometer was used to measure the electron energy distribution by magnetically dispersing the electrons in the horizontal plane. A 150 μm pinhole was placed 2.2 cm from the electron source to improve the energy resolution of the spectrometer. The energy resolution limited by the entrance pinhole and transverse emittance of the beam is estimated to be 2 keV for the energy range of measurement.

Three rectangular masks are set respectively in the low-, mid- and high-energy region on the dispersed data as shown in Fig. 6.11(a), (b) and (c). The fitness criteria is designed to preferentially maximize the total counts inside the mask. Here, using a pre-defined image mask, the FOM is calculated as follows,

$$\text{FOM} = \left[1 - \frac{I_{\text{mean}}(\text{outside mask})}{I_{\text{mean}}(\text{whole image})}\right] \times I_{\text{mean}}(\text{inside mask}) \tag{6.5}$$

where I_{mean} is the mean pixel intensity for a given image region.

The raw spectra after the genetic algorithm optimization are shown in Fig. 6.11: the brightest part has shifted accordingly. The resulting spectra have mean energies of 89 keV, 95 keV and 98 keV respectively for masks in (a), (b) and (c). Note that they do not fall on the visual centroid of the image because the scintillator sensitivity is not included in the presentation of the raw data, however it was taken into account for computing the mean energies. Our results show that manipulation of the electron energy distribution with the DM is somewhat restricted. The final result after optimization does not reach the objective mask completely despite that the mean energies can be varied by up to 10%.

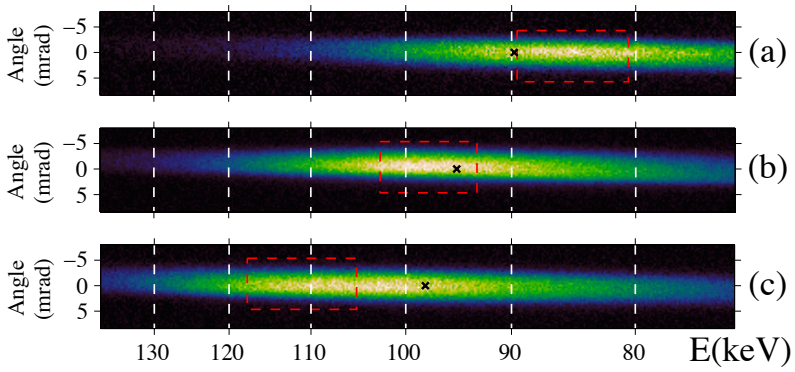

Figure 6.11 Control of electron energy distribution. Raw data showing the dispersed electron signal after genetic algorithm optimization using three different image masks. The location of the mask is indicated by the red rectangle and the black cross (×) represents the final mean energy for each spectrum.

Particle-in-cell simulations

To illustrate the underlying physics of plasma wave structures determined by the conditions of the driving laser pulse, we performed some 2D particle-in-cell (PIC) simulations. Parameters similar to the experiment conditions were used, with a Gaussian plasma density profile to enable trapping of electrons in the density down ramp. The simulations were carried out using the OSIRIS 2.0 [71] framework with similar configurations as that described in Sec. 5.4. Here a stationary box of the dimensions

573×102 μm with 10000×600 cells and 4×4 particles-per-cell was used. A pre-ionized plasma was initialized with a Gaussian density profile of 120 μm FWHM and a peak density of 0.01 n_c at 200 μm, where n_c is the plasma critical density. The laser pulse was initialized at the left edge of the simulation window with the focus located at 215 μm in the density down ramp. The simulations run for 3 ps.

It was shown in Ref. [116] from PIC simulations that the focusing fields of laser plasma accelerators can be controlled by tailoring the transverse intensity profile of the laser pulse using higher-order modes, where generalization to 3D was also discussed. Here for simplicity, we simulated a laser pulse with a fundamental Gaussian mode (TEM_{00}) or a superimposed mode of a Gaussian (TEM_{00}) plus a cross-polarized Hermite-Gaussian (TEM_{01}) pulse.

In 2D geometry, the transverse intensity profile of the laser pulse for the fundamental Gaussian mode has the form $a_0^2 \exp(-2x^2/w_0^2)$, and the first-order Hermite-Gaussian mode $a_1^2 \exp(-2x^2/w_1^2)(4x^2/w_1^2)$, where $a_{0,1}$ is the normalized vector potential and $w_{0,1}$ is the beam waist parameter at focus. To avoid beat interference, the two modes are orthogonally polarized, with parameters $a_0 = 0.9$, $a_1 = 0.3$, $w_0 = 3.31$ μm and $w_1 = 6.62$ μm. For the single mode simulation, $a_0 = 1.08$ and $w_0 = 3.31$ μm are used. In Fig. 6.12, we plot the transverse intensity profiles of the laser pulse from the 2D simulations at the beginning of the simulation ($x_1 = 19\,\mu$m, (a)) and after it has reached the focus ($x_1 = 215\,\mu$m, (b)).

Figure 6.13 shows the evolution of plasma wave structures at different times from the 2D PIC simulations. The electron density x_2-x_1 is plotted for the region where trapping occurs. The left column is for a driver pulse with a single Gaussian mode and right for a superimposed mode. Although the plasma wave has a larger amplitude when it is driven by a single mode laser pulse, the wake phase front evolves into a backward curvature when electrons are trapped and accelerated (for details see discussion in Sec. 5.4 from Chapter V, see Fig. 5.6). In constrast, the evolution of the

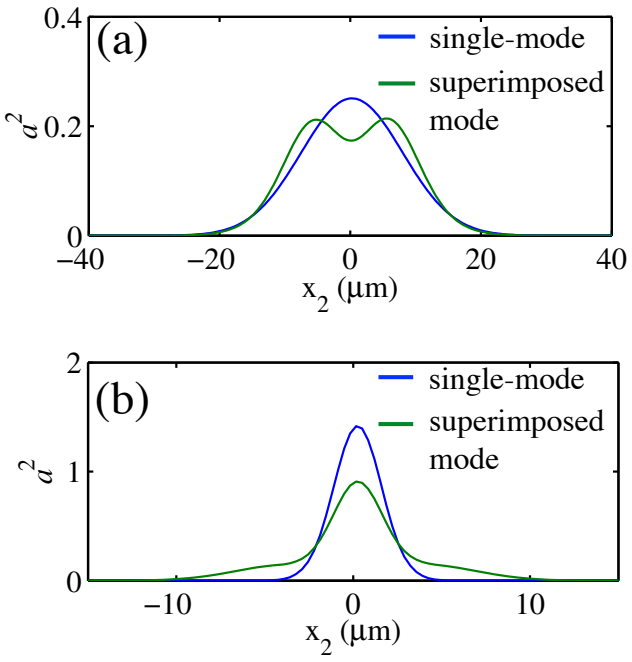

Figure 6.12 Transverse laser intensity profile at the beginning of the simulation (a) and at the geometrical focus (b) plotted for a single Gaussian mode (blue) and a superimposed mode (green) used in the 2D simulations.

wakefield driven by the laser pulse with additional mode forms a flatter phase front.

In Fig. 6.14, the momentum distribution of the forward accelerated electrons shows a larger transverse spread for the single mode laser pulse. This is a consequence of the different trapping conditions and acceleration fields from the coherent plasma wakefield structure, which is governed by the mode of the driver laser pulse.

In a comparative test, we ran the simulation using a single fundamental Gaussian mode laser pulse that has a slightly larger focal spot, thus giving the same focal peak intensity as the one with superimposed modes. The wakefield evolution shows very similar response as Fig. 6.13(a) and does not develop a flatter phase front as seen when using superimposed modes. Subsequently accelerated electrons have very similar divergence to that in Fig. 6.14(a), eliminating the possibility that the improvement comes from a high intensity effect or a simple change in f-number.

When a particular wavefront of laser light interacts with plasma, it can affect the plasma wave structure and trapping conditions of the electrons in a complex

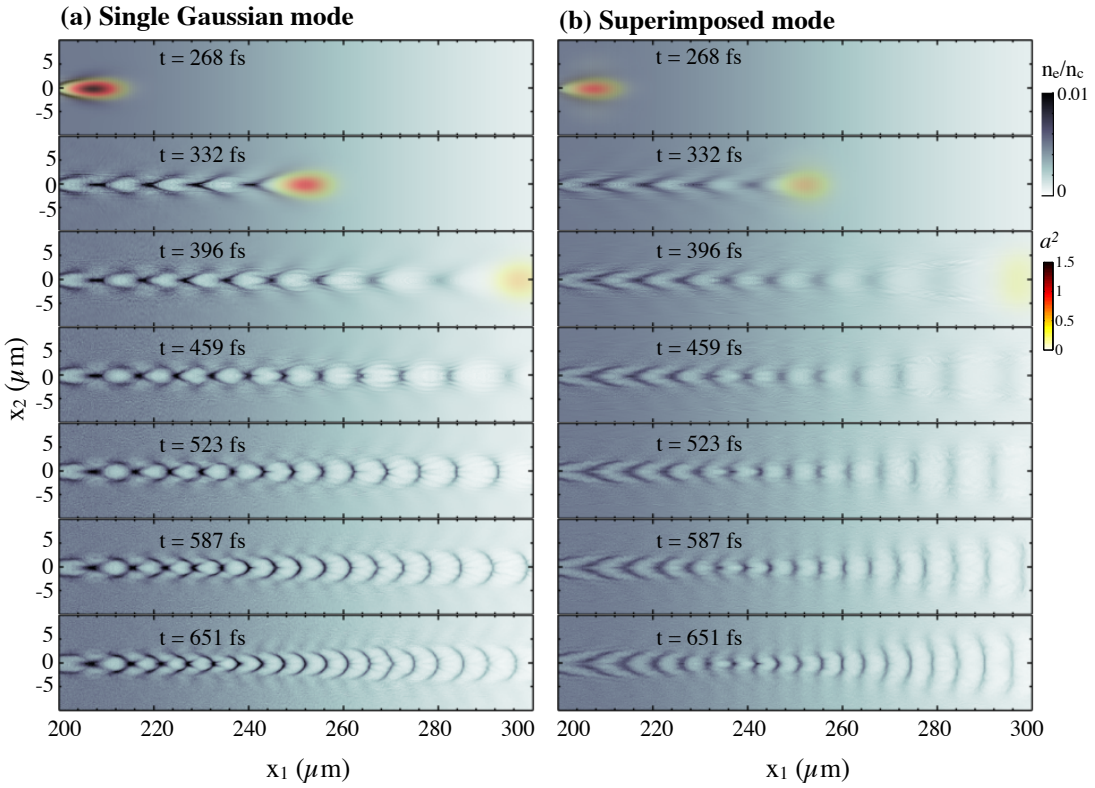

Figure 6.13 Simulation results: Snapshots of the plasma wave structures in the density down ramp region (x_1 = 200-300 μm) from a laser pulse with (a) single Gaussian mode and (b) superimposed mode, at different simulation times. Laser propagates to the right.

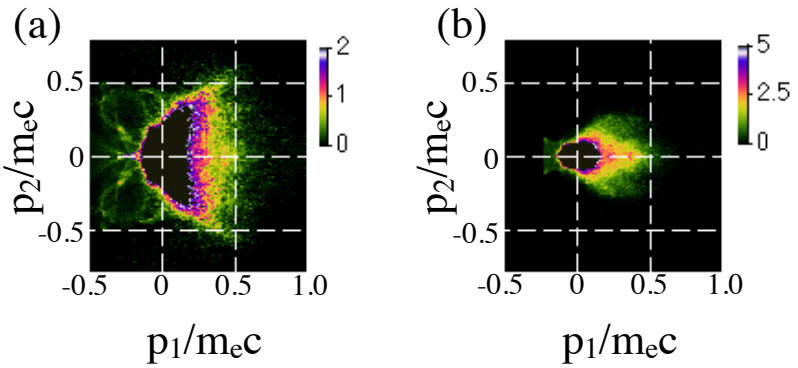

Figure 6.14 Simulation results: the phase space p_2-p_1 distribution of the accelerated electrons shown for (a) single mode and (b) superimposed mode at the end of the simulations (t = 2960 fs).

way. For example, Raman forward scattering, envelope self-modulation, relativistic self-focusing, and relativistic self-phase modulation [48] and many other nonlinear interactions modify both the pulse envelope and phase as the pulse propagates, in a way that cannot be easily predicted and that subsequently dictates the formation of plasma waves. Ideally, the light interacts in such a way as to generate large amplitude plasma waves with electric field structures that accelerate electrons with small divergence, high charge etc. Because of the complicated interaction, it is difficult to determine *a priori* a laser phase profile that will lead to such a plasma structure. However, such unforeseeable conditions were successfully revealed by *using the evolutionary genetic algorithm method*, with the result that the electron charge can be increased and emitted in a very well collimated beam.

6.5 Optimization of pulse compression

In this section, we apply the wavefront shaping optimization to the pulse compression experiments described in Chapter IV. With no changes to the pulse measurement setup, we program the measured pulse duration (τ_{FWHM}) from the commercial FROG device to use with the genetic algorithm, with a very simple fitness function FOM $\propto 1/\tau_{\mathrm{FWHM}}$. The feedback loop is illustrated in Fig. 6.15.

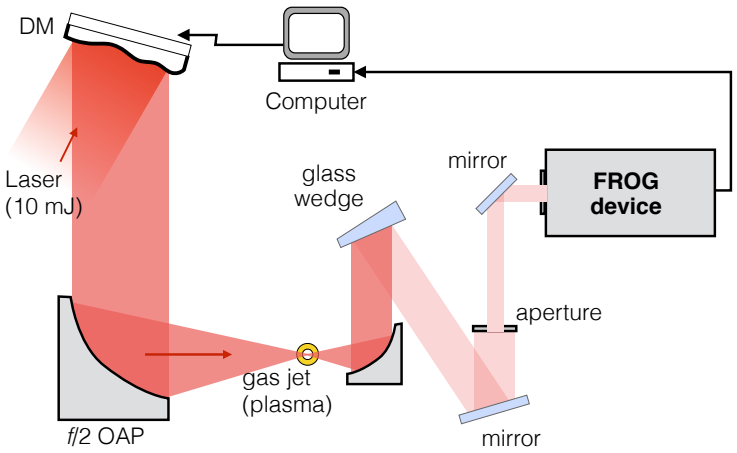

Figure 6.15 Schematic setup for pulse compression optimization.

Figure 6.16 shows the output pulse duration as a function of iteration during the GA optimization. Argon gas was used with a backing pressure of 3.4 bar. The self-compressed pulse duration was further reduced from 30 fs to 25 fs by adaptively shaping the wavefront. The original pulse duration was 36 fs for this measurement.

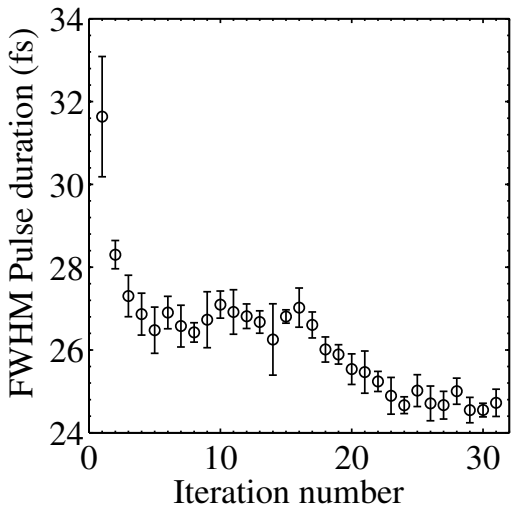

Figure 6.16 Pulse compression optimization results using the deformable mirror with genetic algorithm.

6.6 Conclusion

The concept of adaptive coherent control of plasma wave dynamics opens new possibilities for future laser-based accelerators. Although still at the stage of fundamental research, laser wakefield accelerators are showing significant promise. Such improvements could be integrated into next generation high-power laser projects, such as ICAN [32], based on the combination of many independent fibers, taking advantage of both their high repetition rate and controllability.

In laser wakefield acceleration experiments, the stability and response of the wakefield to laser conditions, such as phase front errors, is not well understood, but is crucial for the success of the laser plasma accelerator as a source of relativistic electrons.

Implementing the methods of this study should enable a significantly improved understanding of the wakefield acceleration process with regard to stability, dark current reduction and control of beam emittance, for example.

One limitation of the experiments discussed in this chapter for wavefront shaping was the number of actuators and maximum deformation of the deformable mirror used. In addition, this work was performed using adaptive optics, but it is clear that coherent control of plasma waves should be possible in a variety of configurations, for example by using an acousto-optic modulator to control the temporal phase of the driving laser pulse.

Adaptive wavefront control in our configuration has led to the production of electron beams with smaller divergence and higher charge. In the next chapter, we will discuss applications of the LWFA electrons, which have greatly benefited from these improvements.

CHAPTER VII

Ultrafast Probing Using Laser Wakefield Accelerated Electrons

7.1 Introduction

Ultrafast electron diffraction (UED) is a powerful technique for investigating structural dynamics in matter [117, 118]. For example, the dynamics of the melting transition has been elucidated on the sub-500 fs time scale in metals [119] or semi-metals [120]; structural phase transitions have also been studied in more complex materials, such as VO_2 [121] or the charge density wave (CDW) material 1T-TaS_2 [122]. State of the art of non-relativistic electron sources for ultrafast electron diffraction consist of electron bunches generated from photocathodes and subsequently accelerated in static fields, typically providing $50 - 300$ keV kinetic energy. The shortest electron bunches produced in this way are in the $300 - 500$ fs range, with thousands of electrons per bunch [118]. These limitations are essentially due to two factors: (i) the space charge of the beam, which limits the number of electrons and the temporal resolution, (ii) the ballistic propagation of electrons with various velocities, which produces a linear chirp in the electron bunch and also tends to degrade the temporal resolution. The second issue has recently been solved by using a RF cavity in order to change the sign of the chirp and compress the electron bunch down to 80 fs

[123, 124]. Concerning the first issue, current developments tend to promote the use of RF guns in order to accelerate electrons to MeV energies in higher electric fields for mitigating the effect of space charge [1, 125–127]. In addition to larger accelerating gradients, the RF fields can also be used to compress the electron bunches and very short bunch durations are predicted [128]. However, it should be noted that the use of RF technology tends to introduce jitter in pump-probe experiments and can thus limit the temporal resolution, in particular when accumulation over several shots is required [129]. Space charge effects can be ultimately eliminated if the number of electrons are reduced to the single-electron limit [130, 131].

Another approach consists of using electrons produced in laser-plasma interaction experiments. In such interactions, plasma electrons are accelerated by laser and/or plasma fields and can gain MeV energies in micron scale distances, thus mitigating the effect of space charge. At the source, the electron bunch duration can be shorter than the laser pulse duration, e.g. < 30 femtoseconds. In addition, the electron bunch is produced directly by the laser pulse in a jitter free manner which can potentially help in improving the temporal resolution in UED experiments. However, electron bunches from laser-plasma interactions have relatively large energy spread distributions; bunches produced from laser-solid interaction typically have $\Delta E/E$ of tens of percent or more [69] whereas bunches from underdense plasmas can have $\Delta E/E$ of a few percent or more [10, 12, 132]. Consequently, the electron bunch develops a linear chirp as it propagates which can severely degrade the bunch duration for sub-relativistic or moderately relativistic beams as used in UED experiments. For UED performed in scanning mode, electron bunches from plasmas must be manipulated to invert the linear chirp using longitudinal compression methods, for example, an alpha magnet [103] such that the electrons are re-bunched at the sample location.

Tokita *et al.* [133] recently performed high-intensity laser-solid interaction experiments, demonstrating that electrons originating from the back of a solid target can be

used to obtain single shot and high quality diffraction images. A temporal resolution of 500 fs was obtained after magnetic pulse compensation [134] so that the temporal resolution might be the intrinsic bunch duration given by the sheath acceleration mechanism: electrons recirculation in the target might elongate the bunch duration.

In contrast, electrons generated from a laser wakefield accelerator can intrinsically provide shorter bunch durations in the 1–10 fs range [135]. Such short durations can be explained by the acceleration mechanism: electrons are injected in a plasma wave bucket typically having a duration $< \lambda_p/2c$, where λ_p is the plasma wavelength. Relativistic electron bunches in the 0.1–1 GeV range are produced with Joule level laser systems operating at 10 Hz or below and their energy is too high for practical applications in UED. The electron source we have discussed in the previous chapter has strong potential for UED experiments: (i) after removing the linear chirp, the bunches should be sub-100 fs, (ii) electron bunches are intrinsically synchronized to the laser source, (iii) the gas target and the high repetition rate permit ease of use as well as the possibility to accumulate data.

In this chapter, proof-of-principle experiments using our electron source for ultrafast probing will be described. In section 7.2, we show that by focusing the electrons using a solenoid, the transverse coherence of this source is sufficient to provide well contrasted static diffraction images. In section 7.3, we conduct a time resolved experiment to study a non-equilibrium plasma produced by optical field ionization. Finally we present some preliminary results from our attempt to a pump-probe study of laser-induced thermal effects on a single-crystalline thin foil gold sample.

7.2 Electron diffraction experiment

Figure 7.1 shows a schematic drawing of the experimental setup. A custom-designed solenoid magnet lens was used to control the divergence of the electron beams. The electrons produced in the interaction were first filtered by an aperture

of 0.5 mm diameter before they traveled through the solenoid lens. The temporal distortion induced by the magnetic lens due to the rotational motion of electrons in the solenoid around the axial direction or misalignment of the magnetic lens was found to be on the order of a femtosecond [136, 137]. The residual pressure in the vacuum chamber stays below 10^{-3} mbar which permits operation of the electron source at 0.5 kHz. The electron charge and beam profile was optimized using the deformable mirror, which is detailed in Chapter VI.

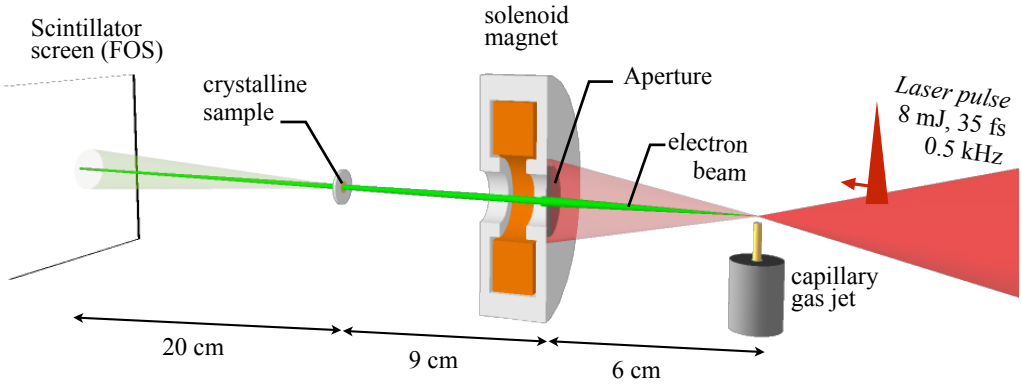

Figure 7.1 Experimental setup for electron diffraction. The solenoid is placed 6 cm after the electron source, the distance between the sample and the scintillator (FOS) is 20 cm.

Figure 7.2(a) shows a typical DM optimized electron beam profile projected onto the scintillator. Fig. 7.2(b) shows the beam after filtering by the 0.5 mm pinhole. The beam divergence can be reduced to less than a mrad by the magnetic lens, as shown in Fig. 7.2(c). The electron beam at best focus can be well fitted by a Lorentzian function, which comes from the fact that the beam is polychromatic; the lower energies form a halo around the focused beam.

7.2.1 Chromaticity of solenoid magnet and diffraction pattern

A solenoid magnetic lens is a common device for focusing and transport charged particle beams. Using the thin lens approximation, the formula of the solenoid focal

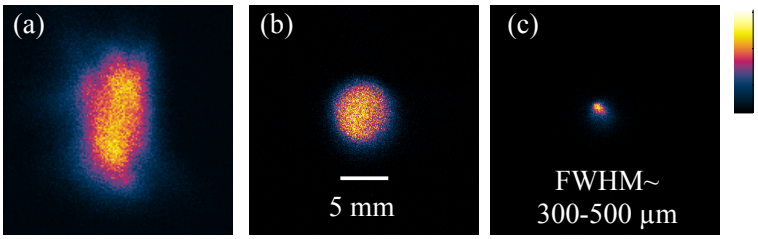

Figure 7.2 Unfocused electron beam (a) with no aperture; (b) through 0.5 mm pinhole and (c) focused electron beam.

length f is given by [138] for electrons:

$$\frac{1}{f} = \left(\frac{e}{2m_e c\beta\gamma}\right)^2 \int B_z^2 dz \tag{7.1}$$

The focusing power of the coil depends on the magnetic flux density as well as the momentum of the charged particles. Therefore, the chromaticity of the magnetic lens permits performance of some shaping of the energy distribution. The axial magnetic field B_z can be varied by driving the solenoid at different current levels. Energy selection is depicted in Fig. 7.3 showing a series of electron spectra measured using the magnetic spectrometer described in Sec. 5.3.2. Electrons of higher energies are focused when the solenoid current is increased from 0.8 A to 1.4 A.

We found that the solenoid alignment was extremely sensitive, in particular because the electron beam had such a large energy distribution, a spatial chirp could be present at focus if the solenoid was not perfectly aligned on the electron beam axis. This would cause an asymmetric smearing of the diffraction pattern as observed in [139].

The effect of solenoid alignment was verified by measuring the electron energy spectrum at different spatial positions across the beam. This was done by moving the magnetic spectrometer so that different portions of the beam could enter through the 0.5 mm slit. The slit was about 7 cm before the screen (cf. the setup of the

magnetic spectrometer in Fig. 3.2). The slit was moved approximately at a step size of 0.1 mm. Fig. 7.4 shows the measured electron energy distribution along the focus at two different solenoid alignment conditions. A strong spatial chirp is clearly seen in Fig. 7.4(a) whereas the focused electrons have a more symmetric energy distribution

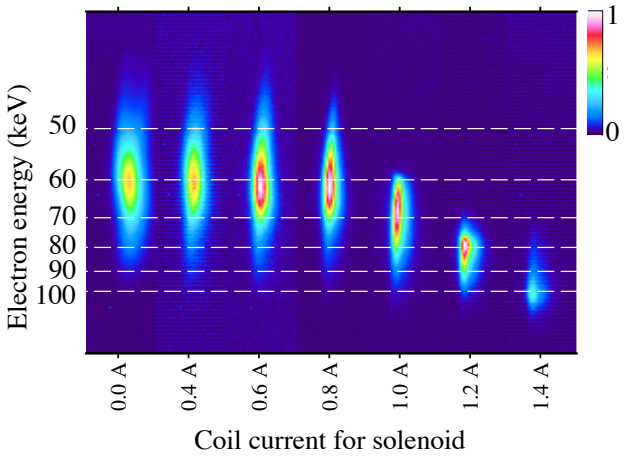

Figure 7.3 Experimental electron energy spectrum as a function of solenoid current. The intensity scale is normalized to the maximum value for each spectrum.

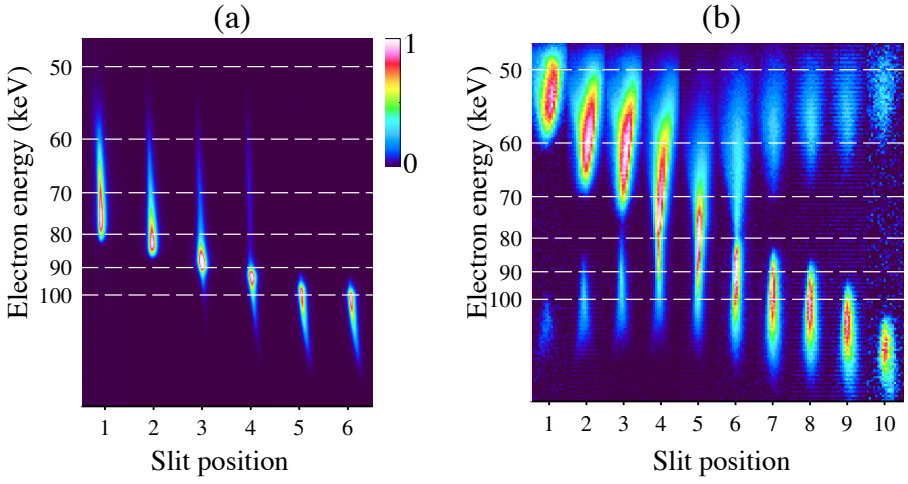

Figure 7.4 Electron energy distribution measured across the focused beam with solenoid alignment for (a) a spatial chirp is present at focus (b) a symmetric focus. The intensity scale is normalized to the maximum value for each spectrum.

in Fig. 7.4(b). Note that energy spectra in Fig. 7.4(b) have slightly lower energies with a broader energy spectrum because this data set was acquired on a different experimental day, which results in broadening of the diffraction rings. In Fig. 7.4(a), the distribution peak at 93 keV for slit position 4 has an energy spread $\Delta E = 7\,\mathrm{keV}$.

Diffraction patterns were recorded for these two different alignment conditions with electrons focused at the scintillator screen. Debye-Scherrer ring patterns obtained using a 10 nm thick polycrystalline aluminum sample are shown in Fig. 7.5. The Al foil was free standing on an mesh as used in transmission electron microscopy. In Fig. 7.5(a), one can clearly see the rings from the (111) and (220) planes; the rings originating from diffraction on the (200) and (311) planes are also visible although dimmer. When the solenoid is well aligned, the beam focal spot is symmetric, indicating that no spatial chirp is present and the diffraction pattern is symmetric as shown in Fig. 7.5(b).

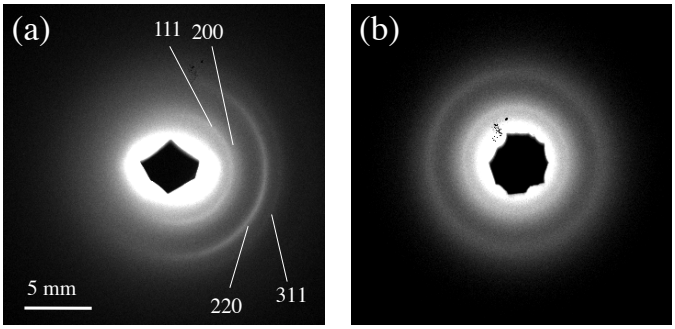

Figure 7.5 Electron diffraction patterns from a 10 nm thick polycrystalline Al foil. (a) and (b) correspond to the conditions in Figs. 7.4(a) and (b) respectively.

We also obtained diffraction patterns using a single crystalline gold foil sample, Fig. 7.6. The diffraction spots (Bragg peaks) are streaked in the radial direction due to the energy spread in the focused beam. The solenoid lens was well aligned in this case as is indicated by the radially symmetric patterns.

Both images in Fig. 7.5 were obtained by accumulating data over tens of seconds.

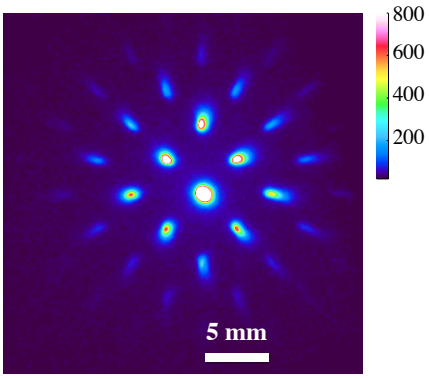

Figure 7.6 Electron diffraction pattern obtained from a single crystal gold sample, using 5000 electron shots (10 s exposure time on a 12-bit CCD camera).

Diffraction rings could be measured by accumulating 200 shots or more. In Ref. [133], single shot diffraction patterns have been recorded from a single gold crystal with $\sim 10^5$ electrons per bunch. The electron source described here has a similar charge per shot. Having replaced the CCD camera with a more sensitive camera (an electron-multiplying CCD, EMCCD, Andor Luca-R), we could obtain a single shot image of gold diffraction pattern as shown in Fig. 7.7(a).

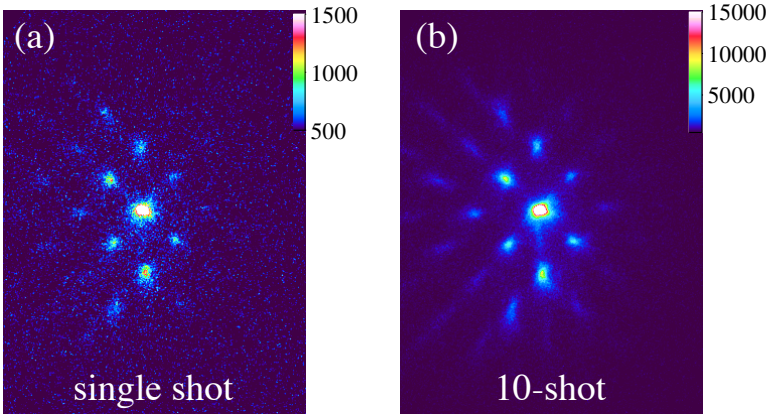

Figure 7.7 Single-crystal Au diffraction patterns obtained on a 14-bit EMCCD for (a) single-shot and (b) 10-shot.

For both cameras, a standard zoom lens was used to image the scintillator plate on the CCD or EMCCD camera. Given the magnification of the imaging system with an effective aperture of 25 mm (measured), we calculate the solid angle to be 7×10^{-3} sr

for collecting scintillating photons. More than one order of magnitude improvement can be expected, for example, by using a fiber optic taper to couple the FOS to the detector. This would further improve the effective quantum efficiency (QE) of the imaging system to allow even higher signal-to-noise ratio (SNR) for single-shot data acquisition. Such an electron source can be potentially used for studying irreversible ultrafast dynamics, provided that the bunch has been longitudinally compressed at the sample.

7.2.2 Beam emittance

The bunch propagation in the beam line was modeled using the general particle tracer (GPT) code [140]. We found that the experimental beam profile could be reproduced by using an initial transverse gaussian distribution with a rms radius of 15 μm: the result is shown as the blue curve in Fig. 7.8(c). In addition, the calculated energy distribution in the focused beam agrees well with the experiment. From the GPT calculation, it was possible to retrieve upper values of the normalized emittance in the focused beam (integrated around 2σ RMS): $\epsilon_N = 0.02$ mm·mrad. The transverse coherence is then given by $L = \hbar D/mc\epsilon_N \approx 5\,\mathrm{nm}$, a value suitable for performing electron diffraction.

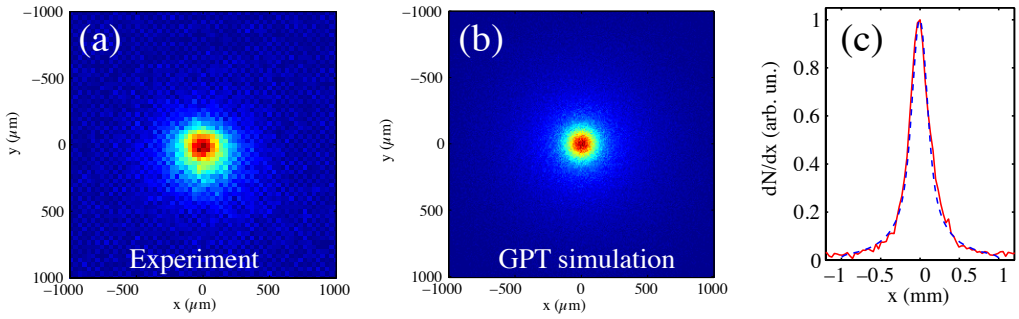

Figure 7.8 (a) Measured focused electron beam profile. (b) GPT simulated electron profile. (c) Horizontal lineout of the beam profile (red solid curve) and GPT simulation results (blue dashed curve).

7.2.3 Stability

For UED experiments where the intensity and position of Bragg peaks need to be monitored with high accuracy, it is of crucial importance to characterize the stability of the electron source. Using the calibrated scintillator, we found that the beam charge is up to 8×10^4 electrons/bunch (12 fC/bunch), with 14% fluctuations RMS shot to shot, which can be reduced to 7.9% when the images are averaged over 10 shots. The shape of the energy distribution does not fluctuate very much. Finally, the pointing stability of the focused beam is found to be greater than the angular resolution of the imaging system, i.e. 400 μrad. The parameters of the electron beam are found to be superior to many of those reported in the literature on laser wakefield acceleration [132, 141]. This may be due to the fact that a kHz laser system is usually more compact and stable than a multi-joule laser system. In addition, the injection mechanism that is used in this experiment relies on downramp injection (see section 5.4 in Chapter V) and it does not involve nonlinear evolution of the laser pulse which tends to be detrimental for obtaining a stable electron beam.

For reducing the bunch duration to the sub-100 fs range, future research will focus on designing a magnetic compressor for compensating the longitudinal chirp or increasing the electron energy to the MeV level [20] in order to decrease the effect of ballistic stretching.

7.3 Time resolved experiment

Although these sub-relativistic electrons accelerated in a laser plasma accelerator can have an uncorrelated bunch duration on the order of several plasma wavelengths (sub-100 fs), they are quickly elongated longitudinally during propagation because of the nature of their sub-relativistic speed and non-zero energy spread. For example, the bunch duration of 90 keV electrons having an energy spread of $\Delta E/E = 20\%$

will increase at a rate of 5.5 ps per cm propagation from the source. However, since the long bunch is intrinsically correlated with its longitudinal position, this can be utilized as an advantage in streaking mode whereby different temporal components are spatially separated. This allows for recording temporal evolution of the dynamics in a single run. If the detection efficiency is sufficiently high, this technique can be used for single-shot visualization of irreversible processes in ultrafast electron diffraction. The temporal resolution The temporal resolution is determined by the streaking strength and the uncorrelated duration rather than the electron bunch duration at the sample.

For multi-shot exposure, the stability of the probe clearly becomes a significant problem. Both shot-to-shot charge fluctuations and pointing fluctuations will cause smearing of the temporal feature and reduction in the signal-to-noise ratio. Although the pointing stability was improved by the solenoid lens and the aperture, the use of a small aperture slightly increased the shot-to-shot charge fluctuation compared to the whole electron beam because of the small variations in the spatial profiles. Therefore, in order to obtain statistically meaningful information, we need to average very many shots. In our experiments, we automated the data acquisition by using an electro-mechanical optical shutter that was triggered to "open" or "close" at $\sim$2.5 Hz. For each "open" or "close" state of the shutter, a "pumped" image and an "unpumped" image were recorded respectively, each containing 100 shots (0.2 ms exposure). This procedure provides a reference shot and also helps eliminate possible systemic drifting on longer timescales.

7.3.1 Probing non-equilibrium plasmas using streaked electrons

The streaked electron probe was first applied to study the evolving electric field from a laser produced plasma. The experimental setup is shown in Fig. 7.9.

In this pump-probe setup, the pump is an optical pulse containing up to 300 μJ energy split from the main laser; and the probe is the LWFA electrons. The pump

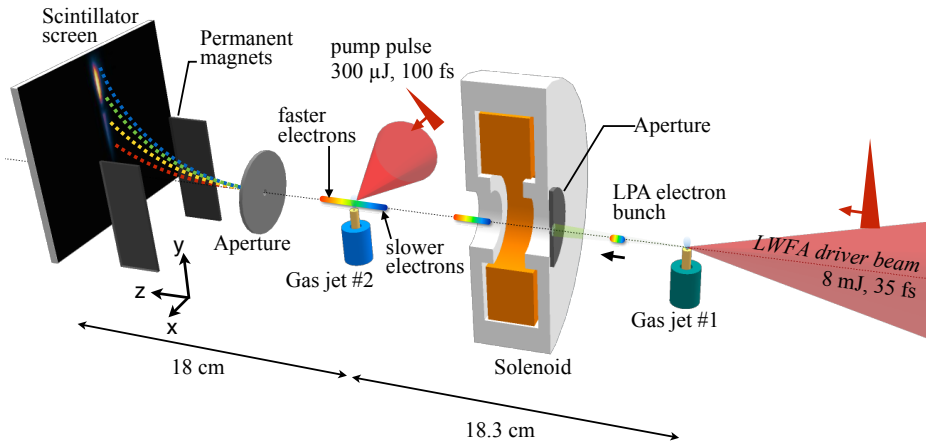

Figure 7.9 Setup for time-resolved pump probe experiments using streaked electrons.

pulse was focused by an $f/1$ off-axis parabolic mirror onto gas jet #2 (see Fig. 7.9), yielding a maximum peak intensity up to 10^{17} W/cm^2. The pulse energy can be continuously varied from 0-300 μJ using a half-wave plate and polarizer combination. The pump beam is delayed by a variable delay stage such that the arrival time of the electron bunches can be adjusted relative to the formation of the plasma. Electrons with energies of 70-110 keV were produced in gas jet #1 (see Chapter V for details). A solenoid magnetic lens with a 0.5 mm entrance aperture was used to collimate the electron beam. Electrons were detected on a scintillator screen imaged by a lens coupled electron-multiplying CCD camera (Andor Luca-R, 14-bit). After passing through the plasma, the electron bunch entered a magnetic spectrometer through a 100 μm aperture. The spectrometer provides the streaking mechanism due to the different paths the electrons travel in the magnetic field. Electron trajectories in three-dimensional magnetic field were calculated using the particle tracing module of the commercial software COMSOL multiphysics [68].

Figure 7.10(a) shows the characteristics of the electron probe, in the absence of the pump laser beam. The unstreaked beam profile is displayed on the top left, which is the undispersed electron signal when the permanent magnets are removed,

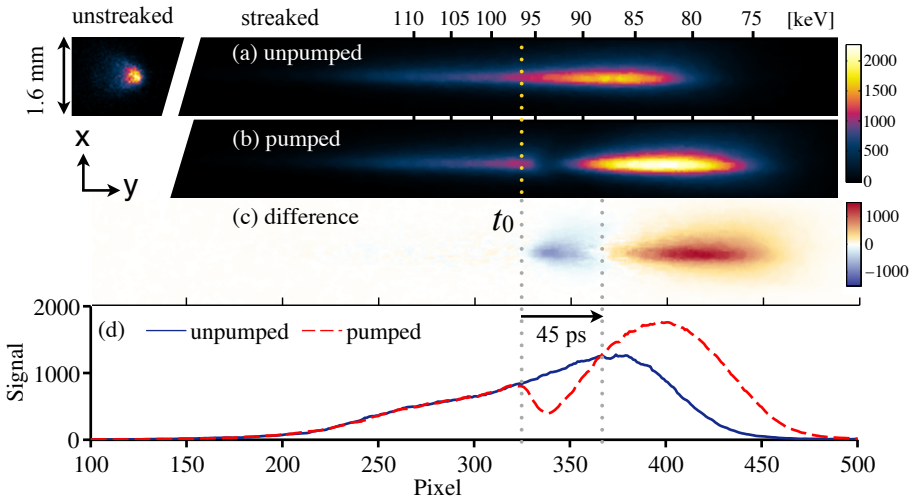

Figure 7.10 Averaged streaked electron signal for 100 electron pulses (a) unpumped (b) pumped and (c) differential signal. (d) Lineout along streaking axis y at the center.

with a beam size of 350 μm (FWHM). This transverse emittance dictates the energy resolution in the dispersed streak signal, which determines the achievable temporal resolution. A resolution of 2 keV is found at 90 keV, which corresponds to a time window of 10 ps at the plasma location for our geometry.

The pump laser pulse was delayed such that the formation of plasma (time zero t_0) occurs when the long electron probe passes the gas target about half way to allow for better signal-to-noise ratio. The time interval between pulses (2 ms for 0.5 kHz) is much greater than the plasma recombination time scale, which enables data accumulation over many cycles.

Figure 7.10(b) displays a typical streaked electron image when pumped. The electrons are deflected by the plasma electric field. The effect of plasma field evolution on the probe electrons can be characterized by two stages. Initially a strong radially outward electric field is quickly established to over-focus electrons, resulting in a dip in the streaked beam pattern; the magnitude of this field strength is gradually reduced on a time scale of 10 ps, focusing more electrons towards the beam axis so that they can enter the streaking region and produce a higher signal. The deflection of the

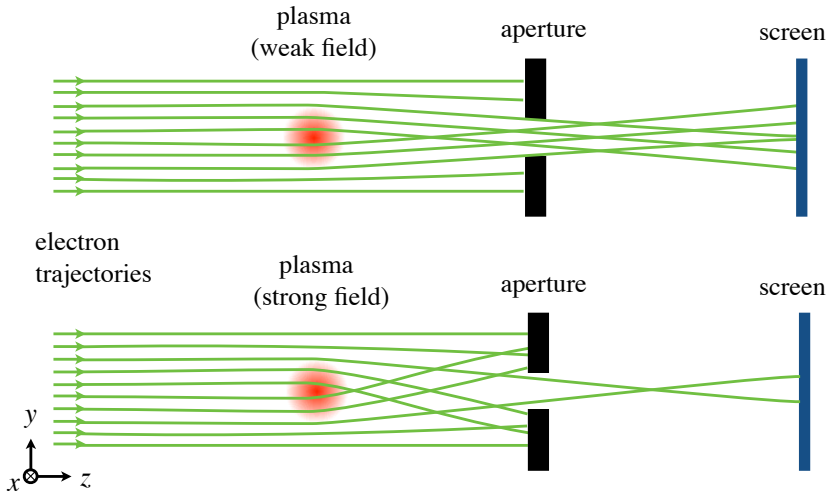

Figure 7.11 Schematic illustrating electrons deflected by the weak and strong electric field of the plasma, without the presence of the streaking magnetic field. Plasma volume is shown at the focus with a cylindrical symmetry and the pump laser beam (OFI beam) propagates along the x axis.

electrons is illustrated in Fig. 7.11 for both weak- and strong-field cases without the streaking magnetic field. With the magnetic streaking applied, the width of the dip feature can be translated to the time axis. The dynamics can be clearly seen in the difference signal image in Fig. 7.10(c) by the positive and negative signal regions. The crossing point is marked in Fig. 7.10(d), which corresponds to $t = 45$ ps. The depth of the dip depends on the strength of the plasma electric field, which can be related to the associated plasma temperature.

Generation of electric fields in a laser produced plasma can be understood using the generalized Ohm's law of a plasma. The expression for the electric field can be derived by considering the electron fluid momentum equation,

$$n_e m_e \frac{d\mathbf{v}_e}{dt} = -en_e(\mathbf{E} + \mathbf{v}_e \times \mathbf{B}) - \nabla \cdot \overline{\overline{P_e}} \tag{7.2}$$

For an unmagnetized plasma (neglect the magnetic term) and consider the time-scale of quasistatic approximation (set left-hand-side to zero), we can obtain the electric

field,

$$\mathbf{E} = -\frac{\nabla \cdot \overline{\overline{P_e}}}{en_e} \tag{7.3}$$

The pressure tensor gradient $\nabla \cdot \overline{\overline{P_e}}$ can be reduced to $k_B T_e \nabla n_e$ for an ideal, isothermal electron gas with a temperature T_e. However, a laser produced plasma can have a very non-Maxwellian distribution of electron energy due to the ionization heating effect [142–144], through which a small fraction of electrons ionized near the peak of the laser pulse can pick up energies associated with the ponderomotive potential. This mechanism may be responsible for the initial large electric fields observed in our experiments when a sufficiently intense pump laser interacts with a high-Z gas (argon). An order-of-magnitude estimate for the lower limit of this electric field can be obtained using the small angle approximation, $\tan\theta \approx e\int E(r)dr/W$, where θ is the deflection angle of the probe electrons, $E(r)$ is the radial plasma electric field and W is the incident electron kinetic energy. For our geometric configuration, we have $\theta \approx d/2D$, where $d \approx 0.5\,\mathrm{mm}$ is the electron beam size and $D = 13\,\mathrm{cm}$ is the distance from the plasma to the aperture. The scale length of the cylindrically symmetric plasma volume can be estimated to be 10 μm. Plugging in these numbers with the electron energy of $W = 95\,\mathrm{keV}$, we have $E \sim 10^7\,\mathrm{V/m}$.

Pump intensity dependence By changing the pump beam energy, we can vary the intensity of the optical field for the plasma generation. The electron temperature of the plasma is expected to change due to the varying ponderomotive potential of the laser. A decrease in the signal magnitude is observed in the subtracted image data, Fig. 7.12. Here, every streak image is an average of 16 pairs (pumped and unpumped, each 100 shots). The noise is manifested on the part of the streak corresponding to $t < t_0$, i. e. before the pump beam arrives.

Measurement of the longitudinal phase-space A composite image is made in Fig. 7.13 using the central part of pumped streak data images by scanning the delay time of the pump laser pulse at a 2 ps step. This gives a direct visualization of

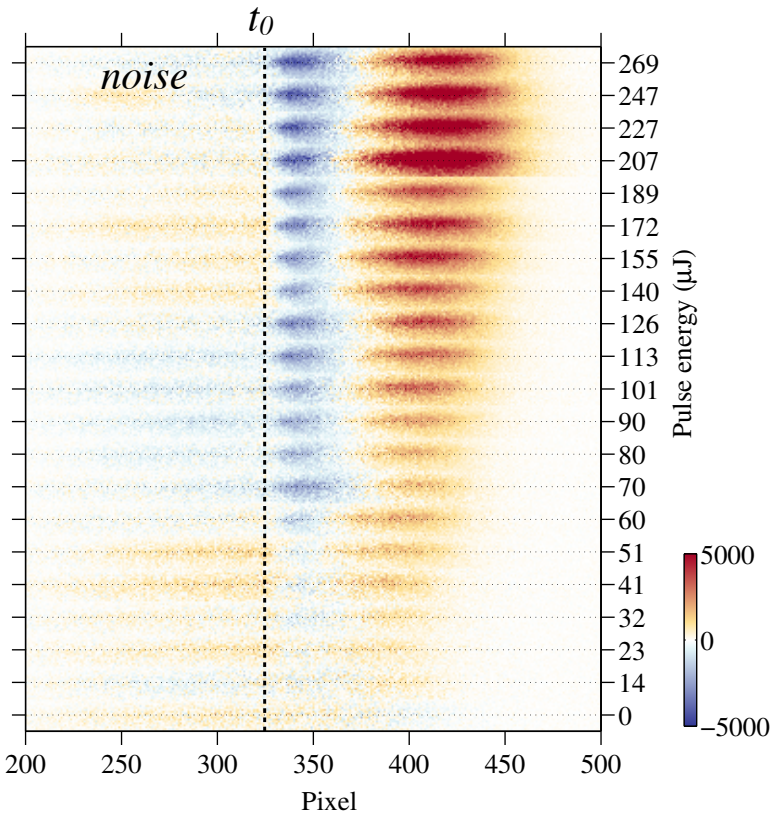

Figure 7.12 Subtracted image of pumped and unpumped vs pump energy (pump intensity).

the longitudinal phase-space distribution of the electron probe. A distinctive, almost linear slope is found, which indicates the strong correlation between momentum and the temporal position. This measurement also provides an absolute calibration on the streak timing.

Future work will include detail analysis of the electron trajectories in the presence of a time-varying self-generated plasma electric field. Numerical methods exist such as Vlasov-Fokker-Planck codes [145, 146] to model a collisional plasma so that the ways in which plasma conditions such as electron temperature and initial density profile will affect the evolution of plasma fields can be elucidated. We will then be able to compare these results with the experiments to give quantitative information on the plasma properties.

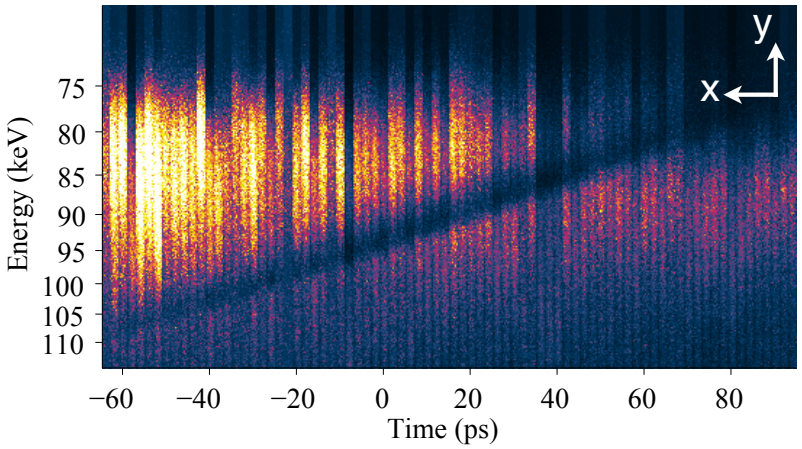

Figure 7.13 Composite image of pumped streak data. Image colorscale has been normalized to an unpumped reference for each scan.

7.3.2 Preliminary pump-probe results on gold sample

In this section, we report initial results on our attempt of a pump-probe experiment on the crystalline gold sample. The geometry of the pump-probe setup is shown in Fig. 7.14(a). The pump beam was focused using an achromatic lens ($f = 5\,\mathrm{cm}$) and delivered from the rear side of the sample. The lens was installed on a XYZ positioner, allowing adjustment of the pump beam on the sample to cover the full size of the electron probe (about 0.5 mm). In practice, the pump beam size was chosen to be greater than 2 mm irradiation over half the sample area, accounting for uncertainty in the determination of the electron probe location at the sample.

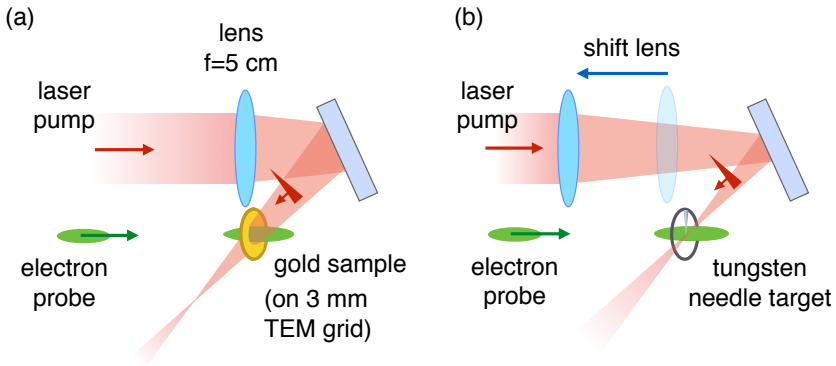

Figure 7.14 Setup for (a) pump-probe experiment on the single crystal gold sample, and (b) determination of time zero.

Laser-induced heating and melting of single crystal gold thin foil was investigated in Ref. [129] using 3.5 MeV electrons and the dynamics was found to be on the 10 ps timescale. As shown in the previous section, this should be resolvable using our setup. At present, in order to accumulate sufficient data for statistics, we need to carefully adjust the pump fluence below a threshold above which non-reversible melting process occurs, but high enough in consideration of the signal-to-noise ratio. The preliminary measurements were performed using streaking mode. An ideal streak would require the different temporal components to be spatially separated uniformly. Since the diffracted electrons emerge from the sample at different propagation angles, the fringe fields present in the magnetic spectrometer used in our previous setup could complicate the trajectories for these diffracted electrons, causing overlapping or focusing. Therefore, in our initial test, instead of using the spectrometer for streaking, we simply took advantage of the achromaticity of the solenoid to obtain a streaked diffraction spot, albeit greatly sacrificing the temporal resolution. In Fig. 7.15(a), we show a diffraction image with streaked Bragg spots. Due to an intentionally misaligned solenoid, diffraction peaks such as (220) and (240) become slightly more streaked compared to the width resulting solely from the energy spread in a well-aligned solenoid. Temporal information spanning 100 ps is imprinted on these streaks.

Data acquisition followed the same procedure in the previous section with alternating "pumped" and "unpumped" exposure every 200 ms. The delay timing was chosen such that the pump pulse arrives at the sample crossing the middle of the electron bunch. The method of determining the delay time (time zero) is illustrated in Fig. 7.14(b). The focusing lens for the pump beam was translated such that the light could be focused onto the tip of a tungsten needle at the same plane as the gold sample. A similar measurement to that of plasma probing discussed in the previous section was done, in which the deflection of electrons caused by the induced electric field of plasma formation at the tip of the needle was observed in the dispersed elec-

tron beams. This technique allows us to set the time zero properly with respect to the electron probe. After the appropriate time delay was set, the lens was shifted back without affecting timing and the needle target was replaced with the thin film sample.

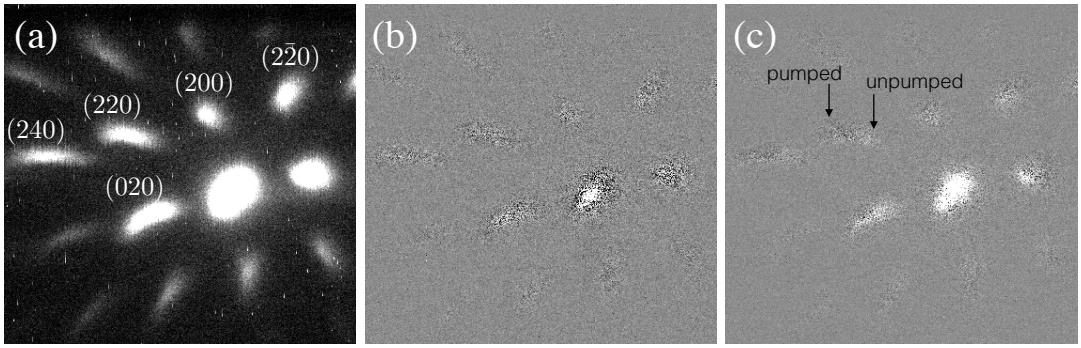

Figure 7.15 (a) Streaked electron diffraction pattern, unpumped. (b) averaged subtraction of two "unpumped" images; (c) averaged subtraction of "pumped" and "unpumped" images.

We found the sample was completely destroyed after a few hundred shots of irradiation at a fluence level of about 3 mJ/cm^2. At lower pump fluence <1 mJ/cm^2, we were not able to observe any changes above the fluctuation level. When we slighly increased the pump above 1 mJ/cm^2, we noticed a slow degrading of the diffraction efficiency over the course of data acquisition ($\sim 10^5$ laser shots). For data accumulation at a kHz, there may be an issue with heat dissipation from laser excitation, which is still not clear at this stage for our setup of the thin film sample. To separate out signals potentially resulting from structural changes on ultrafast timescales, we performed an analysis, in which every pair of subsequent two "unpumped" images are subtracted from each other and averaged using all images. This gave us a baseline for the change of diffraction patterns on a longer time scale, during which data are acquired. The result is shown in Fig. 7.15(b), taken using 15 pairs of "unpumped" images, i.e., averaging 1500 shots in total. Fig. 7.15(c) shows the usual averaged subtracted image from 30 pairs of "pumped" and "unpumped" (3000 shots). Note

that Fig. 7.15(c) has a reduced noise compared to (b) as a consequence of more images being used for averaging. The streaked Bragg peak signal appears uniform in Fig. 7.15(b), whereas in Fig. 7.15(c) a modulation can be seen. There is also a clear visible difference in the undiffracted core. The preliminary results might be evidence of a photo-induced structural change on picosecond time scales. Since the pump beam is split from the main laser beam driving electrons, it has a quite complex mode as a result of the wavefront manipulation for the electron optimization (cf. Chapter VI). This may result in an additional source of noise due to the fluctuation in the pump energy, induced by the vibration of the beam splitter pellicle membrane.Ongoing further work will concentrate on improving the signal-to-noise ratio as well as the temporal resolution.

7.4 Conclusion

The feasibility of using wakefield accelerated electrons as an ultrafast probe was investigated in this chapter. These electrons with energy range of 70-110 keV can be suitable for electron diffraction. The inherent short-bunch duration and temporal synchronization makes them a promising novel source for ultrafast electron diffraction applications. Using a solenoid magnetic lens to control the transverse beam size, first proof-of-principle experiments were performed to demonstrate sufficient transverse coherence for producing clear static diffraction patterns. A single-shot gold diffraction pattern was obtained, by virtue of improvements to the electron beam made possible by the adaptive optimization technique described in the previous chapter.

In the current arrangement, the energy spread of these electrons precludes further adaption to time-resolved diffraction due to the temporal stretching of probe electrons as they drift to the sample. Placing the sample closer to the source will help mitigate this problem, but only marginally, because of other considerations such as sample damage from the LWFA driver laser. Solutions to this problem may require either

temporally compressing the elongated electron bunches or additional energy selection and electron beam transport system to deflect electrons from the laser path.

One advantage of laser accelerated electrons may be the fact that these electrons are accelerated over a very short distance and thus preserve the strong correlation in phase-space distribution, which can be exploited later for compressing to the original duration. Streaking the electrons is another way to take advantage of this correlation. A simple magnet will spatially separate different temporal components because of the momentum-position correlation. In streaking mode, the temporal information is embedded in a single exposure without the need to change the time delay as in scanning mode. The longitudinal phase space was obtained from a time-scan measurement.

We applied this technique to study the dynamics of a non-equilibrium plasma "sample". In the current experiment configuration, the plasma target is placed at the same location we would place the solid crystalline sample, 15–20 cm from the source. 10 ps temporal resolution was demonstrated. Since unlike a solid target, there is no issue of damage for the plasma "sample", the temporal resolution can be easily further improved to sub-ps by placing the target a few mm from the source (just far enough to prevent ionization by the LWFA laser).

CHAPTER VIII

Conclusion and Outlook

This thesis describes the first comprehensive experimental campaign of laser wakefield acceleration and potential applications in an experimental regime using multi-millijoule lasers. Laser-plasma interaction experiments with relativistic intensities have many attractive applications for the production of particle and radiation beams, that would benefit from a compact, high-repetition rate source. While high-energy pulse experiments are still mostly limited to single-shot, laser systems delivering 10-mJ pulses, such as the λ^3 laser used in this work, have already been capable of operation at kHz repetition rates. A major objective of this work was to develop a wakefield electron source at kHz. Using pulse energies as low as a few millijoules for laser wakefield acceleration had never been demonstrated experimentally due to a number of challenges such as the lower achievable intensity and restrictive conditions for electron trapping.

One promising avenue is pulse compression towards the few-optical-cycle regime. Although optical pulses with durations below 10 fs for Ti:S lasers can be routinely produced, the pulse energy is typically too low to be used for laser wakefield acceleration. Increasing energy to 10 mJ or higher so far has relied on fairly intricate optical parametric amplification. In the first experiment of the thesis, we demonstrate a simple yet robust method to efficiently compress laser pulses from 36 fs to 16 fs

using ionization nonlinearities and 3D mode evolution similar to that previously observed in waveguides, but without any external guiding structures. This is a versatile mechanism that can be applied to even higher energy pulses.

Notwithstanding that the self-compressed pulse was not implemented in the electron acceleration experiments, electron beams were measured from wakefield acceleration using 8 mJ, 32 fs laser pulses. These accelerated electrons are consequence of a trapping mechanism where a spatially varying density leads to a decreasing phase velocity of plasma waves. This has been confirmed by both 2D and 3D PIC simulations. The dephasing and slow down of the plasma wave limits the energy gain of the trapped electrons to sub-relativistic energies.

Given an initial set of conditions of the driving laser, the generated plasma waves provide both the longitudinal accelerating field and the transverse electric fields, which can affect the conditions for trapping electrons, focusing of electrons, their energy spread and final beam divergence. The full three dimensional dynamic structure of the plasma waves constitutes a large parameter space. We applied an adaptive control technique using wavefront manipulation to demonstrate significant optimization of the electron acceleration with improved charge and divergence. Precise control and stability is crucial for LWFA applications and the implications of this study show that future high-repetition rate system can benefit from such techniques in laser plasma experiments.

Finally, with the optimized electron beam, we did a proof-of-principle experiment to demonstrate the feasibility of performing electron diffraction using the LWFA source. The first set of time-resolved measurements was to use the electrons to probe the evolution of plasma fields generated in optical field ionized plasmas. A temporal resolution of 10 ps was achieved by magnetic streaking of the probe, while further improvement to sub-ps resolution can be straightforwardly implemented by modifying the geometrical arrangement. Preliminary pump probe results were also obtained on

a thin solid crystalline gold sample.

The work presented in this thesis has a few important implications for future development of a high-repetition rate laser wakefield electron source and applications.

First, a significant challenge in high intensity plasma experiments is the control of shot-to-shot variation. Our experimental results obtained using the low-power laser system have shown superior stability and reproducibility compared with other laser wakefield experiments, mainly due to operation in a regime where the electron trapping and acceleration rely on a controlled injection rather than some strongly nonlinear evolution, and use of a stable flowing target. However, the fluctuations are still high compared to state-of-art conventional accelerators and photocathode based electron guns. In particular, with 10% shot-to-shot variation, it remains a challenge to achieve sufficient signal-to-noise ratio in some time-resolved electron diffraction experiments where the observed effect (e.g., a change in the Bragg amplitude) is on the same order. Therefore the sensitivity obtained using these electrons as a probe is compromised by the instability.

Second, the significant improvement in the electron beam emittance enabled by coherent manipulation of the wavefront indicates that the wakefield structure and the affect on electron seeding are very sensitive to the mode of the driving laser pulse throughout the interaction region. More insight to the underlying physical processes can be obtained through the improvement of the control technique. The concept of adaptive optimization is a robust technique that could be implemented on virtually any high-repetition rate plasma experiment for a multitude of parameters beyond the wavefront control demonstrated in this work, specifically for the temporal phase control.

Further boosting the electron energies to the MeV range will not only greatly expand their applications but also overcome existing drawbacks such as the temporal broadening associated with sub-relativistic energies. In addition to the fine-scale

control we have demonstrated, optimization of the first-order geometry of the electromagnetic energy density of the laser pulse is expected to affect the 3D wakefield response and energy gain of electrons. This has not been explored in this thesis due to the limited pulse energy and duration used – the $f/2$ focusing geometry employed in our experiments is far from generally optimal conditions for driving plasma waves over long propagation distance. The λ^3 laser system is now upgraded to deliver up to 13 mJ energy on target, which is more than 1.6 times higher than that used in this work. Changing to a larger f-number with a longer focal length will clearly be an interesting subject of future studies. We have shown that ionization nonlinearities can strongly modify the laser pulse and lead to pulse compression under appropriate conditions, this process has not yet been used for laser plasma acceleration experiments. Future work will focus on how to incorporate the pulse shaping into the acceleration experiment as a first stage and to study its effect on the performance of the electron accelerator.

Development in target design is another aspect to consider. We have shown that the trapping and acceleration can be stabilized by properly tuning the plasma profile. Both simulations and experimental evidence suggest tailoring the density profile may offer more control to improve the performance, for example, by separating electron trapping and acceleration into a two-step process. The increased complexity for gas target design may raise several engineering issues for high-repetition rate operation.

As a final remark, the work presented here demonstrating a kHz wakefield electron source and relevant applications should provide the basis for future research efforts in developing compact, high-repetition sources from laser plasma based accelerators for practical uses in a broad range of scientific and engineering fields. This is because understanding and control of the plasma wave structure and high-repetition rate studies is critical to the future success of plasma based accelerators.

APPENDICES

APPENDIX A

Atomic units

Atomics units are used in the ADK rate formula, Eq. (2.6). It is a unit system based on physical quantities associated with the ground state of hydrogen, which is convenient for atomic physics calculations. In atomic units, the following fundamental physical constants are defined to be unity, $m_e = e = \hbar = a_0 = 1$. Here m_e is the electron mass, e is elementary charge, $\hbar = h/2\pi$ is the Planck constant divided by 2π and a_0 is the Bohr radius (not to confuse with the normalized vector potential in this thesis). Table A.1 summarizes some useful physical quantities in atomic units and their values in SI units.

Physical quantity	Value in atomic units	Values in SI units
Electron mass m_e	1	9.1094×10^{-31} kg
Electron charge e	1	1.6022×10^{-19} C
Bohr radius a_0	1	5.2918×10^{-11} m
Electric constant ϵ_0	$1/4\pi$	8.8542×10^{-12} F/m
Energy	$\hbar^2/m_e a_0^2 = 1$	27.2114 eV
Angular frequency	v_0/a_0	$4.13414 \times 10^{16}\,\mathrm{s}^{-1}$
Angular momentum $\hbar$	1	$1.0546 \times 10^{-34}\,\mathrm{J \cdot s}$
Electric field strength	$e/(4\pi\epsilon_0 a_0^2) = 1$	$5.14221 \times 10^{11}\,\mathrm{V/m}$
Speed of light	137	$2.998 \times 10^{8}\,\mathrm{m/s}$

Table A.1 Atomic units

APPENDIX B

List of publications

JOURNAL ARTICLES

1. **Z.-H. He**, J. A. Nees, B. Hou, K. M. Krushelnick, and A. G. R. Thomas, "Enhancement of plasma wakefield generation and self-compression of femtosecond laser pulses by ionization gradients," Plasma Phys. Control. Fusion, **56**, 084010 (2014).

2. M. Vargas, W. Schumaker, **Z.-H. He**, Z. Zhao, K. Behm, V. Chvykov, B. Hou, K. M. Krushelnick, A. Maksimchuk, V. Yanovsky, and A. G. R. Thomas, "Improvements to laser wakefield accelerated electron beam stability, divergence, and energy spread using three-dimensional printed two-stage gas cell targets," Appl. Phys. Lett. **104**, 174103 (2014).

3. G. Sarri, W. Schumaker, A. Di Piazza, K. Poder, J. M. Cole, M. Vargas, D. Doria, S. Kushel, B. Dromey, G. Grittani, L. A. Gizzi, M. E. Dieckmann, A. Green, V. Chvykov, A. Maksimchuk, V. Yanovsky, **Z.-H. He**, B. X. Hou, J. A. Nees, S. Kar, Z. Najmudin, A. G. R. Thomas, C. H. Keitel, K. M. Krushelnick, and M. Zepf, "Laser-driven generation of collimated ultra-relativistic positron beams," Plasma Phys. Control. Fusion, **55**, 124017 (2013).

4. **Z.-H. He**, B. Hou, J. A. Nees, J. H. Easter, J. Faure, K. Krushelnick and A. G. R. Thomas, "High repetition-rate wakefield electron source generated by few-millijoule, 30 fs laser pulses on a density downramp," New J. Phys. **15**, 053016 (2013).

5. **Z.-H. He**, A. G. R. Thomas, B. Beaurepaire, J. A. Nees, B. Hou, V. Malka, K. Krushelnick, and J. Faure, "Electron diffraction using ultrafast electron bunches from a laser-wakefield accelerator at kHz repetition rate," Appl. Phys. Lett. **102**, 064104 (2013).

6. G Sarri, W Schumaker, A Di Piazza, M Vargas, B Dromey, ME Dieckmann, V Chvykov, A Maksimchuk, V Yanovsky, **ZH He**, BX Hou, JA Nees, AGR Thomas, CH Keit, M Zepf, K Krushelnick, "A table-top laser-based source of femtosecond, collimated, ultra-relativistic positron beams," Phys. Rev. Lett. **110**, 255002 (2013).

7. S. Jolly, **Z. He**, W. Schumaker, C. McGuffey, K. Krushelnick, A. G. R. Thomas, "Stereolithography based method of creating custom gas density profile targets for high intensity laser-plasma experiments," Rev. Sci. Instrum. **83**, 073503 (2012).

8. B. Hou, J. H. Easter, J. A. Nees, **Z. He**, A. G. R. Thomas, and K. Krushelnick, "Compressor optimization with compressor-based multiphoton intrapulse interference phase scan (MIIPS)," Opt. Lett. **37**, 1385-1387 (2012).

9. Bixue Hou, John A. Nees, **Zhaohan He**, George Petrov, Jack Davis, James H. Easter, Alexander G. R. Thomas, and Karl M. Krushelnick. "Laser-ion acceleration through controlled surface contamination," Phys. Plasmas **18**, 040702 (2011).

MANUSCRIPTS UNDER REVIEW

1. **Z.-H. He**, J. A. Nees, B. Hou, K. Krushelnick, and A. G. R. Thomas, "Ionization induced self-compression of tightly focused femtosecond laser pulses".

2. **Z.-H. He**, B. Hou, V. Lebailly, J. A. Nees, K. Krushelnick, A. G. R. Thomas, "Coherent Control of Plasma Dynamics".

BIBLIOGRAPHY

BIBLIOGRAPHY

[1] J. B. Hastings, F. M. Rudakov, D. H. Dowell, J. F. Schmerge, J. D. Cardoza, J. M. Castro, S. M. Gierman, H. Loos, and P. M. Weber, "Ultrafast time-resolved electron diffraction with megavolt electron beams," Appl. Phys. Lett. **89** (2006).

[2] T. Tajima and J. M. Dawson, "Laser Electron Accelerator," Phys. Rev. Lett. **43**, 267 (1979).

[3] C. Joshi, T. Tajima, J. M. Dawson, H. A. Baldis, and N. A. Ebrahim, "Forward Raman Instability and Electron Acceleration," Phys. Rev. Lett. **47**, 1285 (1981).

[4] N. E. Andreev, L. M. Gorbunov, and V. I. Kirsanov, "Self-modulation of laser pulses in plasma and laser acceleration of electrons," Plasma Physics Reports **21**, 824 (1995).

[5] K. Nakajima, D. Fisher, T. Kawakubo, H. Nakanishi, A. Ogata, Y. Kato, Y. Kitagawa, R. Kodama, K. Mima, H. Shiraga, et al., "Observation of Ultrahigh Gradient Electron Acceleration by a Self-Modulated Intense Short Laser Pulse," Phys. Rev. Lett. **74**, 4428 (1995).

[6] A. Modena, Z. Najmudin, A. Dangor, E., C. Clayton, E., K. A. Marsh, C. Joshi, V. Malka, C. Darrow, et al., "Electron acceleration from the breaking of relativistic plasma waves," Nature **377**, 606 (1995).

[7] A. Ting, C. I. Moore, K. Krushelnick, C. Manka, E. Esarey, P. Sprangle, R. Hubbard, H. R. Burris, R. Fischer, and M. Baine, "Plasma wakefield generation and electron acceleration in a self-modulated laser wakefield accelerator experiment," Phys. Plasmas **4**, 1889 (1997).

[8] S. P. D. Mangles, C. D. Murphy, Z. Najmudin, A. G. R. Thomas, J. L. Collier, A. E. Dangor, E. J. Divall, P. Foster, J. Gallacher, C. J. Hooker, et al., "Monoenergetic beams of relativistic electrons from intense laser-plasma interactions.," Nature **431**, 535 (2004).

[9] C. Geddes, C. S. Toth, J. van Tilborg, E. Esarey, C. B. Schroeder, D. Bruhwiler, C. Nieter, J. Cary, and W. P. Leemans, "High-quality electron beams from a laser wakefield accelerator using plasma-channel guiding," Nature **431**, 538 (2004).

[10] C. Rechatin, J. Faure, A. Ben-Ismail, J. Lim, R. Fitour, A. Specka, H. Videau, A. Tafzi, F. Burgy, and V. Malka, "Controlling the Phase-Space Volume of Injected Electrons in a Laser-Plasma Accelerator," Phys. Rev. Lett. **102**, 164801 (2009).

[11] E. Brunetti, R. P. Shanks, G. G. Manahan, M. R. Islam, B. Ersfeld, M. P. Anania, S. Cipiccia, R. C. Issac, G. Raj, G. Vieux, et al., "Low Emittance, High Brilliance Relativistic Electron Beams from a Laser-Plasma Accelerator," Phys. Rev. Lett. **105**, 215007 (2010).

[12] W. Leemans, B. Nagler, A. Gonsalves, C. Toth, K. Nakamura, C. Geddes, E. Esarey, C. Schroeder, and S. Hooker, "GeV electron beams from a centimetre-scale accelerator," Nat. Phys. **2**, 696 (2006).

[13] S. Kneip, S. R. Nagel, S. F. Martins, S. P. D. Mangles, C. Bellei, O. Chekhlov, R. J. Clarke, N. Delerue, E. J. Divall, G. Doucas, et al., "Near-GeV Acceleration of Electrons by a Nonlinear Plasma Wave Driven by a Self-Guided Laser Pulse," Phys. Rev. Lett. **103**, 035002 (2009).

[14] D. H. Froula, C. E. Clayton, T. Döppner, K. A. Marsh, C. P. J. Barty, L. Divol, R. A. Fonseca, S. H. Glenzer, C. Joshi, W. Lu, et al., "Measurements of the Critical Power for Self-Injection of Electrons in a Laser Wakefield Accelerator," Phys. Rev. Lett. **103**, 215006 (2009).

[15] X. Wang, R. Zgadzaj, N. Fazel, Z. Li, S. Yi, X. Zhang, W. Henderson, Y.-Y. Chang, R. Korzekwa, H.-E. Tsai, et al., "Quasi-monoenergetic laser-plasma acceleration of electrons to 2 gev," Nature communications **4** (2013).

[16] A. Pukhov and J. Meyer-ter Vehn, "Laser wake field acceleration: the highly non-linear broken-wave regime," Appl. Phys. B **74**, 355 (2002).

[17] K. Schmid, L. Veisz, F. Tavella, S. Benavides, R. Tautz, D. Herrmann, A. Buck, B. Hidding, A. Marcinkevicius, U. Schramm, et al., "Few-Cycle Laser-Driven Electron Acceleration," Phys. Rev. Lett. **102**, 124801 (2009).

[18] S. Gordienko and A. Pukhov, "Scalings for ultrarelativistic laser plasmas and quasimonoenergetic electrons," Phys. Plasmas **12**, (2005).

[19] W. Lu, M. Tzoufras, C. Joshi, F. S. Tsung, W. B. Mori, J. Vieira, R. A. Fonseca, and L. O. Silva, "Generating multi-GeV electron bunches using single stage laser wakefield acceleration in a 3D nonlinear regime," Phys. Rev. ST Accel. Beams **10**, 061301 (2007).

[20] B. Beaurepaire, A. Lifschitz, and J. Faure, "Electron acceleration in sub-relativistic wakefields driven by few-cycle laser pulses," New J. Phys. **16**, 023023 (2014).

[21] D. Strickland and G. Mourou, "Compression of amplified chirped optical pulses," Optics Communications **55**, 447 (1985).

[22] P. Gibbon, *Short pulse laser interactions with matter* (Imperial College Press, 2005).

[23] V. Yanovsky, V. Chvykov, G. Kalinchenko, P. Rousseau, T. Planchon, T. Matsuoka, A. Maksimchuk, J. Nees, G. Cheriaux, G. Mourou, et al., "Ultra-high intensity- 300-TW laser at 0.1 Hz repetition rate," Opt. Express **16**, 2109 (2008).

[24] KMLabs, URL `http://www.kmlabs.com`.

[25] I. Ross, P. Matousek, M. Towrie, A. Langley, and J. Collier, "The prospects for ultrashort pulse duration and ultrahigh intensity using optical parametric chirped pulse amplifiers," Optics Communications **144**, 125 (1997).

[26] A. Dubietis, R. Butkus, and A. P. Piskarskas, "Trends in chirped pulse optical parametric amplification," Selected Topics in Quantum Electronics, IEEE Journal of **12**, 163 (2006).

[27] R. M. G. M. Trines, F. Fiuza, R. Bingham, R. A. Fonseca, L. O. Silva, R. A. Cairns, and P. A. Norreys, "Simulations of efficient Raman amplification into the multipetawatt regime," Nat. Phys. **7**, 87 (2011).

[28] R. M. G. M. Trines, F. Fiúza, R. Bingham, R. A. Fonseca, L. O. Silva, R. A. Cairns, and P. A. Norreys, "Production of Picosecond, Kilojoule, and Petawatt Laser Pulses via Raman Amplification of Nanosecond Pulses," Phys. Rev. Lett. **107**, 105002 (2011).

[29] A. Galvanauskas, "Mode-scalable fiber-based chirped pulse amplification systems," Selected Topics in Quantum Electronics, IEEE Journal of **7**, 504 (2001).

[30] A. Galvanauskas, "High Power Fiber Lasers," Opt. Photon. News **15**, 42 (2004).

[31] D. J. Richardson, J. Nilsson, and W. A. Clarkson, "High power fiber lasers: current status and future perspectives.," J. Opt. Soc. Am. B **27**, B63 (2010).

[32] G. Mourou, B. Brocklesby, T. Tajima, and J. Limpert, "The future is fibre accelerators," Nat. Photonics **7**, 258 (2013).

[33] G. Mourou, N. Fisch, V. Malkin, Z. Toroker, E. Khazanov, A. Sergeev, T. Tajima, and B. L. Garrec, "Exawatt-Zettawatt pulse generation and applications," Optics Communications **285**, 720 (2012).

[34] A. Einstein, "Über einen die erzeugung und verwandlung des lichtes betreffenden heuristischen gesichtspunkt," Annalen der Physik **322**, 132 (1905).

[35] M. Göppert-Mayer, "Über elementarakte mit zwei quantensprüngen," Annalen der Physik **401**, 273 (1931).

[36] L. Keldysh, "Ionization in the field of a strong electromagnetic wave," Sov. Phys. JETP **20**, 1307 (1965).

[37] M. V. Ammosov, N. B. Delone, and V. P. Krainov, "Tunnel ionization of complex atoms and of atomic ions in an alternating electromagnetic field," Sov. Phys. JETP **64**, 1191 (1986).

[38] M. V. Ammosov, P. A. Golovinsky, I. Y. Kiyan, V. P. Krainov, and V. M. Ristic, "Tunneling ionization of atoms and atomic ions in an intense laser field with a nonhomogeneous space–time distribution," J. Opt. Soc. Am. B **9**, 1225 (1992).

[39] N. B. Delone and V. P. Krainov, "Tunneling and barrier-suppression ionization of atoms and ions in a laser radiation field," Physics-Uspekhi **41**, 469 (1998).

[40] S. Augst, D. D. Meyerhofer, D. Strickland, and S. L. Chint, "Laser ionization of noble gases by Coulomb-barrier suppression," J. Opt. Soc. Am. B **8**, 858 (1991).

[41] E. Esarey, C. B. Schroeder, and W. P. Leemans, "Physics of laser-driven plasma-based electron accelerators," Rev. Mod. Phys. **81**, 1229 (2009).

[42] B. Quesnel and P. Mora, "Theory and simulation of the interaction of ultraintense laser pulses with electrons in vacuum," Phys. Rev. E **58**, 3719 (1998).

[43] A. I. Akhiezer and R. V. Polovin, "Theory of wave motion in an electron plasma," Sov. Phys. JETP **3** (1956).

[44] G.-Z. Sun, E. Ott, Y. C. Lee, and P. Guzdar, "Self-focusing of short intense pulses in plasmas," Phys. Fluids **30**, 526 (1987).

[45] Z. M. Sheng and J. Meyer-ter Vehn, "Relativistic wave breaking in warm plasmas," Phys. Plasmas **4**, 493 (1997).

[46] S. V. Bulanov, F. Pegoraro, A. M. Pukhov, and A. S. Sakharov, "Transverse-wake wave breaking," Phys. Rev. Lett. **78**, 4205 (1997).

[47] E. Esarey and M. Pilloff, "Trapping and acceleration in nonlinear plasma waves," Phys. Plasmas **2**, 1432 (1995).

[48] W. B. Mori, "The physics of the nonlinear optics of plasmas at relativistic intensities for short-pulse lasers," Quantum Electronics, IEEE Journal of **33**, 1942 (1997).

[49] A. B. Borisov, A. V. Borovskiy, O. B. Shiryaev, V. V. Korobkin, A. M. Prokhorov, J. C. Solem, T. S. Luk, K. Boyer, and C. K. Rhodes, "Relativistic and charge-displacement self-channeling of intense ultrashort laser pulses in plasmas," Phys. Rev. A **45**, 5830 (1992).

[50] B. Hafizi, A. Ting, P. Sprangle, and R. F. Hubbard, "Relativistic focusing and ponderomotive channeling of intense laser beams," Phys. Rev. E **62**, 4120 (2000).

[51] E. Esarey, P. Sprangle, J. Krall, and A. Ting, "Overview of plasma-based accelerator concepts," IEEE Trans. Plasma Sci. **24**, 252 (1996).

[52] S. Rae, "Ionization-induced defocusing of intense laser pulses in high-pressure gases," Optics Communications **97**, 25 (1993), ISSN 0030-4018.

[53] S. Rae, "Spectral blueshifting and spatial defocusing of intense laser pulses in dense gases," Optics Communications **104**, 330 (1994).

[54] W. M. Wood, C. W. Siders, and M. C. Downer, "Measurement of femtosecond ionization dynamics of atmospheric density gases by spectral blueshifting," Phys. Rev. Lett. **67**, 3523 (1991).

[55] E. Esarey, A. Ting, and P. Sprangle, "Frequency shifts induced in laser pulses by plasma waves," Phys. Rev. A **42**, 3526 (1990).

[56] A. V. Kim, S. F. Lirin, A. M. Sergeev, E. V. Vanin, and L. Stenflo, "Compression and frequency up-conversion of an ultrashort ionizing pulse in a plasma," Phys. Rev. A **42**, 2493 (1990).

[57] S. C. Wilks, J. M. Dawson, W. B. Mori, T. Katsouleas, and M. E. Jones, "Photon accelerator," Phys. Rev. Lett. **62**, 2600 (1989).

[58] C. D. Murphy, R. Trines, J. Vieira, A. J. W. Reitsma, R. Bingham, J. L. Collier, E. J. Divall, P. S. Foster, C. J. Hooker, A. J. Langley, et al., "Evidence of photon acceleration by laser wake fields," Phys. Plasmas **13**, 033108 (2006).

[59] L.-M. Peng, M. Whelan, and S. Dudarev, *High-Energy Electron Diffraction and Microscopy* (Oxford Univ. Press, 2011).

[60] S. Semushin and V. Malka, "High density gas jet nozzle design for laser target production," Rev. Sci. Instrum. **72**, 2961 (2001).

[61] M. Takeda, H. Ina, and S. Kobayashi, "Fourier-transform method of fringe-pattern analysis for computer-based topography and interferometry," J. Opt. Soc. Am. **72**, 156 (1982).

[62] P. Tomassini and A. Giulietti, "A generalization of Abel inversion to non-axisymmetric density distribution," Optics Communications **199**, 143 (2001).

[63] M. Hipp, J. Woisetschläger, P. Reiterer, and T. Neger, "Digital evaluation of interferograms," Measurement **36**, 53 (2004).

[64] R. Trebino, K. W. DeLong, D. N. Fittinghoff, J. N. Sweetser, M. A. Krumbugel, B. A. Richman, and D. J. Kane, "Measuring ultrashort laser pulses in the time-frequency domain using frequency-resolved optical gating," Rev. Sci. Instrum. **68**, 3277 (1997).

[65] R. D. T. F. Kawrakow I, Mainegra-Hing E and W. B, "The EGSnrc code system: Monte Carlo simulation of electron and photon transport," NRCC Report PIRS-701, National Research Council of Canada, Ottawa, Canada (2010).

[66] K. A. Tanaka, T. Yabuuchi, T. Sato, R. Kodama, Y. Kitagawa, T. Takahashi, T. Ikeda, Y. Honda, and S. Okuda, "Calibration of imaging plate for high energy electron spectrometer," Rev. Sci. Instrum. **76**, 013507 (2005).

[67] Y. Glinec, J. Faure, A. Guemnie-Tafo, V. Malka, H. Monard, J. P. Larbre, V. De Waele, J. L. Marignier, and M. Mostafavi, "Absolute calibration for a broad range single shot electron spectrometer," Rev. Sci. Instrum. **77** (2006).

[68] COMSOL, Inc., URL `http://www.comsol.com`.

[69] A. G. Mordovanakis, J. Easter, N. Naumova, K. Popov, P.-E. Masson-Laborde, B. Hou, I. Sokolov, G. Mourou, I. V. Glazyrin, W. Rozmus, et al., "Quasimonoenergetic Electron Beams with Relativistic Energies and Ultrashort Duration from Laser-Solid Interactions at 0.5 kHz," Phys. Rev. Lett. **103**, 235001 (2009).

[70] J. M. Dawson, "Particle simulation of plasmas," Rev. Mod. Phys. **55**, 403 (1983).

[71] R. Fonseca, L. Silva, F. Tsung, V. Decyk, W. Lu, C. Ren, W. Mori, S. Deng, S. Lee, T. Katsouleas, et al., in *Computational Science – ICCS 2002*, edited by P. Sloot, A. Hoekstra, C. Tan, and J. Dongarra (Springer Berlin Heidelberg, 2002), vol. 2331 of *Lecture Notes in Computer Science*, pp. 342–351.

[72] F. Krausz and M. Ivanov, "Attosecond physics," Rev. Mod. Phys. **81**, 163 (2009).

[73] A. Couairon and A. Mysyrowicz, "Femtosecond filamentation in transparent media," Physics Reports **441**, 47 (2007).

[74] M. Nisoli, S. D. Silvestri, O. Svelto, R. Szipöcs, K. Ferencz, C. Spielmann, S. Sartania, and F. Krausz, "Compression of high-energy laser pulses below 5 fs," Opt. Lett. **22**, 522 (1997).

[75] V. Chvykov, C. Radier, G. Cheriaux, G. Kalinchenko, V. Yanovsky, and G. Mourou, in *Lasers and Electro-Optics (CLEO) and Quantum Electronics and Laser Science Conference (QELS), 2010 Conference on, San Jose, CA,* (2010), pp. 1–2.

[76] F. S. Tsung, C. Ren, L. O. Silva, W. B. Mori, and T. Katsouleas, "Generation of ultra-intense single-cycle laser pulses by using photon deceleration," Proc. Natl. Acad. Sci. U.S.A. **99**, 29 (2002).

[77] C. Ren, B. J. Duda, R. G. Hemker, W. B. Mori, T. Katsouleas, T. M. Antonsen, and P. Mora, "Compressing and focusing a short laser pulse by a thin plasma lens," Phys. Rev. E **63**, 026411 (2001).

[78] O. Shorokhov, A. Pukhov, and I. Kostyukov, "Self-Compression of Laser Pulses in Plasma," Phys. Rev. Lett. **91**, 265002 (2003).

[79] D. F. Gordon, B. Hafizi, R. F. Hubbard, J. R. Peñano, P. Sprangle, and A. Ting, "Asymmetric Self-Phase Modulation and Compression of Short Laser Pulses in Plasma Channels," Phys. Rev. Lett. **90**, 215001 (2003).

[80] J. Faure, Y. Glinec, J. J. Santos, F. Ewald, J.-P. Rousseau, S. Kiselev, A. Pukhov, T. Hosokai, and V. Malka, "Observation of Laser-Pulse Shortening in Nonlinear Plasma Waves," Phys. Rev. Lett. **95**, 205003 (2005).

[81] J. Schreiber, C. Bellei, S. P. D. Mangles, C. Kamperidis, S. Kneip, S. R. Nagel, C. A. J. Palmer, P. P. Rajeev, M. J. V. Streeter, and Z. Najmudin, "Complete Temporal Characterization of Asymmetric Pulse Compression in a Laser Wakefield," Phys. Rev. Lett. **105**, 235003 (2010).

[82] A. A. Balakin, A. G. Litvak, V. A. Mironov, and S. A. Skobelev, "Self-compression of relativistically strong femtosecond laser pulses during the excitation of a plasma wake wave," EPL (Europhysics Letters) **100**, 34002 (2012).

[83] A. Pipahl, E. A. Anashkina, M. Toncian, T. Toncian, S. A. Skobelev, A. V. Bashinov, A. A. Gonoskov, O. Willi, and A. V. Kim, "High-intensity few-cycle laser-pulse generation by the plasma-wakefield self-compression effect," Phys. Rev. E **87**, 033104 (2013).

[84] C. F. Dutin, A. Dubrouil, S. Petit, E. Mével, E. Constant, and D. Descamps, "Post-compression of high-energy femtosecond pulses using gas ionization," Opt. Lett. **35**, 253 (2010).

[85] T. Auguste, O. Gobert, C. F. Dutin, A. Dubrouil, E. Mével, S. Petit, E. Constant, and D. Descamps, "Application of optical-field-ionization-induced spectral broadening in helium gas to the postcompression of high-energy femtosecond laser pulses," J. Opt. Soc. Am. B **29**, 1277 (2012).

[86] S. A. Skobelev, A. V. Kim, and O. Willi, "Generation of High-Energy Few-Cycle Laser Pulses by Using the Ionization-Induced Self-Compression Effect," Phys. Rev. Lett. **108**, 123904 (2012).

[87] O. Hort, A. Dubrouil, C. Fourcade-Dutin, S. Petit, E. Mével, D. Descamps, and E. Constant, "Terawatt Post compression of high energy fs pulses using ionization: A way to overcome the conventional limitation in energy of few optical cycle pulses," EPJ Web of Conferences **41**, 10021 (2013).

[88] R. Szipöcs, C. Spielmann, F. Krausz, and K. Ferencz, "Chirped multilayer coatings for broadband dispersion control in femtosecond lasers," Opt. Lett. **19**, 201 (1994).

[89] N. L. Wagner, E. A. Gibson, T. Popmintchev, I. P. Christov, M. M. Murnane, and H. C. Kapteyn, "Self-Compression of Ultrashort Pulses through Ionization-Induced Spatiotemporal Reshaping," Phys. Rev. Lett. **93**, 173902 (2004).

[90] J. K. Wahlstrand, Y.-H. Cheng, and H. M. Milchberg, "High Field Optical Nonlinearity and the Kramers-Kronig Relations," Phys. Rev. Lett. **109**, 113904 (2012).

[91] A. Sergeev, E. Vanin, L. Stenflo, D. Anderson, M. Lisak, and M. L. Quiroga-Teixeiro, "Nonlinear shaping of a two-dimensional ultrashort ionizing pulse," Phys. Rev. A **46**, 7830 (1992).

[92] P. Chessa, E. De Wispelaere, F. Dorchies, V. Malka, J. R. Marquès, G. Hamoniaux, P. Mora, and F. Amiranoff, "Temporal and Angular Resolution of the Ionization-Induced Refraction of a Short Laser Pulse in Helium Gas," Phys. Rev. Lett. **82**, 552 (1999).

[93] A. G. R. Thomas, Z. Najmudin, S. P. D. Mangles, C. D. Murphy, A. E. Dangor, C. Kamperidis, K. L. Lancaster, W. B. Mori, P. A. Norreys, W. Rozmus, et al., "Effect of Laser-Focusing Conditions on Propagation and Monoenergetic Electron Production in Laser-Wakefield Accelerators," Phys. Rev. Lett. **98**, 095004 (2007).

[94] S. Bulanov, N. Naumova, F. Pegoraro, and J. Sakai, "Particle injection into the wave acceleration phase due to nonlinear wake wave breaking," Phys. Rev. E **58**, R5257 (1998).

[95] C. G. R. Geddes, K. Nakamura, G. R. Plateau, C. Toth, E. Cormier-Michel, E. Esarey, C. B. Schroeder, J. R. Cary, and W. P. Leemans, "Plasma-Density-Gradient Injection of Low Absolute-Momentum-Spread Electron Bunches," Phys. Rev. Lett. **100**, 215004 (2008).

[96] J. Faure, C. Rechatin, O. Lundh, L. Ammoura, and V. Malka, "Injection and acceleration of quasimonoenergetic relativistic electron beams using density gradients at the edges of a plasma channel," Phys. Plasmas **17** (2010).

[97] K. Schmid, A. Buck, C. M. S. Sears, J. M. Mikhailova, R. Tautz, D. Herrmann, M. Geissler, F. Krausz, and L. Veisz, "Density-transition based electron injector for laser driven wakefield accelerators," Phys. Rev. ST Accel. Beams **13**, 091301 (2010).

[98] G. B. Whitham, *Linear and Nonlinear Waves* (Wiley, New York, 1974).

[99] A. V. Brantov, T. Z. Esirkepov, M. Kando, H. Kotaki, V. Y. Bychenkov, and S. V. Bulanov, "Controlled electron injection into the wake wave using plasma density inhomogeneity," Phys. Plasmas **15**, 073111 (2008).

[100] J. M. Dawson, "Nonlinear Electron Oscillations in a Cold Plasma," Phys. Rev. **113**, 383 (1959).

[101] T. Katsouleas and W. B. Mori, "Wave-Breaking Amplitude of Relativistic Oscillations in a Thermal Plasma," Phys. Rev. Lett. **61**, 90 (1988).

[102] S. B. van der Geer, M. J. de Loos, T. van Oudheusden, W. P. E. M. op 't Root, M. J. van der Wiel, and O. J. Luiten, "Longitudinal phase-space manipulation of ellipsoidal electron bunches in realistic fields," Phys. Rev. ST Accel. Beams **9**, 044203 (2006).

[103] P. Kung, H.-C. Lihn, H. Wiedemann, and D. Bocek, "Generation and Measurement of 50-fs (rms) Electron Pulses," Phys. Rev. Lett. **73**, 967 (1994).

[104] R. M. G. M. Trines, R. Bingham, Z. Najmudin, S. Mangles, L. O. Silva, R. Fonseca, and P. A. Norreys, "Electron trapping and acceleration on a downward density ramp: a two-stage approach," New J. Phys. **12**, 045027 (2010).

[105] J. M. Beckers, "Adaptive optics for astronomy - Principles, performance, and applications.," Annual Review of Astronomy and Astrophysics **31**, 13 (1993).

[106] M. J. Booth, "Adaptive optics in microscopy," Philosophical Transactions of the Royal Society A: Mathematical, Physical and Engineering Sciences **365**, 2829 (2007).

[107] J. Liang, D. R. Williams, and D. T. Miller, "Supernormal vision and high-resolution retinal imaging through adaptive optics," J. Opt. Soc. Am. A **14**, 2884 (1997).

[108] S. Campbell, S. M. F. Triphan, R. El-Agmy, A. H. Greenaway, and D. T. Reid, "Direct optimization of femtosecond laser ablation using adaptive wavefront shaping," Journal of Optics A: Pure and Applied Optics **9**, 1100 (2007).

[109] S.-W. Bahk, P. Rousseau, T. A. Planchon, V. Chvykov, G. Kalintchenko, A. Maksimchuk, G. A. Mourou, and V. Yanovsky, "Generation and characterization of the highest laser intensities (10^{22} W/cm^2)," Opt. Lett. **29**, 2837 (2004).

[110] O. Albert, H. Wang, D. Liu, Z. Chang, and G. Mourou, "Generation of relativistic intensity pulses at a kilohertz repetition rate," Opt. Lett. **25**, 1125 (2000).

[111] T. A. Planchon, W. Amir, J. J. Field, C. G. Durfee, J. A. Squier, P. Rousseau, O. Albert, and G. Mourou, "Adaptive correction of a tightly focused, high-intensity laser beam by use of a third-harmonic signal generated at an interface," Opt. Lett. **31**, 2214 (2006).

[112] D. S. Bethune, "Optical second-harmonic generation in atomic vapors with focused beams," Phys. Rev. A **23**, 3139 (1981).

[113] M. Beresna, P. G. Kazansky, Y. Svirko, M. Barkauskas, and R. Danielius, "High average power second harmonic generation in air," Appl. Phys. Lett. **95** (2009).

[114] R. Bartels, S. Backus, E. Zeek, L. Misoguti, G. Vdovin, I. P. Christov, M. M. Murnane, and H. C. Kapteyn, "Shaped-pulse optimization of coherent emission of high-harmonic soft X-rays," Nature **406**, 164 (2000).

[115] D. Yoshitomi, J. Nees, N. Miyamoto, T. Sekikawa, T. Kanai, G. Mourou, and S. Watanabe, "Phase-matched enhancements of high-harmonic soft X-rays by adaptive wave-front control with a genetic algorithm," Appl. Phys. B **78**, 275 (2004).

[116] E. Cormier-Michel, E. Esarey, C. G. R. Geddes, C. B. Schroeder, K. Paul, P. J. Mullowney, J. R. Cary, and W. P. Leemans, "Control of focusing fields in laser-plasma accelerators using higher-order modes," Phys. Rev. ST Accel. Beams **14**, 031303 (2011).

[117] A. H. Zewail and J. M. Thomas, *4D Electron Microscopy: Imaging in Space and Time* (Imperial College Press, London, 2010).

[118] G. Sciaini and R. J. D. Miller, "Femtosecond electron diffraction: heralding the era of atomically resolved dynamics," Reports on Progress in Physics **74**, 096101 (2011).

[119] B. J. Siwick, J. R. Dwyer, R. E. Jordan, and R. J. D. Miller, "An Atomic-Level View of Melting Using Femtosecond Electron Diffraction," Science **302**, 1382 (2003).

[120] G. Sciaini, M. Harb, S. G. Kruglik, T. Payer, C. T. Hebeisen, F.-J. Meyer zu Heringdorf, M. Yamaguchi, M. Horn-von Hoegen, R. Ernstorfer, and R. J. D. Miller, "Electronic acceleration of atomic motions and disordering in bismuth," Nature **458**, 56 (2009).

[121] P. Baum, D.-S. Yang, and A. H. Zewail, "4D Visualization of Transitional Structures in Phase Transformations by Electron Diffraction," Science **318**, 788 (2007).

[122] M. Eichberger, H. Schafer, M. Krumova, M. Beyer, J. Demsar, H. Berger, G. Moriena, G. Sciaini, and R. J. D. Miller, "Snapshots of cooperative atomic motions in the optical suppression of charge density waves," Nature **468**, 799 (2010).

[123] T. van Oudheusden, E. F. de Jong, S. B. van der Geer, W. P. E. M. O. Äôt Root, O. J. Luiten, and B. J. Siwick, "Electron source concept for single-shot sub-100 fs electron diffraction in the 100 keV range," J. Appl. Phys. **102** (2007).

[124] T. van Oudheusden, P. L. E. M. Pasmans, S. B. van der Geer, M. J. de Loos, M. J. van der Wiel, and O. J. Luiten, "Compression of Subrelativistic Space-Charge-Dominated Electron Bunches for Single-Shot Femtosecond Electron Diffraction," Phys. Rev. Lett. **105**, 264801 (2010).

[125] P. Musumeci, J. T. Moody, C. M. Scoby, M. S. Gutierrez, H. A. Bender, and N. S. Wilcox, "High quality single shot diffraction patterns using ultrashort megaelectron volt electron beams from a radio frequency photoinjector," Rev. Sci. Instrum. **81** (2010).

[126] R. Li, W. Huang, Y. Du, L. Yan, Q. Du, J. Shi, J. Hua, H. Chen, T. Du, H. Xu, et al., "Note: Single-shot continuously time-resolved MeV ultrafast electron diffraction," Rev. Sci. Instrum. **81** (2010).

[127] Y. Murooka, N. Naruse, S. Sakakihara, M. Ishimaru, J. Yang, and K. Tanimura, "Transmission-electron diffraction by MeV electron pulses," Appl. Phys. Lett. **98**, (2011).

[128] J.-H. Han, "Production of a sub-10 fs electron beam with 10^7 electrons," Phys. Rev. ST Accel. Beams **14**, 050101 (2011).

[129] P. Musumeci, J. T. Moody, C. M. Scoby, M. S. Gutierrez, and M. Westfall, "Laser-induced melting of a single crystal gold sample by time-resolved ultrafast relativistic electron diffraction," Appl. Phys. Lett. **97**, (2010).

[130] P. Baum, "On the physics of ultrashort single-electron pulses for time-resolved microscopy and diffraction," Chemical Physics **423**, 55 (2013), ISSN 0301-0104.

[131] P. Baum, "Towards ultimate temporal and spatial resolutions with ultrafast single-electron diffraction," Journal of Physics B: Atomic, Molecular and Optical Physics **47**, 124005 (2014).

[132] J. Faure, C. Rechatin, A. Norlin, A. Lifschitz, Y. Glinec, and V. Malka, "Controlled injection and acceleration of electrons in plasma wakefields by colliding laser pulses," Nature **444**, 737 (2006).

[133] S. Tokita, S. Inoue, S. Masuno, M. Hashida, and S. Sakabe, "Single-shot ultrafast electron diffraction with a laser-accelerated sub-MeV electron pulse," Appl. Phys. Lett. **95**, 111911 (2009).

[134] S. Tokita, M. Hashida, S. Inoue, T. Nishoji, K. Otani, and S. Sakabe, "Single-Shot Femtosecond Electron Diffraction with Laser-Accelerated Electrons: Experimental Demonstration of Electron Pulse Compression," Phys. Rev. Lett. **105**, 215004 (2010).

[135] O. Lundh, J. Lim, C. Rechatin, L. Ammoura, A. Ben-Ismail, X. Davoine, G. Gallot, J.-P. Goddet, E. Lefebvre, V. Malka, et al., "Few femtosecond, few kiloampere electron bunch produced by a laser-plasma accelerator," Nat. Phys. **7**, 219 (2011).

[136] C. Weninger and P. Baum, "Temporal distortions in magnetic lenses," Ultramicroscopy **113**, 145 (2012), ISSN 0304-3991.

[137] D. Kreier, D. Sabonis, and P. Baum, "Alignment of magnetic solenoid lenses for minimizing temporal distortions," Journal of Optics **16**, 075201 (2014).

[138] M. Reiser, *Theory and Design of Charged Partcile Beams* (Wiley-VCH Verlag GmbH, Weinheim, Germany, 2008).

[139] E. Fill, S. Trushin, R. Bruch, and R. Tommasini, "Diffraction of laser-plasma-generated electron pulses," Appl. Phys. B **81**, 155 (2005).

[140] Pulsar Physics, URL `http://www.pulsar.nl/gpt/`.

[141] M. Vargas, W. Schumaker, Z.-H. He, Z. Zhao, K. Behm, V. Chvykov, B. Hou, K. Krushelnick, A. Maksimchuk, V. Yanovsky, et al., "Improvements to laser wakefield accelerated electron beam stability, divergence, and energy spread using three-dimensional printed two-stage gas cell targets," Appl. Phys. Lett. **104**, 174103 (2014).

[142] P. B. Corkum, N. H. Burnett, and F. Brunel, "Above-threshold ionization in the long-wavelength limit," Phys. Rev. Lett. **62**, 1259 (1989).

[143] P. B. Lerner and J. S. Cohen, "Formation of hot electrons in noble gases by intense-field ionization: A quasistatic tunneling, independent-electron model," Phys. Rev. A **51**, 1464 (1995).

[144] T. Ditmire, E. T. Gumbrell, R. A. Smith, L. Mountford, and M. H. R. Hutchinson, "Supersonic ionization wave driven by radiation transport in a short-pulse laser-produced plasma," Phys. Rev. Lett. **77**, 498 (1996).

[145] R. Kingham and A. Bell, "An implicit Vlasov–Fokker–Planck code to model non-local electron transport in 2-D with magnetic fields," J. Comput. Phys. **194**, 1 (2004).

[146] A. Thomas, M. Tzoufras, A. Robinson, R. Kingham, C. Ridgers, M. Sherlock, and A. Bell, "A review of Vlasov–Fokker–Planck numerical modeling of inertial confinement fusion plasma," J. Comput. Phys. **231**, 1051 (2012).